The impact and response of mini-haloes and the interhalo medium on cosmic reionization

Tsang Keung Chan [1,2,3]★ Alejandro Benítez-Llambay [3,4] Tom Theuns [3] Carlos Frenk [3] and Richard Bower [3]

[1]*Department of Physics, The Chinese University of Hong Kong, Shatin, Hong Kong, China*
[2]*Department of Astronomy and Astrophysics, the University of Chicago, Chicago, IL60637, USA*
[3]*Department of Physics, Institute for Computational Cosmology, Durham University, South Road, Durham DH1 3LE, UK*
[4]*Dipartimento di Fisica G. Occhialini, Università degli Studi di Milano Bicocca, Piazza della Scienza, 3 I-20126 Milano MI, Italy*

ABSTRACT

An ionization front (I-front) that propagates through an inhomogeneous medium is slowed down by self-shielding and recombinations. We perform cosmological radiation hydrodynamics simulations of the I-front propagation during the epoch of cosmic reionization. The simulations resolve gas in mini-haloes (halo mass $10^4 \lesssim M_h[\mathrm{M}_\odot] \lesssim 10^8$) that could dominate recombinations, in a computational volume that is large enough to sample the abundance of such haloes. The numerical resolution is sufficient (gas-particle mass $\sim 20\,\mathrm{M}_\odot$ and spatial resolution <0.1 ckpc) to allow accurate modelling of the hydrodynamic response of gas to photoheating. We quantify the photoevaporation time of mini-haloes as a function of M_h and its dependence on the photoionization rate, Γ_{-12}, and the redshift of reionization, z_i. The recombination rate can be enhanced over that of a uniform medium by a factor $\sim 10{-}20$ early on. The peak value increases with Γ_{-12} and decreases with z_i, due to the enhanced contribution from mini-haloes. The clumping factor, c_r, decreases to a factor of a few at ~ 100 Myr after the passage of the I-front when the mini-haloes have been photoevaporated; this asymptotic value depends only weakly on Γ_{-12}. Recombinations increase the required number of photons per baryon to reionize the Universe by 20 per cent–100 per cent, with the higher value occurring when Γ_{-12} is high and z_i is low. We complement the numerical simulations with simple analytical models for the evaporation rate and the inverse Strömgren layer. The study also demonstrates the proficiency and potential of SPH-M1RT to address astrophysical problems in high-resolution cosmological simulations.

Key words: radiative transfer – intergalactic medium – dark ages, reionization, first stars – large-scale structure of Universe – cosmology: theory.

1 INTRODUCTION

The epoch of reionization (EOR) refers to the time during which luminous sources (e.g. hot stars) transformed the interhalo medium (hereafter IHM),[1] from mostly neutral to mostly ionized (see reviews by e.g. Loeb & Barkana 2001; Madau 2017 or Wise 2019). Following cosmic recombination at redshift $z \sim 1100$, the Universe remained neutral up to redshifts $z \sim 15{-}30$ when the first stars formed and emitted ionizing photons (Tegmark et al. 1997; Abel, Bryan & Norman 2002; Bromm, Coppi & Larson 2002). These stars and the first galaxies ionized their immediate surroundings. With more and brighter galaxies forming, cumulatively more than one ionizing photon per hydrogen was emitted, causing these cosmological H II regions (Shapiro & Giroux 1987) to percolate (Gnedin 2000a;

Barkana & Loeb 2004; Furlanetto, Zaldarriaga & Hernquist 2004; Iliev et al. 2006a), signalling the end of the EOR. After reionization, the ionizing photons emitted by galaxies and quasars keep the IHM highly ionized, with ionizations approximately balanced by recombinations in higher density regions (Bolton & Haehnelt 2007; Haardt & Madau 2012).

Observations of the polarization of the cosmic microwave background (CMB) due to Thomson scattering place the mid-point of the EOR (where about half the IHM is highly ionized) at around $z \sim 8$ (Planck Collaboration VI 2020). This is consistent with the evolution of the fraction of galaxies that are detected in Lyman-α emission (Mason et al. 2018), and constraints on the neutral fraction in the IHM inferred from the spectra of high-redshift quasars (Fan et al. 2006; Mortlock et al. 2011; Bouwens et al. 2015). Measurements of the patchy kinetic Sunyaev–Zeldovich effect in the CMB place limits on the duration of the EOR (Zahn et al. 2012; George et al. 2015), with Planck Collaboration XLVII (2016) setting an upper limit to the width of the reionization period of $\Delta z \lesssim 2.8$.

Improving constraints on the EOR is a major science driver for various observational projects, including the Low Frequency Array

★ E-mail: tsangkeungchan@cuhk.edu.hk

[1]We use the term 'IHM' for the medium outside of haloes, rather than the more conventional 'IGM'. This is because our small high-redshift simulation volume contains few galaxies but many haloes.

(e.g. Greig et al. 2021), the James Webb Space Telescope (e.g. Robertson 2022), and in the near future, the Square Kilometre Array (e.g. Koopmans et al. 2015). On the theory side, several groups have modelled the EOR with simulations in cosmological volumes (with linear extents[2] ∼10–100 cMpc, e.g. Finlator, Davé & Özel 2011; Gnedin 2014; Iliev et al. 2014; Ocvirk et al. 2016; Pawlik et al. 2017; Rosdahl et al. 2018; Doussot, Trac & Cen 2019; Kannan et al. 2022). These simulations use 'subgrid' physics to model unresolved processes, which may introduce degeneracies in the interpretation.

There are three main challenges to our understanding of the EOR: (i) determining the rate at which sources emit ionizing photons, (ii) computing the escape fraction, f_{esc}, of ionizing photons that contribute to ionizing the IHM(rather than being absorbed in the immediate surroundings of where they were produced), and (iii) understanding the nature and evolution of photon sinks, where ionized gas recombines again.

The precise nature of the dominant ionizing sources remains controversial. These could be stars in very faint galaxies below the detection limit of the *Hubble Space Telescope* deep fields (with 1500 Å magnitude $M_{UV} \gtrsim -13$, Robertson et al. 2013; Finkelstein et al. 2019). Another possibility is slightly brighter galaxies that have higher values of f_{esc} because they drive strong winds (Sharma et al. 2016, 2017; Naidu et al. 2020). *JWST* promises to measure the slope of the faint-end luminosity function, which could constrain the contribution of faint galaxies to the emissivity. However, it will remain challenging for observations to constrain f_{esc} directly, although the UV-slope and the dominance of nebular lines in the spectra of galaxies may be good proxies for f_{esc} (e.g. Chisholm et al. 2018, 2022).

In this paper, we focus on challenge (iii): understanding the nature and evolution of photon sinks. Clumpy gaseous structures impede reionization by boosting the opacity (often described in terms of the mean-free path of ionizing photons) and the recombination rate (which consumes ionizing photons) of the IHM.

The recombination rate in an inhomogeneous medium relative to that of a uniform medium is characterized by the 'clumping factor', $c_{l,all} \sim \langle n_{HII}^2 \rangle / \langle n_H \rangle^2$, where $\langle \rangle$ denotes a volume average and n_{HII} and n_H are the density of ionized and total gas. Calculating the clumping factor accurately is challenging. Its numerical value is uncertain, ranging from 2 to 30 (e.g. Gnedin & Ostriker 1997; Iliev et al. 2007; Trac & Cen 2007; Pawlik, Schaye & van Scherpenzeel 2009; McQuinn, Oh & Faucher-Giguère 2011; Raičević & Theuns 2011; Finlator et al. 2012; Shull et al. 2012), depending on its definition and the simulation outcome.

To further exacerbate the issue, a significant number of recombinations occurs in gas inside the smallest gravitationally bound structures: mini-haloes. These are low-mass haloes, $10^4 \lesssim M_h/M_\odot \lesssim 10^8$, not massive enough to form a galaxy (without metals or molecules) but able to retain their cosmic share of baryons before reionization.

Haiman, Abel & Madau (2001) claimed that mini-haloes boost the number of photons that are required to reionize the universe by a factor of ∼10 (although they assumed mini-haloes are optically thin). The semi-analytical model of Iliev, Scannapieco & Shapiro (2005b) and the subgrid model of Ciardi et al. (2006) also suggest that mini-haloes can boost reionization photon budget, based on high-resolution 2D radiation hydrodynamical (RHD) simulations (Shapiro, Iliev & Raga 2004). Emberson, Thomas & Alvarez (2013)

performed a suite of high-resolution cosmological hydrodynamics simulations that resolve all mini-haloes with at least 100 particles. Post-processing these simulations with radiative transfer (hereafter RT), they obtained values of $c_{l,all} \sim 10$, confirming the major impact of small-scale structures on reionization. But Emberson et al. (2013) might have overestimated the clumping factor by not including photoheating and photoevaporation.

Park et al. (2016) performed cosmological RHD simulations with photoevaporation. These calculations resolve mini-haloes, and model the ionizing background as a roughly uniform radiation field with GADGET-RT. But the simulated volumes are relatively small and may not capture the full mass range of mini-haloes. D'Aloisio et al. (2020) performed RHD simulations in a simulation volume with linear extent ∼1 cMpc, using a uniform mesh with cell size ∼1 ckpc (which might be larger than the virial radius of low-mass mini-haloes). Both Park et al. (2016) and D'Aloisio et al. (2020) concluded that $c_{l,all} \sim 10$ during the early stages (≪100 Myr) of reionization, but then drops rapidly to lower values ∼2, due to photoevaporation. But these studies do not explicitly study mini-halo photoevaporation and its impact on reionization, which we investigate here.

Improving upon previous studies, we perform high-resolution (dark matter particle mass ∼100 $M_\odot$ and adaptive spatial resolution <0.1 ckpc) cosmological RHD simulations in volumes of linear extent ∼1 cMpc to investigate the response of gas in small-scale structures on the passage of an ionization front (I-front) and its impact on reionization.

The simulations are performed with the cosmological simulation code SWIFT (Schaller et al. 2018, 2023)[3] with smoothed particle hydrodynamics (SPH, Gingold & Monaghan 1977; Lucy 1977). We model RHD with SPH-M1RT, a novel SPH two-moment method with local Eddington tensor closure (Chan et al. 2021). The simulated volume is large enough to sample the full mass range of mini-haloes (see Section 3.2) and the resolution is high enough to resolve the small mini-haloes.[4]

With this simulation suite, we investigate the mini-halo photoevaporation process and its dependence on redshift and photoionization rate. We study how high-density gas can stall the I-front due to self-shielding. Secondly, we perform a detailed analysis of how the inhomogeneous medium impedes reionization, including the clumping factor, the number of recombination photons, and the role of mini-haloes. We extend upon Chan et al. (2023), which presented only the clumping factor evolution of one of our representative simulations.

This paper is organized as follows. In Section 2, we describe the stages of reionization. We introduce our simulation suite in Section 3. The analysis of the simulations is described in Section 4, focusing on the impact of an I-front on gas in cosmic filaments and mini-haloes. We use these results to gauge the impact of these structures on the progress of reionization (in terms of recombinations and the clumping factor). We put our results in context and discuss them in Section 5. Finally, we conclude with a summary and an outlook for future research. A set of appendices provide the details of our numerical implementation and convergence tests.

This is a long paper, and we recommend the reader to start by skimming through the following sections. First, the definition and discussion around mini-haloes in Section 2.1 (Fig. 1) and the stages of reionization in the beginning of Section 2.2 (Fig. 3). The main

---

[2]The c in cMpc is used to indicate that this is a comoving size; we will use pMpc to indicate proper distances.

[3]https://www.swiftsim.com

[4]For example, a 10^6 $M_\odot$ mini-halo has a virial radius around 0.3 pkpc (or 2 ckpc at $z \sim 6$), compared to our gravitational softening length ∼0.1 ckpc.
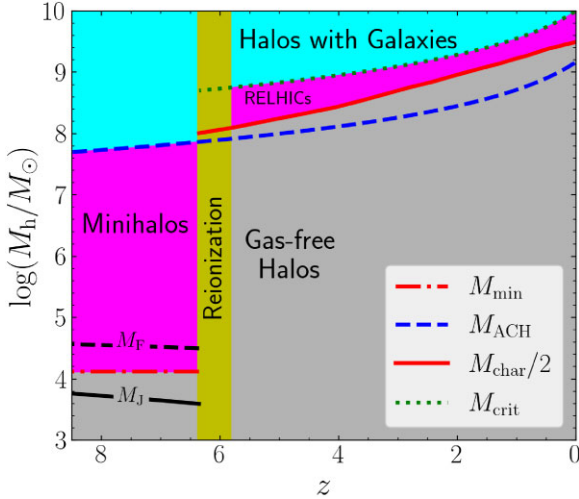
Figure 1. Properties of haloes with different masses as a function of redshift, the vertical band (labelled ``Reionization'') indicates the EOR, assumed to occur around $z \sim 6$. M_J is the Jeans mass (bottom solid line, equation 2), M_F is the filtering mass (bottom dashed line, equation 3), M_{min} is the mass above which haloes contain 50 per cent of the cosmic baryon fraction on average as computed from the simulations (dotted–dashed line between the M_F and M_J lines), M_{ACH} is the halo mass above which gas at the virial temperature can cool atomically (top dashed line, equation 4). Haloes with mass $M_{min} < M_h < M_{ACH}$ are mini-haloes (middle left region). After reionization, M_{char} is the mass above which haloes contain 50 per cent of the cosmic baryon fraction on average as computed by Okamoto, Gao & Theuns (2008, top solid line), and M_{crit} is the mass above which haloes can host a galaxy according to Benitez-Llambay & Frenk (2020, top dotted line). We moved the M_{char} line down since haloes below M_{char} can still hold a small fraction of gas: such haloes can host RELHICs (middle right region, Benítez-Llambay et al. 2017). Haloes in the bottom regions cannot retain a significant fraction of their baryons, whereas haloes in top regions could host a galaxy. Hence, the haloes in the middle regions are photon sinks, whereas those in the top regions host photon sources. The figure also shows that all mini-haloes are photoevaporated during and after the EOR.

results are Figs 13 and 14 in Section 4.4, which quantify the rate at which mini-haloes photoevaporate. Finally, the impact of small-scale structures on reionization is presented in Section 4.5 (Figs 15–17).

2 OVERVIEW AND THEORETICAL ESTIMATES

2.1 Haloes and their role in reionization

The impact of haloes on the IHM pre- and post-reionization depends on their mass. Below some minimum mass, haloes have too shallow potential wells to accrete or retain cosmic gas. The value of this minimum mass depends on the mean temperature of the gas, T_{IHM}. Prior to reionization, T_{IHM} depends on redshift z as (e.g. Furlanetto, Oh & Briggs 2006)

$$T_{IHM} = 2.73 \, (1 + z_{dec}) \left(\frac{1+z}{1+z_{dec}} \right)^2 \, \mathrm{K},$$

$$1 + z_{dec} = 134 \left(\frac{\Omega_b \, h^2}{0.021} \right)^{2/5}. \tag{1}$$

Here, z_{dec} is the redshift where the cosmic gas decouples from the CMB temperature.

We consider the following three estimates of the (pre-ionization) minimum mass:

(i) the Jeans mass, M_J,

$$M_J = \left(\frac{5 k_B T_{IHM}}{G \mu m_H} \right)^{3/2} \left(\frac{3}{4 \pi \, \Omega_M \, \rho_{c,0} (1+z)^3} \right)^{1/2}$$

$$\sim 4.2 \times 10^3 M_\odot \left(\frac{1+z}{9} \right)^{3/2}, \tag{2}$$

(e.g. Mo, van den Bosch & White 2010), where $\mu \approx 1.22$ is the mean molecular weight per hydrogen atom of fully neutral primordial gas. We note that M_J decreases with cosmic time, therefore low-mass haloes need to accrete baryons to reach the cosmic baryon fraction,

(ii) the 'filtering mass', M_F, introduced by Gnedin (2000b) to account for the redshift dependence of T_{IHM},

$$M_F \sim M_J \left[3 \ln \left(\frac{1+z_{dec}}{1+z} \right) - 6 + 6 \left(\frac{1+z}{1+z_{dec}} \right)^{1/2} \right]^{3/2}; \tag{3}$$

see Appendix A for more details,

(iii) M_{min}, the halo mass above which haloes contain on average more than 50 per cent of the cosmic baryon fraction, as determined from the simulations described in Section 3.2.[5]

The IHM temperature increases by almost three orders of magnitude during reionization, and hence so does the minimum mass. We use the simulations of Okamoto et al. (2008) to compute the (post-reionization) minimum mass and refer to it below as M_{char} (the characteristic value of the post-reionization minimum mass). We further define M_{ACH} as the minimum halo mass in which cosmic gas can cool atomically (atomically cooling haloes, ACHs)

$$M_{ACH} \sim 5 \times 10^7 \left(\frac{1+z}{9} \right)^{-3/2} \, M_\odot, \tag{4}$$

and M_{crit} as the halo mass above which stars can form post-reionization according to Benitez-Llambay & Frenk (2020).

Fig. 1 illustrates the evolution of these masses, with the vertical yellow band indicating the assumed EOR. Pre-reionization, M_J and M_F decrease with cosmic time, whereas M_{min} remains approximately constant. Numerically, $M_{min} \approx 2 \times 10^4 \, M_\odot$, which is a factor of a few larger than M_J and a factor of a few smaller than M_F.

Average baryon fractions of haloes (pre-reionization) in units of the cosmic mean are shown in Fig. 2 at various redshifts; the horizontal dotted line indicates 50 per cent. The figure also illustrates that neither M_J nor M_F provides accurate estimates of M_{min}.

In Fig. 1, the left magenta region represents mini-haloes, the main topic of this paper. They are haloes with $M_{min} \lesssim M_h \lesssim M_{ACH}$, which contain their cosmic share of baryons but this gas cannot cool atomically.[6] After reionization, $M_{char} > M_{ACH}$ implies that there are no more haloes that contain gas which cannot cool atomically: all mini-haloes are evaporated during reionization. Such gas-free haloes occupy the grey region.

Finally, the right magenta region represents the 'reionization-limited H I clouds' (RELHICs) in the mass range $M_{char}/2 \lesssim M_h \lesssim M_{crit}$ Benítez-Llambay et al. (2017). They contain a significant amount of gas yet do not host a galaxy.

The main point to take away from Fig. 1 is this: before reionization, to capture all photon sinks requires resolving haloes down to masses

---

[5]We use our highest resolution cosmological simulation 'S512G00', which has a dark matter particle mass of $\sim 10 \, M_\odot$, see Section 3 for details.

[6]We have not indicated the mini-haloes in which Pop III stars can form due to cooling by molecular hydrogen. However, this star formation pathway will likely be suppressed by the photodissociation photons from first stars/galaxies (see Section 5 and Trenti & Stiavelli 2009).
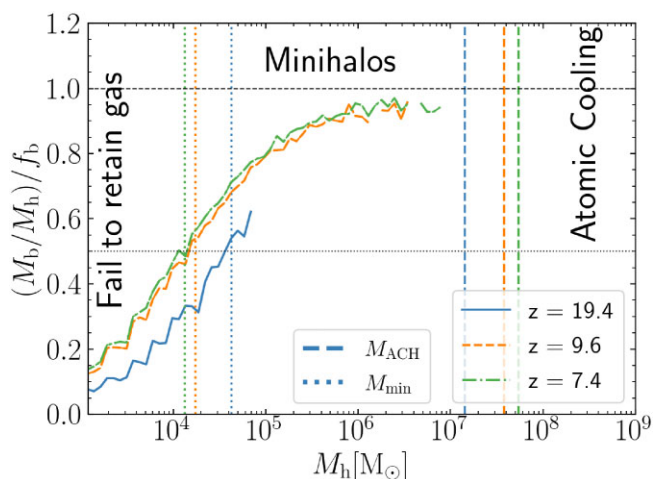
Figure 2. The gas fraction inside haloes at different redshifts before reionization in our highest resolution simulation (S512G00; see Section 3 for details), in units of the cosmic baryon fraction ($f_b \equiv \Omega_b/\Omega_m$). Vertical dotted lines indicate $M_{\min}$, the mass above which the baryon fraction of a halo is $f_b/2$ or more on average (from left to right, for $z = 7.4$, 9.6, and 19.4). Vertical dashed lines indicate the halo mass above which gas at the virial temperature can cool atomically, $M_{\rm ACH}$ (from right to left, for $z = 7.4$, 9.6, and 19.4). Horizontal lines indicate a baryon fraction of $f_b/2$ (dotted) and f_b (dashed). Mini-haloes are haloes with masses between $M_{\rm ACH}$ (vertical dashed) and $M_{\min}$ (vertical dotted).
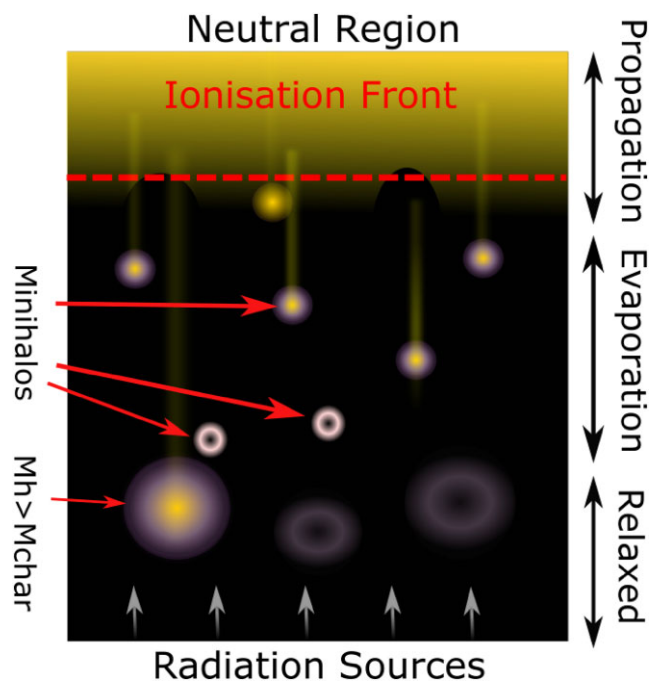
$\sim 10^4$ M$_\odot$.[7] After reionization, haloes with masses $\gtrsim 10^8$ M$_\odot$ are the dominant photon sinks. This highlights the extended range in masses (from $\sim 10^4$ to $\gtrsim 10^8$ M$_\odot$) of photon sinks during and after EOR.

2.2 The progression of the reionization process

We divide the EOR into three characteristic evolutionary phases, (i) the I-front propagation phase, (ii) the mini-halo evaporation phase, and (iii) the relaxed phase. These phases are illustrated in Fig. 3 and described below:

(i) *(I-front) Propagation phase:* the R-type.[8] I-front propagates at a small fraction of the speed of light, ionizing, and heating the low-density IHM. Haloes more massive than a minimum mass, $M_{\min}$, contain a large fraction of their cosmic complement of baryons, and this gas is dense enough to self-shield and hence initially remains neutral. Dense gas in such haloes significantly increases the recombination rate compared to that of a uniform IHM. At the end of this phase, the neutral, high-density, self-shielded gas in haloes is embedded in a highly ionized IHM.

(ii) *(Mini-halo) Evaporation phase:* the I-front propagates into haloes, ionizing the gas in their outskirts. In haloes more massive than a minimum mass, $M_{\rm char}$, most of this ionized gas does not photoevaporate, and their inner parts remain self-shielded. In contrast, the gas in lower mass haloes photoevaporates at a speed slower than the sound speed, taking 10–100 of Myrs to complete.[9] Such mini-haloes are very numerous, and their photoevaporation consumes a

[7]However, X-ray preheating can relax this resolution requirement (see Section 5 for more discussions).
[8]The terms 'R-type' (rarefied) and 'D-type' (dense) I-fronts were coined by Kahn (1954) (see e.g. Osterbrock & Ferland 2006, for details).
[9]The gas evaporates slower than the sound crossing time because I-fronts are trapped inside haloes and propagate at subsonic speed (Shapiro et al. 2004).

Figure 3. A schematic picture of the three stages of reionization, in which an initially planar I-front (top dashed line) moves upwards in the diagram. In the lower part of the diagram, the IHM is highly ionized (dark region) except in haloes with mass above a characteristic mass, $M_{\rm char}$. The outskirts of the gas in these haloes are highly ionized but the haloes' potential wells are deep enough that the gas cannot photoevaporate: these are LLSs. The inner parts of the haloes can self-shield, and the gas is neutral; these are damped Lyman-α systems (solid discs). In the middle part of the diagram, the I-front has passed only recently, and the gas in mini-haloes is still photoevaporating (hollow circles). The I-front has not yet reached the top of the diagram, where the IHM is still neutral (top light region). Light vertical stripes are regions where gas remains neutral due to the shadowing of the ionizing radiation by an intervening self-shielded region. The I-front is slowing down and becomes increasingly corrugated rather than planar as a result of the density inhomogeneities in the IHM.

large number of ionizing photons, comparable to the number of photons needed to reionize the IHM (e.g. Shapiro et al. 2004; Iliev, Shapiro & Raga 2005a). At the end of this phase, all mini-haloes are photoevaporated. Only haloes more massive than $M_{\rm char}$ contain significant amounts of gas.

(iii) *(Post-reionization) Relaxed phase:* the I-front also propagates into haloes more massive than mini-haloes, but their deeper potential wells prevent them from photoevaporating. These photon sinks correspond to Lyman-limit (the ionized outskirts of the haloes) and damped-Lyman-α systems (the self-shielded inner parts, hereafter referred to as LLS's and DLA's, see e.g. Theuns 2021). After reionization, these structures are mainly responsible for determining the opacity, the recombination rate and the clumping factor.

2.2.1 (I-front) Propagation phase

Consider the case of an initially planar I-front propagating through a (nearly) uniform IHM which is fully neutral at time $t = 0$. The speed of the I-front along its propagation direction,[10] which we assume to

[10]This also neglects collisional ionization and the presence of helium.

be the Z-axis, is

$$\frac{dZ}{dt} = \frac{F}{\langle n_H \rangle} - \alpha_B (1-x)^2 \langle n_H \rangle Z \,, \tag{5}$$

where $\langle n_H \rangle$ is the (mean) hydrogen density by number, x is the neutral fraction at coordinate Z of the gas once it is ionized, and α_B is the temperature-dependent recombination coefficient. The solution to this differential equation is

$$Z = Z_S \left[1 - \exp(-t/t_r) \right] \,, \tag{6}$$

provided we assume that the gas downstream of the I-front is highly ionized, $x \ll 1$. Here,

$$t_r = \frac{1}{\alpha_B(T_{IHM}) \langle n_H(z) \rangle} \approx 2.1 \left(\frac{1+z}{9} \right)^{-3} \text{Gyr} \,,$$

$$\frac{dZ}{dt} = \frac{Z_S}{t_r} \exp\left(-\frac{t}{t_r}\right)$$

$$\approx 4.7 \times 10^3 \exp\left(-\frac{t}{t_r}\right) \left(\frac{\Gamma_{-12}}{0.1} \right) \left(\frac{1+z}{9} \right)^{-3} \text{km s}^{-1}$$

$$Z_S = \frac{F t_r}{\langle n_H \rangle} \approx 11 \left(\frac{\Gamma_{-12}}{0.1} \right) \left(\frac{1+z}{9} \right)^{-6} \text{pMpc} \,, \tag{7}$$

where t_r is the recombination time and Z_S is the 1D analogue of the Strömgren radius.[11] The photoionization rate, Γ, is related to F by

$$\Gamma = F \sigma_{HI} = 1.62 \times 10^{-13} \left(\frac{F}{10^5 \text{cm}^{-2} \text{s}^{-1}} \right) \text{s}^{-1}$$

$$\equiv \Gamma_{-12} \, 10^{-12} \text{s}^{-1} \,, \tag{8}$$

and the case-B recombination rate is

$$\alpha_B(T) \approx 1.1 \times 10^{-13} \left(\frac{T}{2.2 \times 10^4 \text{K}} \right)^{-0.7} \text{cm}^3 \text{s}^{-1} \,. \tag{9}$$

The numerical values in equation (8) assume that the ionizing spectrum is that of a blackbody with effective temperature $T_{BB} = 10^5$ K, for example, massive stars, which yields a frequency-averaged photoionization cross-section,[12] of $\sigma_{HI} = 1.63 \times 10^{-18}$ cm^2. The temperature of the IHM is $T_{IHM} \approx 2.2 \times 10^4$ K after being flash ionized by such an ionizing spectrum (e.g. Chan et al. 2021).

The I-front's propagation speed is considerably slower than the speed of light. Note that the location of the Strömgren layer, Z_S, itself evolves as the Universe expands (see e.g. Shapiro & Giroux 1987 for a more accurate calculation of the evolution of such H II regions). Equation (7) also shows that the recombination time at the mean density, t_r, is longer than the age of the Universe, $t_U = 2/(3H(z)) = 0.65 (9/(1+z))^{3/2}$ Gyr, at a redshift, $z \lesssim 8$. Gas in mini-haloes is at a higher density and hence has a shorter recombination time, thus slowing down the I-front until the gas photoevaporates.

2.2.2 (Mini-halo) Evaporation phase

The dense gas in mini-haloes traps the I-front. The response of the gas, when overrun by the I-front, depends on ratios of three time-scales: (i) the sound-crossing time t_{sc}, (ii) the I-front crossing time t_{ic}, and (iii) the recombination time $t_{r, h}$.

The sound-crossing time is the time for a sound wave to travel a distance equal to the virial radius, R_h, of the halo,

$$t_{sc} = \frac{R_h}{c_s}$$

$$\sim 7.0 \left(\frac{1+z}{9} \right)^{-1} \left(\frac{M_h}{10^5 M_\odot} \right)^{\frac{1}{3}} \left(\frac{T}{2.2 \times 10^4 \text{K}} \frac{0.6}{\mu} \right)^{-\frac{1}{2}} \text{Myr} \,, \tag{10}$$

where M_h is the virial mass of the halo and c_s is the sound speed, which we evaluated at the temperature of the IHM after flash ionization (Chan et al. 2021).

The I-front propagating time, t_{ic}, is the time it takes for an I-front to cross a mini-halo, neglecting recombinations,

$$t_{ic} = \frac{\Delta \langle n_H \rangle R_h}{F}$$

$$\sim 6.6 \left(\frac{\Delta}{200} \right) \left(\frac{1+z}{9} \right)^2 \left(\frac{0.1}{\Gamma_{-12}} \right) \left(\frac{M_h}{10^5 M_\odot} \right)^{\frac{1}{3}} \text{Myr} \,. \tag{11}$$

Finally, the mean recombination time of the gas in a halo, $t_{r, h}$, is:

$$t_{r,h} = \frac{1}{c_{mh} \Delta \langle n_H \rangle \alpha_B}$$

$$\sim 5.4 \left(\frac{1+z}{9} \right)^{-3} \left(\frac{c_{mh}}{2} \right)^{-1} \left(\frac{\Delta}{200} \right)^{-1} \text{Myr} \,. \tag{12}$$

We evaluated the case-B recombination coefficient at a temperature, $T = 2.2 \times 10^4$ K, Δ is the gas overdensity which we set to 200 (e.g. Mo et al. 2010). Furthermore, c_{mh} is the clumping factor of the gas inside a mini-halo; in the simulations discussed below, we find typical values for c_{mh} in the range 2–4. The values of these three times are similar for our default choice of parameters, for example, a halo mass of $M_h = 10^5$ M$_\odot$ and a photoionization rate with $\Gamma_{-12} \sim 0.1$. The dependence on halo mass is the same for t_{ic} and t_{sc}, but the redshift dependence differs; t_r does not depend on M_h. Depending on the values of z and M_h, we identify the three following regimes:

(i) *Sound-speed limited regime:* when $t_{ic} \ll t_{sc}$, the I-front races through a mini-halo so quickly that its gas cannot recombine nor react hydrodynamically. The gas is ionized and heated and will photoevaporate[13] on a time-scale, $t \sim t_{sc}$. This is typically the case for low-mass haloes, at low redshift, and when Γ_{-12} is large.

(ii) *Ionization limited regime:* when $t_{sc} \ll t_{ic}$, the I-front moves slowly and the gas can photoevaporate as soon as it ionizes: this also implies that the total gas density tracks the ionized gas density.

(iii) *I-front trapping regime:* if $t_r \ll t_{ic}$, the gas is photoionized, but recombines very quickly.[14] The I-front moves at subsonic speeds and eventually nearly stalls at the inverse Strömgren layer (ISL, Shapiro et al. 2004). This regime occurs in haloes of mass, $M_h \gtrsim 10^6$ M$_\odot$, and in the central dense region of low-mass haloes.

In principle, the duration of the photoevaporation phase is not simply established by the time it takes to photoevaporate the most massive mini-haloes. It is because low-mass mini-haloes may contribute more to the recombination rate since they are much more numerous. We will use the simulations described below to estimate the duration of this phase.

---

[11]Using the value of dZ/dt suggests that it would take of order $\gtrsim 10$ Myr for an I-front to cross 1 Mpc. In fact, it takes considerably longer than this, because of density inhomogeneities and recombination.

[12]Our value differs from that of Emberson et al. (2013) because we use a different spectral shape.

[13]I-front trapping can still occur in the central dense regions of small haloes where the recombination time is short, see Shapiro et al. (2004). If this core is small, it may not affect reionization significantly.

[14]These I-fronts are D-type (dense-type). See e.g. Draine (2011).

2.2.3 (Post-reionization) Relaxed phase

Long ($\gg 100$ Myr) after being overrun by the I-front, haloes with $M_h < M_{char}$ are photoevaporated and unable to accrete gas (Okamoto et al. 2008): such haloes no longer contribute to recombination. Gas in the outskirts of more massive haloes is highly ionized, with the inner parts self-shielded and neutral. These LLS's and DLA's determine the attenuation length of ionizing photons, and thereby the relationship between the emissivity of ionizing photons and the photoionization rate (e.g. Faucher-Giguère et al. 2009; McQuinn et al. 2011; Haardt & Madau 2012).

Cosmological RHD simulations are required to capture the propagation and evaporation phases and the transition to the post-reionization phase. To resolve photon sinks during these stages, such simulations must resolve mini-haloes above the Jeans mass in a computational volume that is large enough to sample the rarer LLS's and DLA's that determine the mean-free path of ionizing photons in the post-reionization phase. This is a tall order, even if we neglect the even more challenging calculation of resolving the nature of the ionizing sources and the thorny issue of determining the fraction of those photons that can escape their natal cloud. In this paper, we focus on photon sinks during the EOR: we simply inject ionizing photons into our computational volume at a specified rate and follow how these photoevaporate gas out of small haloes.

3 SIMULATIONS

3.1 Code and numerical set-up

We simulate a periodic cubic cosmological volume using the publicly available,[15] SPH code SWIFT (Schaller et al. 2016, 2018). Among the various implementations of the SPH algorithms (e.g. Borrow et al. 2022) included in the code, we select the entropy-based version described by Springel & Hernquist (2002) and Springel (2005).

RHD is solved with the SPH-M1RT two-moment method with a modified M1 closure,[16] as described by Chan et al. (2021). A uniform, constant flux of ionizing radiation is injected into the computational volume from two opposing faces of the cubic volume. We consider a simulation suite in which we vary the redshift when we start injecting photons, z_i, and the intensity of the radiation, Γ_{-12}. The spectrum of the radiation is that of a blackbody of temperature, $T_{BB} = 10^5$ K, and is treated in a single frequency bin using the grey approximation; this also means that we neglect any spectral hardening of the radiation. The optically thin direction of the Eddington tensor is taken to be along the initial direction of propagation of the I-front; this improves the ability of the method to cast shadows and handle self-shielding. To reduce the computational cost, we propagate radiation at a reduced speed of light, $\tilde{c}$ (Gnedin & Abel 2001). In our implementation, $\tilde{c}$ scales with the value of the smoothing lengths of the SPH particles.[17] The interaction of radiation with matter is calculated with a non-equilibrium thermo-chemistry solver with hydrogen only (as in Chan et al. 2021). We include helium when calculating the heat capacity,

---

but we do not consider its interaction with radiation. Note that we also neglect molecular hydrogen and other elements (see Section 5 for a discussion on the caveats of our approach). Our original RT implementation did not account for the cosmological redshifting of radiation. We describe and test in Appendix C our choice of comoving variables. Our implementation accounts for the decrease in the proper density of photons as the Universe expands, but it does not account for the increase in the wavelengths of these photons. The mean-free path of ionizing photons is short in the case we simulate here. Therefore, this is a reasonable approximation.

Our simulation suite does not include feedback from evolving stars. However, as very dense gas particles severely limit the simulation time-step, and since we do not include the correct physics for these high-density regions anyway, we simply convert gas particles into stars once their density exceeds a physical density of 10 hydrogen atoms per cm³ and an overdensity of $\Delta = \rho/\langle\rho\rangle = 10^3$. These criteria are similar to the 'quick-Lyα' approximation used by, for example, Viel, Haehnelt & Springel (2004), who pointed out that the impact of this approximation on the Lyα flux power spectrum is small (less than 0.2 per cent). Moreover, the density of gas particles that turn into stars is higher than that of the regions that give rise to LLSs. This indicates that our approximation is unlikely to affect the I-front speed or the photoevaporation time-scales of mini-haloes (see further discussions on this in Section 5).

We generate the initial conditions at redshift $z = 127$, using the publicly available MUSIC code (Hahn & Abel 2011). The adopted cosmological parameters are: $h = 0.678$, $\Omega_m = 0.307$, $\Omega_\Lambda = 0.693$, and $\Omega_b = 0.0455$, $\sigma_8 = 0.811$, and $n_s = 0.961$, where symbols have their usual meaning. The hydrogen and helium mass fractions are $X = 0.752$ and $Y = 1 - X$, respectively. We use equation (1) to compute the temperature at the mean density, T_{IHM}, which gives the normalization of the adiabat describing the temperature–density relation of the particles in the initial conditions, $T_{ini}(\rho)$:

$$T_{ini}(\rho) = T_{IHM} \left(\frac{\rho}{\langle\rho\rangle}\right)^{2/3} \equiv T_{IHM} \Delta^{2/3}. \tag{13}$$

3.2 Simulation suite

Our main objective is to study the photoevaporation of mini-haloes and how this impacts the progression of reionization. This requires sampling and resolving mini-haloes from the Jeans mass, M_{min}, to the atomic cooling limit, M_{ACH} (see Fig. 1). We vary the redshift at which we start injecting radiation and the flux of the injected ionizing photons and run individual simulations until several 100 Myr after the radiation injection. Simulation parameters are listed in Table 1. We motivate the choices as follows.

We set the dark matter particle mass of the fiducial simulations to $m_{DM} \sim 100\,M_\odot$, so that a halo of mass M_{min} (see Section 2) is resolved with ~ 300 particles. The baryonic content of such haloes is resolved with roughly 30 per cent accuracy (Naoz, Barkana & Mesinger 2009) and the overall clumping factor of the simulated volume is accurate to ~ 10 per cent $- 20$ per cent (Emberson et al. 2013).

To include massive haloes of mass $\sim M_{ACH}$, we consider a fiducial linear extent of 800 ckpc. We demonstrate in Fig. D8 that such a volume contains more than one halo of mass M_{ACH} at $z = 8$, and 10 at $z = 6$. This linear extent also yields approximately converged values for the mean-free path of ionizing photons at the end of the EOR (for unrelaxed gas; see Emberson et al. 2013).[18]

---

[15] http://www.swiftsim.com

[16] Wu, McQuinn & Eisenstein (2021) suggested that the M1 method, the approach here, overionizes absorbers with idealized calculations, assuming uniform radiation coming from infinity. However, their argument is not applicable to the case here where radiation is plane parallel. The accuracy of our method with a plane-parallel radiation field is demonstrated in Appendix E.

[17] See Appendix B for more details on this 'variable' speed of light approximation.

[18] Emberson et al. (2013) did not consider the effect of photoheating and thus photoevaporation. However, if photoheating is included, haloes with

Table 1. Details of the simulation suite. From left to right: simulation identifier, linear extent of the simulated volume L_{box}, redshift of reionization z_i, photoionization rate in units of $10^{-12} s^{-1}$, Γ_{-12}, number of gas and dark matter particles, N, gas particle masses m_{gas}, dark matter particle masses m_{DM}, gravitational softening lengths l_{soft}, reduced speed of light at the mean density, $\tilde{c}$, and mean hydrogen density, $\langle n_H \rangle$, at z_i. The simulation identifier encodes the extent of the simulated volume, the number of particles, the value of z_i and the value of Γ_{-12}.

Sim	L_{box} [ckpc]	z_i	Γ_{-12}	N	m_{gas} [$M_\odot$]	m_{DM} [$M_\odot$]	l_{soft} [kpc]	$\tilde{c}$ [c]	$\langle n_H \rangle$ [cm^{-3}]
Validation									
S128z8G03	400	7.9	0.3	128^3	160	960	0.3	0.15	1.2×10^{-4}
S256z8G03c001	400	7.9	0.3	256^3	20	120	0.1	0.01	1.2×10^{-4}
S256z8G03c005	400	7.9	0.3	256^3	20	120	0.1	0.05	1.2×10^{-4}
S256z8G03c01	400	7.9	0.3	256^3	20	120	0.1	0.1	1.2×10^{-4}
S256z8G03c02	400	7.9	0.3	256^3	20	120	0.1	0.2	1.2×10^{-4}
S256z8G03c05	400	7.9	0.3	256^3	20	120	0.1	0.5	1.2×10^{-4}
S256z8G003c001	400	7.9	0.03	256^3	20	120	0.1	0.01	1.2×10^{-4}
S256z8G003c005	400	7.9	0.03	256^3	20	120	0.1	0.05	1.2×10^{-4}
S256z8G003c01	400	7.9	0.03	256^3	20	120	0.1	0.1	1.2×10^{-4}
S256z8G003c02	400	7.9	0.03	256^3	20	120	0.1	0.2	1.2×10^{-4}
S512z8G00	400	7.9	0.0	512^3	2.5	15	0.05	–	1.2×10^{-4}
M128z8G03	800	7.9	0.3	128^3	1300	7700	0.4	0.15	1.2×10^{-4}
M256z8G03	800	7.9	0.3	256^3	160	960	0.3	0.15	1.2×10^{-4}
L512z8G03	1600	7.9	0.3	512^3	160	960	0.3	0.15	1.2×10^{-4}
L512z8G01	1600	7.9	0.1	512^3	160	960	0.3	0.05	1.2×10^{-4}
Production									
M512z6G03	800	6.0	0.3	512^3	20	120	0.1	0.15	6.0×10^{-5}
M512z6G003	800	6.0	0.03	512^3	20	120	0.1	0.05	6.0×10^{-5}
M512z8G03	800	7.9	0.3	512^3	20	120	0.1	0.15	1.2×10^{-4}
M512z8G015	800	7.9	0.15	512^3	20	120	0.1	0.075	1.2×10^{-4}
M512z8G003	800	7.9	0.03	512^3	20	120	0.1	0.05	1.2×10^{-4}
M512z10G03	800	10.2	0.3	512^3	20	120	0.1	0.15	2.5×10^{-4}

We perform simulations with three choices of the 'reionization redshift', $z_i \sim 10$, 8, and 6 (z_i is the redshift where we start injecting ionizing photons from two opposing faces of the cubic volume at constant flux). This range covers approximately current observational estimates for the start and tail-end of the EOR (e.g. Fan et al. 2006; Planck Collaboration VI 2020). The values of F correspond to photoionization rates of $\Gamma_{-12} = 0.03$–0.3 (where F and Γ_{-12} are related by the frequency-averaged photoionization rate, as in equation 8). This range in Γ_{-12} is motivated by observational estimates (e.g. Calverley et al. 2011; Wyithe & Bolton 2011; D'Aloisio et al. 2018) as well as simulation results (e.g. Rosdahl et al. 2018).

We take the value of the reduced speed of light to be proportional to that of the I-front: this allows us to use a lower value of $\tilde{c}$ at lower Γ_{-12}, decreasing the wall-clock time of the simulations (see Appendix D for tests of numerical convergence). Once the majority of the IHM is ionized, that is, at the start of the evaporation phase of the EOR, most I-fronts are expected to be D-type and hence propagate locally at a speed comparable to the sound speed, which is much slower than the speed of light. Therefore, we set $\tilde{c} = c/100$ once the mass-weighted neutral hydrogen fraction drops below 5 per cent (see the similar approach and convergence tests in D'Aloisio et al. 2020).

Finally, note that the simulated volumes are all relatively small and are not necessarily representative cosmological volumes during the EOR. Rather we think of them as selected patches of the Universe

that are overrun by an I-front due to sources outside of the simulated volume. These patches are ionized at various redshifts, z_i, and with a range of values of the photoionization rate, Γ_i.
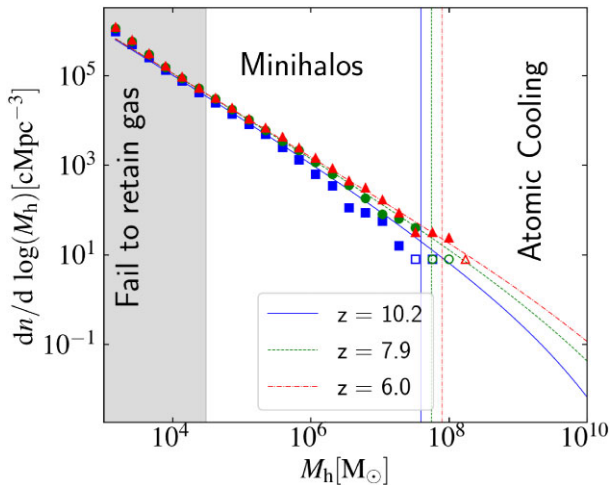
3.3 Halo identification

We use NBODYKIT (Hand et al. 2018) to identify haloes using the friend-of-friend algorithm (Davis et al. 1985), as simply connected regions with a mean density of ∼200 times the average density of the Universe. The halo mass function of our simulations at redshifts before z_i is compared to that computed with the COLOSSUS PYTHON package,[19] (Diemer 2018) in Fig. 4 (we selected the Reed et al. 2007 fit). The agreement between the simulation results and the fit indicates that our small volume contains the expected number of mini-haloes up to the mass of atomic-cooling haloes, as desired. We have performed additional runs in which we vary the box size and numerical resolution, see Appendix D.

4 RESULTS

4.1 Overview

We illustrate the first two reionization phases – I-front propagation and mini-halo evaporation – using the M512z8G03 run. In this simulation, ionizing photons are injected after redshift $z_i = 7.87$, with a constant flux equivalent to a photoionization rate of $\Gamma_{-12} = 0.3$. The value of z_i falls around the mid-point of the EOR as inferred from the Thompson optical depth (Planck Collaboration XLVII 2016), and the value of Γ_{-12} is typical of the expected mean value during this

virial mass below the characteristic mass found by Okamoto et al. (2008) will eventually photoevaporate, with more massive haloes determining the clumping factor. An accurate calculation of the clumping factor then requires an even larger volume. To study this situation, our simulation suite includes larger volumes simulated at lower resolution.

[19]https://bdiemer.bitbucket.io/colossus/

Figure 4. Symbols: halo mass function of the fiducial simulation (M512) at three different redshifts, and lines show the fitting functions from Reed et al. (2007). Colours correspond to $z = 10.2$ (squares and solid line), $z = 7.9$ (circle and dotted line), and $z = 6.0$ (triangles and dashed line). Empty symbols show mass bins with fewer than 5 haloes per decade in halo mass. The thin vertical lines on the right show the minimum mass of atomic cooling haloes (equation 4); haloes in the shaded region are not well resolved, containing fewer than 300 dark matter particles. Our fiducial simulation resolves mini-haloes with more than 300 particles in a volume sufficiently large to contain a few haloes in which gas can cool atomically.

time ($\Gamma_{-12} = 0.3, \ldots, 0.6$, e..g D'Aloisio et al. 2018). Therefore, this setup simulates the history of a typical patch of the universe during the EOR. The evolution of the other simulations is qualitatively similar to that of M512z8G03. Simulations with higher values of z_i have fewer self-shielded clouds since structure formation is less advanced, and those at lower z_i or higher values of Γ_{-12} have more self-shielded clouds.

Fig. 5 shows the simulated volume at $z = 7.84$, which is ~3 Myr after ionizing photons were first injected (propagation phase, upper row), when the I-front has propagated over approximately 1/6th of the simulation volume. Using equation (5) with $\alpha_B = 0$ for the speed of the I-front in a homogeneous medium, we would expect an I-front to cross the computational volume in a time $\sim \langle n_H \rangle L / F \sim 6$ Myr (where L is the proper box size and F is photon flux) if recombination could be neglected. Clearly, density inhomogeneities, and in particular mini-haloes, slow down the I-front by a factor ~ 2—3 on average. The top row shows how the initial planar I-front becomes corrugated. This is because high-density regions locally slow down the front, as opposed to low-density regions which increase the front speed. Sufficiently dense gas in haloes may even stop the I-front casting a shadow of gas that remains neutral behind them. Downstream of the I-front, the highly ionized gas is also photoheated, reaching a temperature of $T \sim 2 \times 10^4$ K in a time-scale of order Γ^{-1} (photoionization rate; see equation 8). The middle panel shows that the I-front is sharp, with the distance from where the gas is mostly ionized to where it is mostly neutral of around

$$d_{\text{IF}} \sim 1/(\langle n_H \rangle \sigma_{\text{HI}}) \sim 1.4 \text{ pkpc} \left(\frac{1+z}{9} \right)^{-3}. \tag{14}$$

Therefore, the IHM during the EOR is either highly ionized or mostly neutral, to a good approximation.

The lower row of Fig. 5 corresponds to $z = 7.58$ (~30 Myr from the start of photon injection) when more than 99 per cent of the

volume has been highly ionized. When the I-front has already crossed the computational volume, it leaves behind filaments and haloes with mostly neutral and cold gas. The lower-left panel shows that these filaments are photoevaporating, with gas expanding out of the shallow potential well once it is ionized and heated (see also Bryan et al. 1999). The flow velocity is comparable to the local sound speed. These expansion waves compress and heat the gas in the filaments' outskirts, as seen in the lower right panel, where hotter gas surrounds the expanding cooler filaments. The denser gas in mini-haloes takes longer to fully photoevaporate, and sufficiently massive haloes retain most of their baryons.

This discussion suggests assigning gas to three categories: (1) the low-density IHM, for example, voids; (2) the filaments of the cosmic web; and (3) collapsed haloes including mini-haloes. These structures stand out in the top left panel of Fig. 5. To investigate how these structures are impacted by reionization and vice versa how they affect reionization, we proceed as follows. In Section 4.2, we investigate the impact of I-front on the IHM and filaments, and in Section 4.3, study how self-shielding keeps the central parts of mini-haloes neutral. In Section 4.4, we will turn to the photoevaporation of mini-haloes. In Section 4.5, we will quantify how these small-scale structures impede reionization and the role of photoevaporation/relaxation.

4.2 Response of the IHM to reionization

We examine the volume density distribution of our simulations in Fig. 6. Here, we plot $\Delta^3 \mathcal{P}_V(\Delta)$ as a function of $\log \Delta$. We show these curves for the total gas density (solid blue) and ionized gas density (dashed blue). First, we study the response of the IHM to the passing of I-front for the simulation M512z8G03 (left panel) quantitatively. Upon the passage of I-front, low-density ($\Delta < 5$) gas got highly ionized and heated to $T \sim 2 \times 10^4$ K (see also Fig. 7). But this gas changes relatively little in volume density (since it cannot expand further). On the other hand, self-shielded gas at high density ($\log \Delta > 3$) remains mostly neutral and cold, whose P_V also is not strongly affected by reionization due to self-shielding. Photoheating significantly reduces P_V of intermediate densities, $\log \Delta \sim 1$–3, since this gas is not self-shielded and expanded after photoheating. More detailed analysis (including particle tracking) is presented in Appendix F.

Other curves in Fig. 6 show the total gas density probability distribution (PDF's) for all gas in haloes (dashed orange), haloes in the mass range $\log M_h[M_\odot] > 8$ (green dashed), $7 < \log M_h[M_\odot] < 8$ (pink dotted), $6 < \log M_h[M_\odot] < 7$ (brown solid) $5 < \log M_h[M_\odot] < 6$ (purple dashed) and $\log M_h[M_\odot] < 5$ (grey dashed). The top panels correspond to the beginning of reionization when the I-front is still traversing the volume; the lower panels are at redshift $z = 5$. Panels from left to right correspond to different values for z_i and Γ_{-12}, as indicated. The straight black dashed line shows $\mathcal{P}_V \propto \Delta^{-2.5}$, which corresponds to the PDF slope of an isothermal profile (see Miralda-Escudé, Haehnelt & Rees 2000 and discussions below).

In the left panel, we can see how haloes with $\log M_h < 7$ photo-evaporate, with their contribution to the high-density PDF $\log \Delta > 2$, decreasing dramatically between $z = 6$ and 5. The intermediate-density gas, $1 < \log \Delta < 3$, is mostly associated with the more massive haloes, $\log M_h > 8$.

The middle panels correspond to a case with $z_i = 8$ and a lower photoionization rate of $\Gamma_{-12} = 0.03$ as compared to $z_i = 6$ and $\Gamma_{-12} = 0.3$. Nevertheless, the PDF's at $z = 5$ are quite similar, with the most striking difference being the location of the upturn in the PDF, which occurs around $\log \Delta = 2.6$ in the left panel and $\log \Delta =$
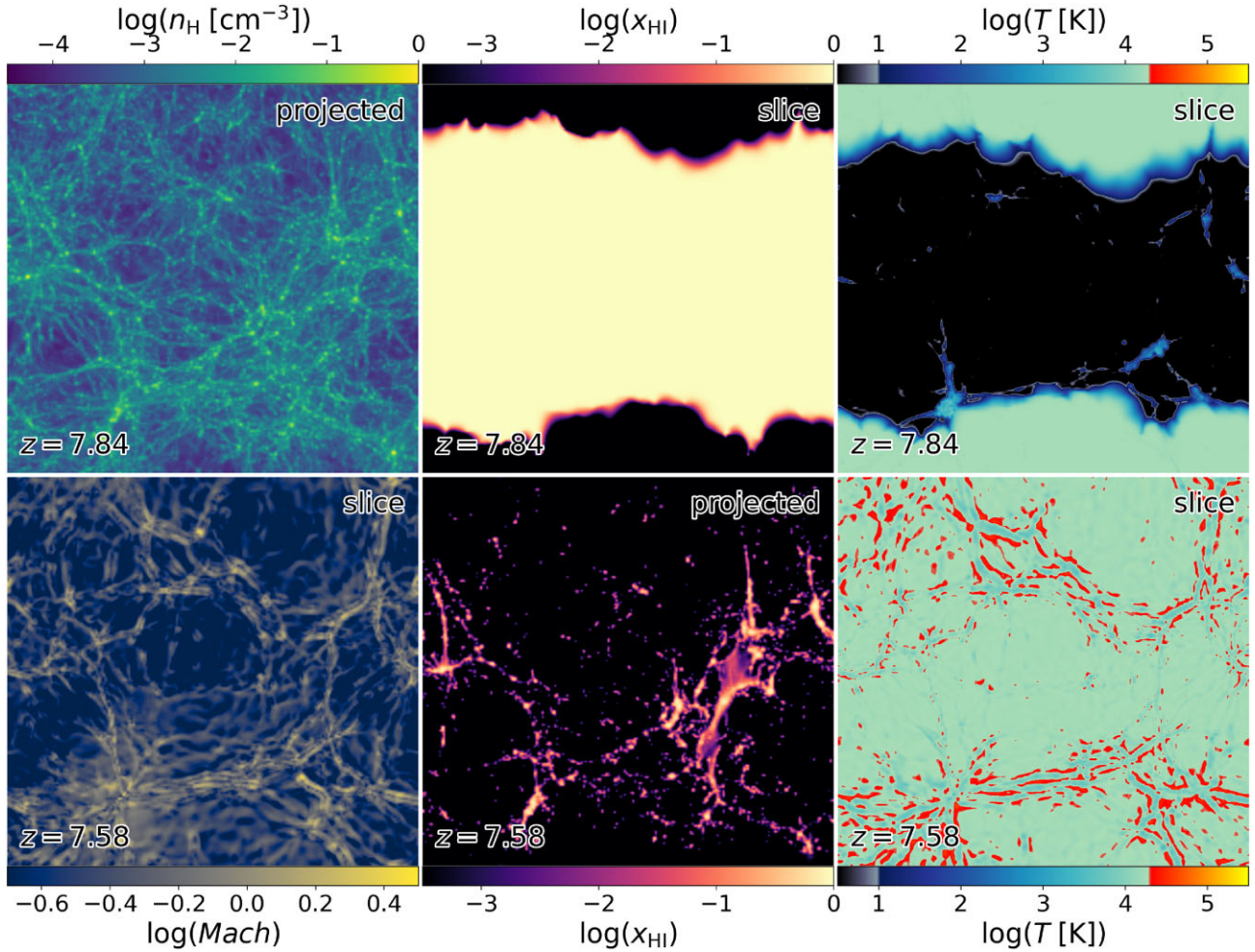
Figure 5. Impact and response of gas structures to the passage of I-fronts, entering the computational volume simultaneously from the top and the bottom. Individual panels visualize slices/projections of the M512z8G03 simulation box at $z = 7.84$ (upper panels) and $z = 7.58$ (lower panels). Radiation is injected at redshift $z_i \approx 8$. Panels from left to right are hydrogen gas density (n_H) (Mach number in the lower left), the neutral fraction (x_{HI}), and the gas temperature (T). Panels labelled 'projected' correspond to projections of the computational volume; the others correspond to infinitesimally thin slices through the mid-plane. As the I-front propagates through the volume, gas becomes ionized and photoheated, and mini-haloes photoevaporate. Photoheating causes the expansion of the filaments.

2 in the middle panel. We note that this upturn is also the location where the gas turns from mostly ionized to mostly neutral.

The right panels correspond to a model with $z_i = 10$ and $\Gamma_{-12} = 0.3$. Although this model has the same value of the photoionization rate as the model in the left panel, the PDF's look strikingly different, with, in particular, very little gas at high densities. The reason for this becomes clear by comparing the top panels: the more massive haloes have not formed yet by $z \sim 10$, and these haloes do not accrete gas once it is photoheated. This shows that reionization has a bigger impact on more massive haloes by preventing them from accreting hot gas rather than by photoevaporating their gas.

Miralda-Escudé et al. (2000) found that the gas PDF is described well by the form $\mathcal{P}_V \propto \Delta^\gamma \exp(-\Delta^{4/3}/\sigma_\Delta^2)$, where $\gamma(= -2.5)$ and σ_Δ are fitting parameters. Their model is based on simulations with uniform UV background and the optically thin approximation (Miralda-Escudé et al. 1996).

With full RHD here, our result (Fig. 6) does not agree with Miralda-Escudé et al. (2000, compared with the $\gamma = -2.5$ scaling in Fig. 6). Our PDF has a stronger dip at $\log \Delta \sim 2$, followed by a stiff profile at higher density. With RHD, we capture the self-

shielding of gas inside haloes, which is less affected by the radiation, so the dense gas can maintain a stiff profile. The ionized gas, on the other hand, is photoheated and evaporated, which explains the dip at $\log \Delta \sim 2$.

McQuinn et al. (2011) also showed a drop in gas density (at $\delta \sim 10^2$) compared to Miralda-Escudé et al. (2000). They turned off ionization background for $n_H > 10^{-2} \text{cm}^{-3}$ and consider self-shielding with pro-process RT. A dip in the PDF around $\delta \sim 10^2$ was also found in other high-resolution RHD simulations, for example, Park et al. (2016) and D'Aloisio et al. (2020). These results support that the self-shielding of gas is responsible for the deviation from Miralda-Escudé et al. (2000).

The processes described here can be visualized in the temperature–density diagrams of Fig. 7, before (upper panel) and after (lower panel) the passage of the I-front. The gas in the simulations has an initial entropy, $T/\rho^{\gamma-1}$, at the start of the calculations, set by the initial temperature of the gas (equation 13). This initial entropy is shown by the diagonal dotted line. But the gas can increase its entropy and move upwards from the dotted line through shocks during structure formation.
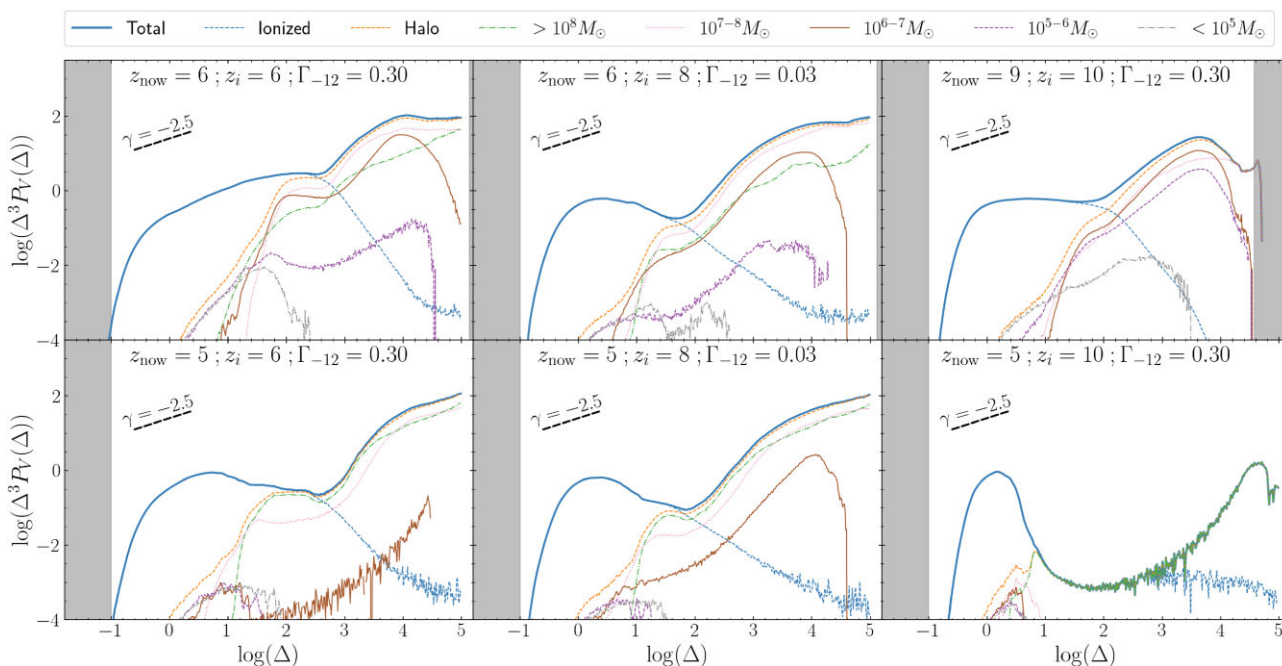
Figure 6. PDF by volume multiplied by Δ^3, $\Delta^3\mathcal{P}_V$, as a function of the logarithm of the overdensity, $\log\Delta$. In the top row, the I-front is still sweeping the computational volume. The lower row shows post-reionization (in practice, we show the last simulation snapshot at $z_{now} \sim 5$). The 'Total' lines refer to all gas in the volume, whereas the 'Halo' lines refer only to gas in haloes. We also distinguish the contribution of gas in haloes according to halo mass (different line styles). Those labelled 'Ionized' correspond to $\Delta^3\mathcal{P}_V(\Delta)x_{HII}^2$ such that the area under the curve is proportional to the recombination rate per unit volume per decade in Δ. The left-shaded regions correspond to densities too low to resolve accurately, and the right-shaded regions indicate gas above our artificial 'star formation threshold' where the simulation is unreliable due to missing physics. The short dashed lines at the top left corners indicate the power law $\mathcal{P}_V \propto \Delta^\gamma$, for $\gamma = -2.5$ for comparison. This power law describes the scaling of Miralda-Escudé et al.'s (2000) model at high densities (see the main text). The low-mass mini-haloes are photoevaporated between the upper and lower panels.

Before reionization, the gas temperature remains below $\sim 10^4$ K due to Compton and atomic line cooling. Hence, pre-reionization gas exists in the triangular-shaped region of the upper panel. But we note that by mass, most of the gas remains close to the entropy floor, as shown by the contours.

After the I-front has crossed the computational volume, gas with $\log\Delta \leq 2$ is ionized and photoheated to $T \sim 2.2 \times 10^4$ K. Gas at higher densities self-shields, remains mostly neutral, and is at $\log T \, [K] \sim 2$–4. The lower density gas with $\log\Delta \sim 0$–1 is mostly at $T \sim 2.2 \times 10^4$ K, but some gas is hotter, and some gas is cooler. This results in a diamond-shaped region in Fig. 7. As we explained previously, the origin of the hotter gas is due to adiabatic compression and shocking of underdense gas by filaments.[20] But clearly, some gas can also cool adiabatically, explaining the lower diamond region.

The connection with filaments is illustrated in more detail in Fig. 8, which shows a close-up of two filaments that are nearly parallel to the y-axis (plotted horizontally in this figure). The middle panel shows that both filaments are expanding in the x-direction with a speed $|v_x|$ of up to $20\,\mathrm{km\,s^{-1}}$ (which is higher than the sound speed). This adiabatic expansion cools the central region of the filament and heats the surroundings IHM through compression (upper panel). Similar

adiabatic changes are seen in the expansion of mini-haloes and the resulting compression in their surroundings, for example, test 7 in Iliev et al. (2009).

4.3 The inverse Strömgren layer

When an I-front overruns neutral gas in a halo, its denser interior may be able to stall the front, provided the recombination rate is high enough. In mini-haloes, the front will continue to move inwards as the gas in the outer parts photoevaporates, but in more massive haloes, the centre may continue to self-shield. In this section, we estimate the density, n_S, at the location of this 'ISL', above which gas self-shields and remains mostly neutral.[21] In the simulations, we determine n_S as the minimum gas density where $x > 1/2$. The value of n_S is of interest because it impacts the overall recombination rate and the clumping factor in a patch of Universe. A good understanding of what sets n_S might also help to model self-shielding in simulations without performing computationally expensive RT (e.g. Rahmati & Schaye 2014; Ploeckinger & Schaye 2020).

An analytical estimate for n_S can be derived from the model of Theuns (2021) for damped Lyman-α systems. Assume that the density profile in a halo of virial radius R_h is the power law

$$n_H(r) = n_{H,h} \left(\frac{R_h}{R}\right)^2, \tag{15}$$

[20]We tracked particles with $T > 9 \times 10^4$ K and $\log\Delta \sim 0$–1 back in time to investigate the evolution of their entropy. After being photoionized, their entropy changes slightly, whereas their density may change by one order of magnitude. This means that their temperature change is mostly due to adiabatic compression/expansion, with a small contribution from shock. This is consistent with the scatter in temperature being approximately symmetric around the $T \sim 2.2 \times 10^4$ K.

[21]Note that n_S is not the self-shielding density $n_{H,SSh}$, used in Rahmati et al. (2013). The latter describes the density where the *optical depth due to self-shielding* reaches $\tau = 1$, and x can be much less than $1/2$ even when $\tau = 1$.
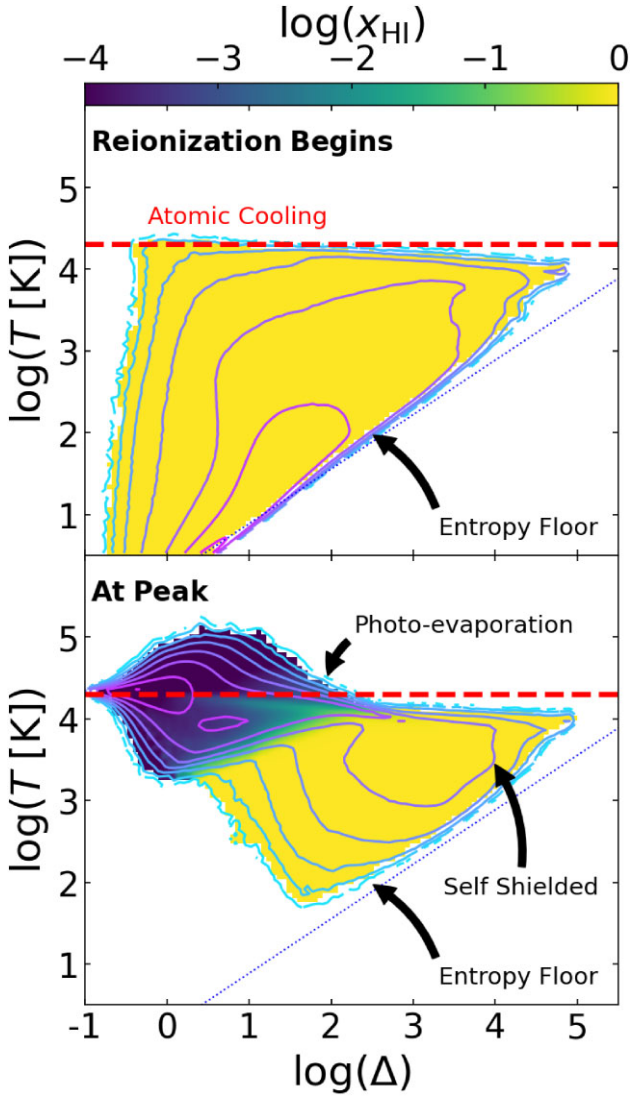
Figure 7. Temperature versus overdensity diagrams for the M512z8G03 run at the start of reionization, $z \lesssim z_i$ (upper panel) and when the clumping factor c_r is maximal (lower panel). The colour scale encodes the mass-weighted neutral fraction. The horizontal dashed line is the temperature where the cooling due to H I is maximum. The dotted line is the initial entropy (equation 13). Contours indicate the surface density of gas particles in this plot, evenly spaced in log surface density.

where $n_{\mathrm{H,h}} (= 200/3 \langle n_{\mathrm{H}} \rangle)$ is the hydrogen density at the virial radius. Assuming that the gas is in photoionization equilibrium, the rate of change of the neutral density is zero,

$$\frac{\mathrm{d}n_{\mathrm{HI}}}{\mathrm{d}t} = -\Gamma \, x \, n_{\mathrm{H}} + \alpha_{\mathrm{B}} (1-x)^2 \, n_{\mathrm{H}}^2 = 0 \,, \tag{16}$$

where x is the neutral fraction and we have neglected collisional ionizations and any contribution from helium or other elements. The photoionization rate Γ at radius R in the cloud is related to its value Γ_h at R_h by

$$\Gamma = \Gamma_h \exp(-\tau) \,, \tag{17}$$

where the optical depth

$$\tau = \int_R^{R_h} \sigma_{\mathrm{HI}} \, x \, n_{\mathrm{H}} \, \mathrm{d}R \,. \tag{18}$$
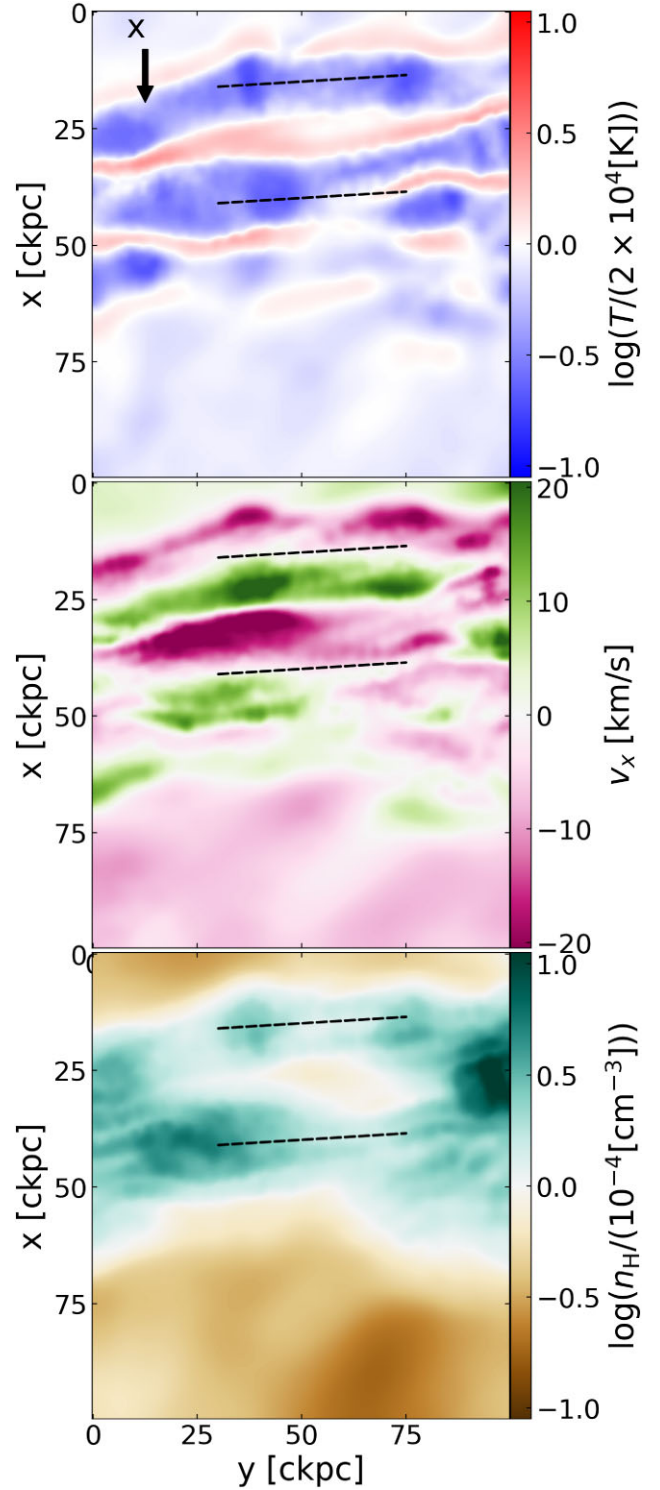
Figure 8. Slices through the M512z8G03 run at $z = 7.58$, after the I-front has crossed the simulation volume (see Fig. 5). Panels show temperature (upper panel), velocity in the x-direction (central panel), and hydrogen density (lower panel). These particular slices illustrate the photoevaporation of two filaments, indicated by dashed black lines in each panel. At this moment in time, the density in the filaments is higher than in their surroundings (lower panel), yet the gas is cooler due to adiabatic expansion. The gas expands at a speed close to the sound speed (central panel) and compresses and heats the gas in the surrounding IHM as seen in the upper panel. This type of compressional heating is the origin of the hotter gas, $T > 10^{4.2}$ K, seen in Fig. 7.

Combining these yields

$$\exp(-\tau) = \frac{\alpha_B\, n_{H,h}}{\Gamma_h} \frac{(1-x)^2}{x} \left(\frac{R_h}{R}\right)^2. \tag{19}$$

Taking the logarithm on both sides yields

$$-\tau = -\int_R^{R_h} \sigma_{HI}\, x\, n_H\, dR = \ln\left[\frac{\alpha_B\, n_{H,h}}{\Gamma_h} \frac{(1-x)^2}{x} \left(\frac{R_h}{R}\right)^2\right], \tag{20}$$

and taking the derivative with respect to R

$$\sigma_{HI}\, x\, n_{H,h} \left(\frac{R_h}{R}\right)^2 = -\frac{1}{x}\frac{dx}{dR} - \frac{2}{1-x}\frac{dx}{dR} - \frac{2}{R}. \tag{21}$$

This is a differential equation for $x(r)$, which we write in dimensionless form as

$$\left(-\frac{1}{x} - \frac{2}{1-x}\right)\frac{dx}{dr} = \frac{2}{r} + \tau_h \frac{x}{r^2}, \tag{22}$$

where $\tau_h \equiv \sigma_{HI}\, n_{H,h} R_h$ is a characteristic optical depth for the halo, and $r \equiv R/R_h$. The boundary condition is the neutral fraction $x = x_h$ at $r = 1$,

$$\frac{x_h}{(1-x_h)^2} \approx x_h = \frac{\alpha_B\, n_{H,h}}{\Gamma_h} = \frac{t_i}{t_r}, \tag{23}$$

where the ionization and recombination time at $r = 1$ are $t_h \equiv \Gamma_h^{-1}$ and $\equiv (\alpha_B n_{H,h})^{-1}$. This differential equation has no closed-form solution, the numerical solution is plotted in Fig. 9 for a range of halo masses and two redshifts. In the ionized outskirts of the halo, we can take $x \ll 1$ so that $1 - x \approx 1$, and the differential equation simplifies to

$$-\frac{1}{x}\frac{dx}{dr} = \frac{2}{r} + \tau_h \frac{x}{r^2}, \tag{24}$$

with solution

$$x(r) = \frac{3r x_h}{-\tau_h\, x_h + (3 + \tau_h\, x_h)r^3}. \tag{25}$$

This approximate solution is also plotted in Fig. 9. Not surprisingly, it captures the increase in x with increasing n_H very well when $x \ll 1$, but it also captures rather well the density and location where $x = 1/2$ and even where $x = 1$. At a given redshift, n_S (where $x = 1$) is higher for lower halo masses. For a given halo mass, n_S increases with increasing redshift.

We obtain the scaling of n_S with M_h and z as follows. We start by computing the value R_S of the ISL by expressing that the recombination rate along a ray, from R_h to R_S, equals the impinging flux – this simply means that all photons impinging on the halo at R_h have been used up by recombination between R_h and R_S:

$$\int_{R_S}^{R_h} \alpha_B\, n_H^2(r)\, dr = \frac{\Gamma_h}{\sigma_{HI}}, \tag{26}$$

so that for our $1/r^2$ density profile

$$r_S \equiv \frac{R_S}{R_h} = \left(1 + \frac{3\, t_r}{t_i\, \tau_h}\right)^{-1/3} \approx \left(\frac{3\, t_r}{t_i\, \tau_h}\right)^{-1/3}. \tag{27}$$

We note that t_r depends on redshift but not on halo mass, whereas τ_h depends both on M_h and redshift. The approximation of neglecting the '1' in the round brackets applies to most cases of interest. In this approximation, we derive the following scaling relation for the
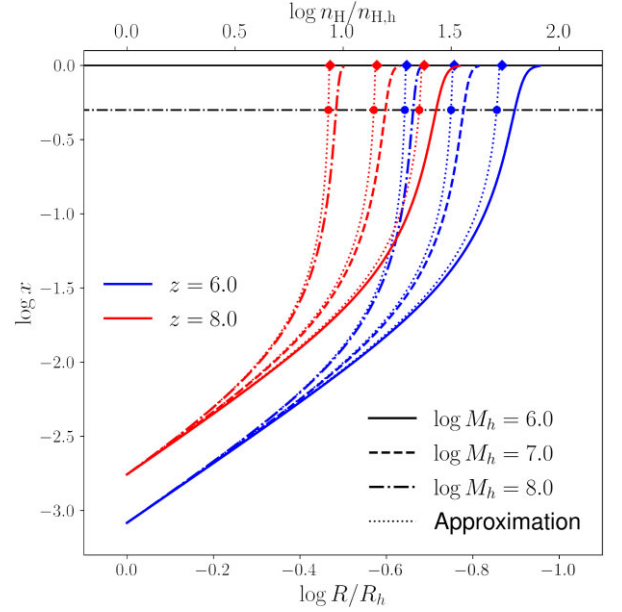
Figure 9. Neutral fraction as a function of radius (lower horizontal axis) or density (upper horizontal axis) in haloes with a spherical density profile of the form $n_H = n_{H,h}(R_h/R)^2$, where R_h is the virial radius, for different halo masses (different line styles) and redshifts (left set of lines: $z = 8.0$; right set of lines: $z = 6.0$) as per the legend, obtained by integrating equation (22). The horizontal dotted–dashed line and solid line indicates $x = 1/2$ and 1. The dotted line is the approximation for $x(R)$ from equation (25). Small dots and small diamonds indicate the value where $x = 1/2$ and 1 in the approximate model. The calculations take $\Gamma_h = 10^{-12}$s for the photoionization rate at the virial radius, $\alpha_r = \alpha_B(T = 10^4\,K)$ for the recombination rate, and $\sigma_{HI} = 1.62 \times 10^{-18}$cm^{-2} for the photoionization cross-section. The approximate model is fairly accurate, even in predicting the location and density where $x = 1/2$ and 1. The value of $n_{H,h} = 8.6 \times 10^{-3}$ and 4.1×10^{-3} cm^{-3} at $z = 8$ and 6, respectively.

hydrogen density n_S at the Strömgren radius,

$$n_S \approx \frac{1}{n_{H,h}^{1/3} R_h^{2/3}} \left(\frac{3\Gamma_h}{\alpha_B\, \sigma_{HI}}\right)^{2/3}$$

$$\sim 0.09\, \mathrm{cm}^{-3} \left(\frac{1+z}{8}\right)^{-1/3} \left(\frac{M_h}{5 \times 10^7\, M_\odot}\right)^{-2/9}$$

$$\times \left(\frac{\Gamma_h}{10^{-12}\mathrm{s}^{-1}}\right)^{2/3}. \tag{28}$$

with the numerical value taking the gas temperature to be $T = 10^4$ K when evaluating the recombination coefficient, and taking $\sigma_{HI} = 1.62 \times 10^{-18}$ cm^{-2}. We note that the dependencies on halo mass and redshift are relatively weak.

So far, we characterized the photoionization rate by its value Γ_h at the virial radius. It is likely that $\Gamma_h < \Gamma_0$, where Γ_0 is the volume-averaged photoionization rate because the gas in the surroundings of the halo also causes absorption and hence suppresses the ionizing flux. We can estimate the importance of this effect by simply extrapolating the $1/r^2$ density profile to infinity:

$$\int_{R_h}^{\infty} \alpha_B\, n_H^2\, dr = \frac{\Gamma_0 - \Gamma_h}{\sigma_{HI}}. \tag{29}$$
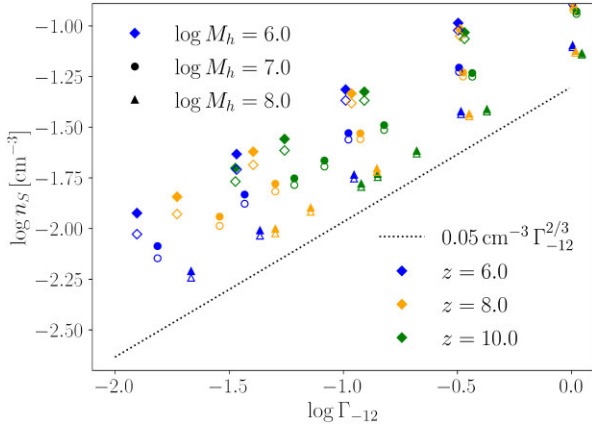
Figure 10. The transition to neutral gas in the model of Theuns (2021). Filled symbols denote the density at the inverse Strömgren radius, computed from equation (28). Open symbols denote the minimum density where $x >$ 1/2, obtained from integrating equation (22). In both cases, we used equation (30) to relate the photoionization rate at the virial radius, Γ_h, to its volume-averaged value, $\Gamma_0 \equiv 10^{-12}\Gamma_{-12}\,\text{s}^{-1}$. The symbol type encodes virial mass, M_h in units $M_\odot$, and its colour encodes redshift, as per the legends. The dotted line shows the scaling $\propto \Gamma_0^{2/3}$. We have evaluated the recombination coefficient at $T = 10^4$ K and set $\sigma_{HI} = 1.62 \times 10^{-18}\,\text{cm}^2$.

This yields the following relation,

$$\Gamma_h = \Gamma_0 - \frac{n_{H,h}\tau_h\alpha_r}{3} \equiv \Gamma_0 \left[1 - \exp(-\tau_\infty)\right]$$
$$\times \exp(-\tau_\infty) = \frac{n_{H,h}\tau_h\alpha_r}{3\Gamma_0}. \tag{30}$$

We plot n_S computed from equation (28) and use the previous equation to relate Γ_h to Γ_0 in Fig. 10.

The transition from neutral to ionized gas is relatively sharp in the simulations, as can be seen by comparing the 'Ionized' and 'Neutral' lines in Fig. 6. This justifies the Miralda-Escudé et al. (2000) assumption for a characteristic density dividing mostly neutral and mostly ionized gas, which was also shown in other numerical studies, for example, McQuinn et al. (2011), Park et al. (2016), and D'Aloisio et al. (2020). Therefore, the value of n_S is relatively well defined, and operationally we determine it for each halo as the minimum density for which $x > 1/2$. We plot this value in Fig. 11 as a function of Γ_{-12}. The analytical relation of equation (28) captures the $n_S \propto \Gamma_{-12}^{2/3}$ scaling, but the simulated value of n_S is smaller. We suspect this is due to the density structure in the accreting gas, which the analytical model does not account for.

We generalize the analytical calculation to the case of a halo overrun by a plane-parallel I-front in Appendix E. We use this to test the ability of the RT scheme to capture an I-front at the typical numerical resolution with which we simulate mini-haloes.

4.4 Photoevaporation of mini-haloes

Here, we examine the time-dependent effects of the ionizing radiation on individual haloes. To do so, we need to calculate how long mini-haloes have been irradiated with ionizing radiation.

In our simulations, we inject ionizing photons from two opposing sides of the periodic volume. As a consequence, mini-haloes close to the injection side are affected by the radiation earlier (and for longer) than those further away. To account for this time difference, we first calculate the I-front position, defined as the location where the volume-weighted neutral fraction is ~0.5 (we do this in cubic cells
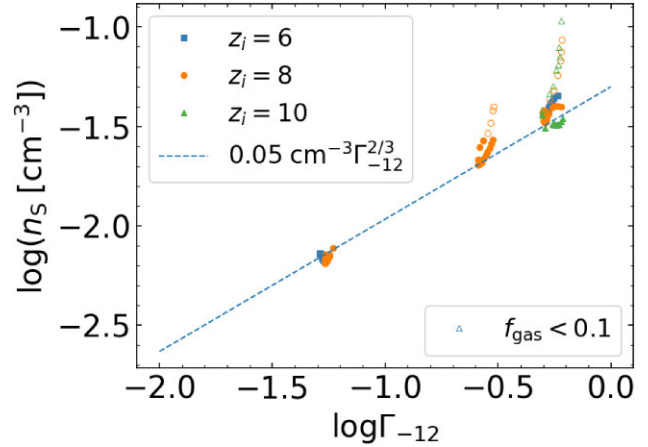
Figure 11. Hydrogen density, n_S, where gas transitions to neutral, $x > 1/2$, in the simulations plotted against the volume-averaged photoionization rate, Γ_{-12}, after the I-front has crossed the simulation volume. Large markers refer to gas in haloes that contain more than 10 per cent of the cosmic baryon fraction, f_b; small markers are for haloes containing less than 10 per cent of f_b. Different markers encode different values of z_i, as per the legend. The dashed line indicates the theoretical scaling ($n_S \propto \Gamma_{-12}^{2/3}$; equation 28).

of extent 10 ckpc instead of considering a plane-parallel I-front). For each halo, we then record the time since it encountered the I-front. Hence, we can compute the duration t_{dur} between the current time and the time that the halo was first irradiated.

We select ~20 mini-haloes with mass $M_h \sim 10^6\,M_\odot$ and compute the median of their spherically averaged radial density profiles. We assume that the centre of the halo corresponds to the location where the density of neutral gas is highest.[22]

The density profiles of these haloes are plotted in Fig. 12 for various values of t_{dur}, and two values of the photoionization rate, $\Gamma_{-12} = 0.3$ and 0.03.

If radiative cooling is inefficient (as in mini-haloes), the maximum gas density is limited by the entropy of the intergalactic medium (IGM) after decoupling from radiation (Visbal, Haiman & Bryan 2014). Therefore, the central density profiles are flat. Outside of the central regions, the profiles of the total density (solid lines) are reasonably well approximated by $n_H(r) \propto r^{-2}$ (black dotted–dashed line), at least before the I-front has propagated significantly into the halo's gas.

Using the order-of-magnitude estimates derived in Section 2.2.2, we find for the sound crossing time $t_{sc} \approx 20$ Myr, the I-front crossing time $t_{ic} = 4\,\Gamma_{-12}^{-1}$ Myr ≈ 13 Myr for $\Gamma_{-12} = 0.3$ (and 130 Myr for $\Gamma_{-12} = 0.03$), and the recombination time $t_r = 10$ Myr.

Therefore, haloes are in the sound-speed limited regime for $\Gamma_{-12} = 0.3$ (upper panel, using the nomenclature of Section 2.2.2). The I-front propagates rapidly into haloes, reaching down to 5 per cent of the virial radius within 50 Myr. Gas starts photoevaporating, but the time it takes to leave the halo is longer than t_{ic}. Therefore, the halo contains a large amount of highly ionized photoheated gas. Given that the gas has density profile is $n_H \propto r^{-2}$, the neutral gas has a density profile approximately $n_{HI}(r) = x\,n_H(r) \approx \alpha_B/\Gamma_{-12}n_H^2 \propto r^{-4}$.

In contrast, haloes are in the ionization limited regime when $\Gamma_{-12} = 0.03$ (lower panel). The I-front propagates so slowly into the cloud that the photoheated gas has time to photoevaporate and

---

[22]Taking a slightly different centre will affect the density profile mostly close to that centre.
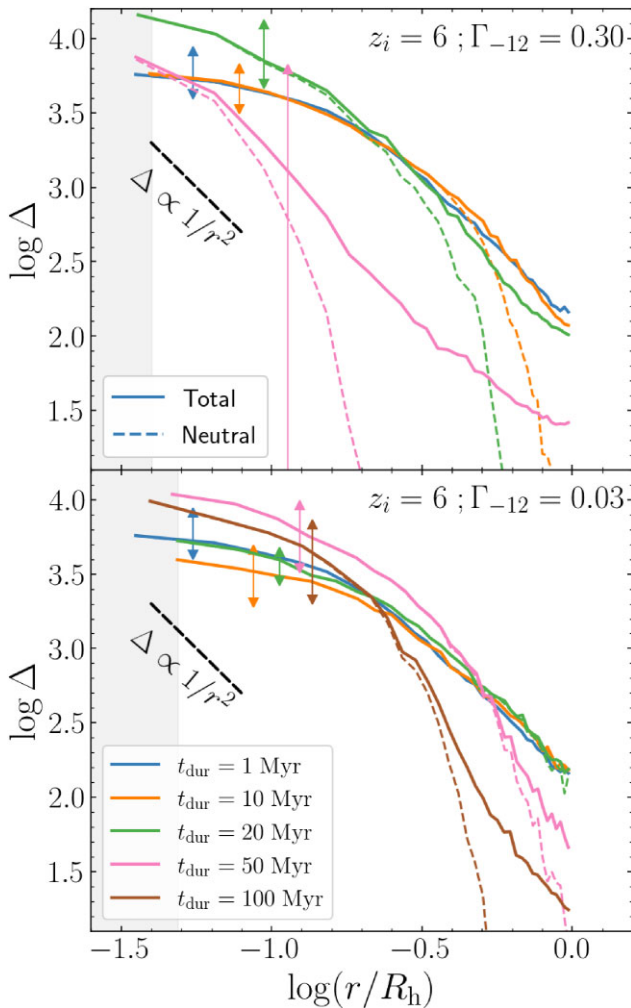
Figure 12. Gas overdensity profiles of haloes with $M_{\mathrm{h}} \sim 10^6$ M$_\odot$ at different times, t_{dur}, after they were over-run by an I-front. The solid lines are total gas density, whereas the dashed lines are neutral gas density. The arrows indicate the 15th and 85th percentiles of haloes with similar values of t_{dur}. The black dashed lines show power laws for isothermal profiles, $\rho(\Delta) \propto \Delta^{-2}$, that describe the run of the total density with radius in the range $0.1 \leq r/R_h \leq 1$ relatively well (R_h is the virial radius of the haloes). Gas in the shaded region is within a gravitational softening length from the centre.

leave the halo. Consequently, the neutral and ionized gas profiles almost trace each other. For this low value of Γ_{-12}, even haloes of this low mass can hold on to a large fraction of their gas for several 100 Myr, and this affects the duration of the photoevaporation phase of the EOR.

We demonstrate how fast a halo photoevaporates in Fig. 13. We plot the halo baryon fraction in units of the cosmic mean, $M_{\mathrm{gas}}/(f_b\, M_h)$ (where $f_b \equiv \Omega_b/\Omega_m$), at various values of t_{dur}. More massive haloes can hold onto their gas for longer times. An $M_h = 10^5$ M$_\odot$ halo loses half of its gas in $t_{\mathrm{dur}} = 20$ Myr for $\Gamma_{-12} = 0.3$. On the other hand, a halo with $M_h = 10^7$ M$_\odot$ has only lost ≈ 20 per cent of its gas at $t_{\mathrm{dur}} = 50$ Myr at $\Gamma_{-12} = 0.3$. A lower Γ_{-12} can also slow down the photoevaporation, for example, the $M_h = 10^5$ M$_\odot$ halo takes twice as long to photoevaporate at $\Gamma_{-12} = 0.03$ (than $\Gamma_{-12} = 0.3$).

A more quantitative measure of the photoevaporation time-scale is plotted in Fig. 14. We have computed the value of t_{dur} after which a halo contains only 10 per cent of the cosmic baryon fraction, which we refer to as $t_{\mathrm{ev,10\,per\,cent}}$ (upper panel). For $\Gamma_{-12} = 0.3$, we
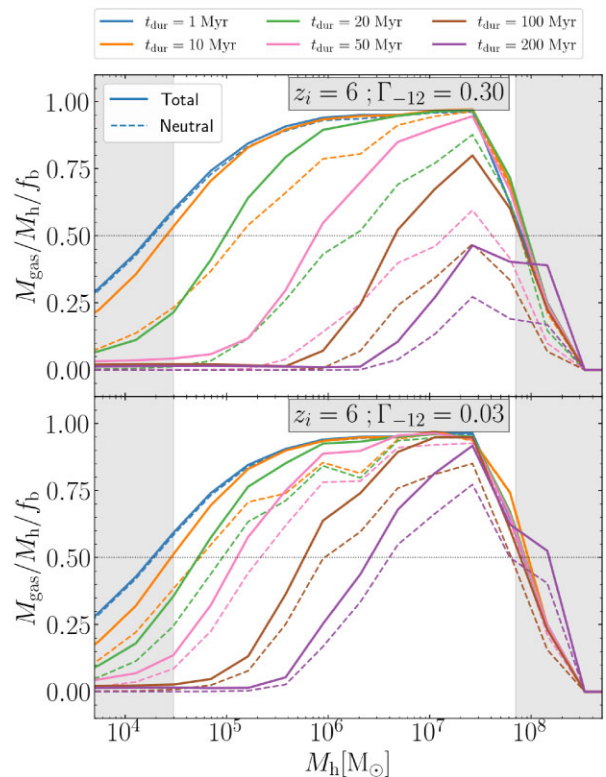

Figure 13. Ratio between gas mass within the virial radius and the halo mass, in units of the cosmic baryon fraction, f_b. Solid lines refer to total gas mass, and dashed lines to neutral gas. Different colours correspond to different times, t_{dur}, since the halo was over-run by I-front, from blue (recently) to purple (long ago). The upper panel has $\Gamma_{-12} = 0.3$, whereas the lower panel has the lower photoionization rate of $\Gamma_{-12} = 0.03$. Haloes in the left-shaded regions are resolved with fewer than 300 dark matter particles. Haloes in the right-shaded *region* are susceptible to atomic cooling.

find the approximate scaling $t_{\mathrm{ev,10\,per\,cent}} \propto M_h^{1/2.3}$ (solid lines in the top right panel), which is somewhat shallower than the $t_{\mathrm{ic}} \propto M_h^{1/3}$ dependence of the I-front crossing time on halo mass. That panel also shows that the evaporation time depends surprisingly little on redshift. The dependence is even weaker than that of the sound crossing time, $t_{\mathrm{sc}} \propto (1 + z)^{-1}$. $t_{\mathrm{ev,10\,per\,cent}}$ can be a few times t_{sc}, because recombinations significantly delay ionization and hence photoevaporation.

In the left and central panels, we notice that the dependence of $t_{\mathrm{ev,10\,per\,cent}}$ on Γ_{-12} is weaker than that of $t_{\mathrm{ic}} \propto \Gamma_{-12}^{-1}$. At the lower values of $\Gamma_{-12} = 0.03$, the more massive haloes have not yet reached $t_{\mathrm{ev,10\,per\,cent}}$ by the end of the simulation run: this is indicated by the thin dotted lines.

The dashed lines indicate when the haloes contain less than 10 per cent of neutral gas. When Γ_{-12} is low (e.g. $\Gamma_{-12} = 0.03$), there is little difference between the total and neutral gas lines because once ionized, gas quickly leaves the halo: these haloes are in the ionization-limited regime. However if Γ_{-12} is larger ($\Gamma_{-12} = 0.3$, say), some of the ionized gas is still inside the halo because it has not had time yet to photoevaporate: these haloes are in the sound-speed limited regime. The difference between the two regimes is more pronounced at lower z and lower halo mass, as seen in the central panel.

The lower panel of Fig. 14 shows $t_{\mathrm{ev,0.1\,per\,cent}}$, the time after which haloes contain less than 0.1 per cent of the cosmic baryon fraction. The panels compare our results to those of Iliev et
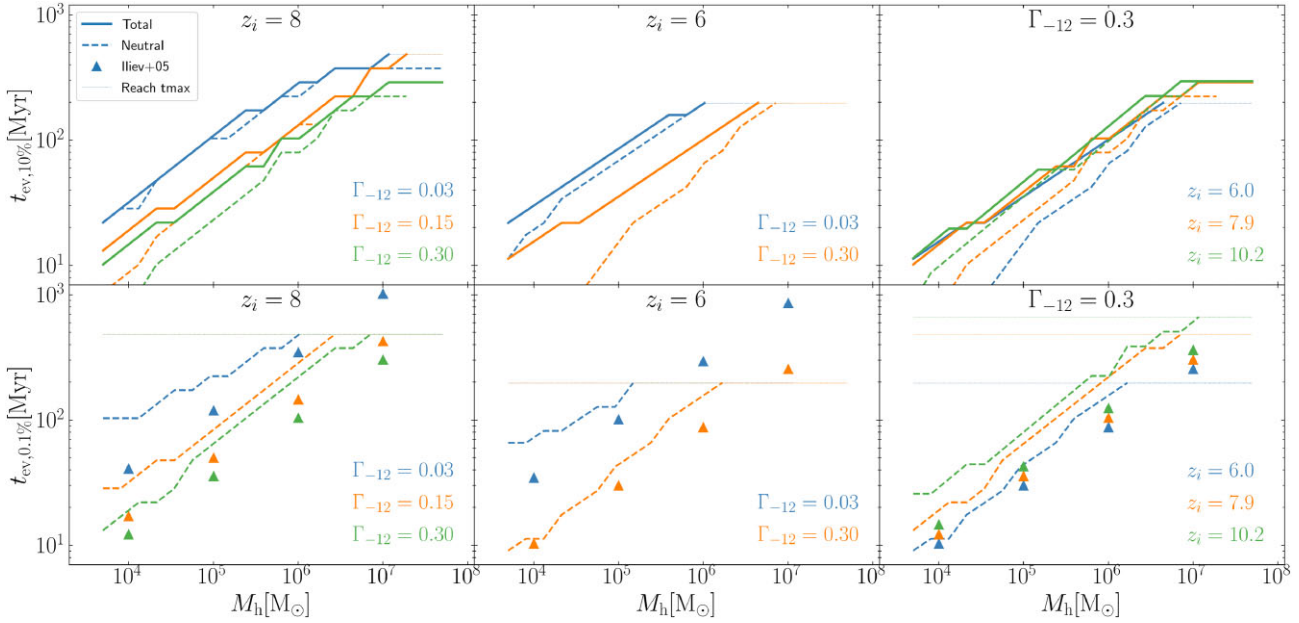
Figure 14. Evaporation time, t_{ev}, as a function of halo mass, M_h. The upper panels show the time to lose 90 per cent of the total gas mass (solid lines) or the neutral gas mass (dashed lines) (relative to the cosmic share of baryons; after the halo was over-run by I-front). Thin dotted lines indicate that evaporation is not yet complete when the simulation is stopped. The lower panels are similar, except that haloes must lose 99.9 per cent of their gas. Triangles are the simulation results of Iliev et al. (2005a). Our evaporation times are slightly longer, but the trends with M_h and Γ_{-12} are very similar: the evaporation time increases with M_h and z_i, and decreases with increasing Γ_{-12}.

al. (2005a, triangles), and we find an agreement within a factor of two. Several differences between our simulations and theirs may explain the difference. First, ours are 3D cosmological RHD simulations, in which haloes grow in mass through mergers and accretion during photoevaporation. In contrast, theirs are 2D non-cosmological simulations. Secondly, our simulations include the effect of shadowing since we simulate a cosmological volume. Third, we consider radiation in one frequency bin, whereas their RT is multifrequency. The multifrequency treatment will allow high-energy radiation to penetrate further into haloes and include effects of spectral hardening (which boost the photoevaporation rates). Finally, our SPH simulation is particle-based, whereas they used a uniform grid. Our spatial resolution is comparable to theirs at high density, but is lower in lower density regions.

We do not plot the evaporation times of the total gas (solid) in the lower panels. It is because, in our simulations, the total gas fraction does not drop below 0.1 per cent: even mini-haloes with $M_h \sim 10^4 \, M_\odot$ can hold on to a small fraction of (highly ionized) gas.

4.5 The impact of small-scale structure on reionization

4.5.1 The clumping factor, c_r

The recombination rate in an inhomogeneous medium is enhanced compared with that of a uniform medium of the same mean density by the clumping factor, c_r.[23], which we define here as

$$\left\langle \left. \frac{dn_{HI}}{dt} \right|_{rec} \right\rangle = \langle \alpha_B \, n_e \, n_{HII} \rangle \equiv c_{r,all} \, \alpha_B(\bar{T}) \, \langle n_{HII} \rangle^2 , \quad (31)$$

---

[23]Note that c_l as defined in the Introduction does not account for recombination rate but c_r does.

with the extra subscript 'all' added for reasons explained below. Here, angular brackets, $\langle \rangle$, denote volume-averaging and $\bar{T}$ is the mass-averaged temperature. This definition captures the dependence of the recombination rate on temperature (see also Park et al. 2016). Other definitions have appeared in the literature: these clumping factors can differ by tens of per cent, but the qualitative trends are similar (see Appendix D for details).

Structures change the I-front speed and location; inserting equation (31) into equation (5) yields the solution

$$Z = \frac{\tau_r \, F}{c_r \, n_H} \left[1 - \exp(-c_r t/\tau_r) \right] ,$$
$$\frac{dZ}{dt} = \frac{F}{n_H} \exp(-c_r t/t_r) , \quad (32)$$

in the approximation that n_H, t_r, and F are all time independent. As expected, the I-front moves slower and stalls earlier when clumping is more pronounced (greater c_r).

We cannot apply equation (31) directly to our simulations because (i) we inject radiation from the sides into the computational volume, and (ii) we include collisional ionization in the calculation. To account for (i), we only include gas downstream from the I-front in the calculation of c_r:

$$c_r = \frac{\langle \alpha_B \, n_{HII}^2 \rangle_{IF}}{\alpha_B(\bar{T}_{IF}) \, \langle n_{HII} \rangle_{IF}^2} . \quad (33)$$

We approximate the I-front by a plane where the volume-weighted neutral fraction first reaches 50 per cent (and perpendicular to the injection direction). We also resolve (ii) this way since collisional ionization contributes relatively little to the recombination rate in the downstream region, where photoionization dominates. Furthermore, our small simulation volume does not contain many more massive haloes where collisional ionizations are frequent.
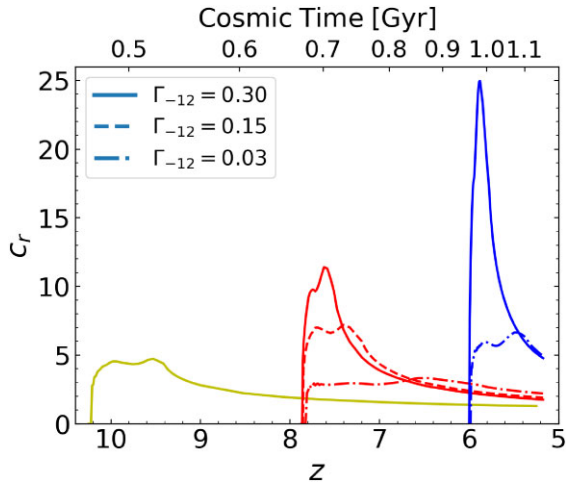
Figure 15. Clumping factor, c_r (equation 33), as a function of redshift, z, for simulations with different photoionization rates Γ_{-12} (solid, dashed, dotted–dashed lines correspond to $\Gamma_{-12} = 0.3, 0.15$, and 0.03). The line colour indicates different redshifts of ionization (left, middle, and right sets of lines correspond to $z_i \sim 10, 8$, and 6 respectively). When the I-front enters the simulation volume, c_r rapidly increases to a peak value, $c_{r,\text{peak}}$. Then, c_r decreases on a time-scale of order 100 Myr before reaching asymptotically an approximately constant value. The value of $c_{r,\text{peak}}$ increases with increasing Γ_{-12} and decreasing z_i, but the asymptotic late-time value of c_r is approximately independent of Γ_{-12}.

4.5.2 Evolution of the clumping factor

Fig. 15 shows the evolution of the clumping factor as computed using equation (33). In all runs, c_r increases rapidly to a peak value,[24] and after ~ 100 Myr, starts to decrease to an asymptotic value of $\lesssim 5$. The height of the peak, $c_{r,\text{peak}}$, increases with increasing Γ_{-12} and with decreasing z_i. We find that approximately

$$c_{r,\text{peak}} \sim 9 \times \left(\frac{1+z_i}{9}\right)^{-3} \left(\frac{\Gamma_{-12}}{0.3}\right)^{\gamma}, \qquad (34)$$

where the exponent $\gamma \sim 0.5$–0.6. The increase in $c_{r,\text{peak}}$ with decreasing z_i is simply due to structure formation: there are far fewer haloes at higher z to boost the recombination rate. The dependence on Γ_{-12} is a result of the increase of n_S (the density where the recombination rate is sufficiently high that the gas remains significantly neutral, equation 27) with Γ_{-12} and the dependence of the photoevaporation time-scale on Γ_{-12}.

We caution the reader that our small simulation volume does not contain sufficient massive haloes that dominate c_r post-reionization. This may affect the simulation with $z_i \sim 10$ most because photoheating of the IHM at high z prevents haloes from accreting gas.

The contribution to the recombination rate of gas at different densities is plotted as the blue line, labelled as 'Total' in Fig. 16. At low reionization redshift z_i, high Γ_{-12}, and close to the reionization redshift ($z \sim z_i$), the recombination rate is dominated by the denser gas with $\Delta > 100$ that is mostly inside of haloes (upper left panel). At slightly later times (lower left panel), lower density gas with Δ of the order of a few starts to dominate because the denser gas has photoevaporated (in fact, a considerable fraction of the gas with initial overdensity $\Delta \sim 100$ decreases in density to values of a few following its photoevaporation, see the discussion of Fig. F1).

Our small simulation volume underestimates the contribution of haloes to recombinations to some extent. Still, we find that similar trends (a rapid rise in c_r to a peak value, followed by a decrease on a longer time-scale) in a simulation performed in a larger computational volume (see Appendix D).

The central panels in Fig. 16 also demonstrate how photoevaporation decreases the contribution of halo gas to the recombination rate. Due to photoevaporation, gas around the mean density, $\Delta \sim 1$, increasingly dominates the recombination rate at later times. This is even more striking in the right panels of the figure: early reionization prevents the accretion of gas onto more massive haloes that form after z_i so that haloes now contribute much less to recombinations.

The other coloured lines in Fig. 16 quantify the contribution to the recombination rate in haloes of a given mass range, as indicated by the legend. For our choice of photoionization rate, Γ_{-12}, and reionization redshift, z_i, we find that mini-haloes with mass below $10^6\, M_\odot$ (grey dashed line) do not contribute significantly to the recombination rate, and by extension to the clumping factor. This is partly because they photoevaporate quickly, as seen by comparing the upper panel with the lower panel in any given column. Rather, the more massive mini-haloes with masses $\gtrsim 10^{6-7}\, M_\odot$ dominate recombinations during the EOR.

Our findings agree with those of Iliev et al. (2005a), who also concluded that mini-haloes with $M_h \ll 10^6\, M_\odot$ contribute little to c_r. They find that haloes with mass less than $\sim 10^6\, M_\odot$ increase[25] the photon consumption during EOR by less than a 10 per cent–20 per cent. Since low-mass mini-haloes do not affect c_r significantly, we could relax the required resolution of our simulations to $m_{\text{DM}} \lesssim 10^3\, M_\odot$ (see Appendix D).

We now return to the late-time behaviour of the clumping factor, as plotted in Fig. 15. The value of c_r drops from its peak to an asymptotic value of ~ 2–3 after several 100 Myr, in agreement with previous simulations of the post-EOR IHM (e.g. Pawlik et al. 2009; McQuinn et al. 2011). The duration of the characteristic drop is set by the photoevaporation time of mini-haloes, which is of the order of 100 Myr for the more massive mini-haloes and $\lesssim 50$ Myr for mini-haloes with mass $M_h = 10^5\, M_\odot$ (see Fig. 14).

Interestingly, we find that the value of the clumping factor at the end of the EOR is relatively insensitive to the photoionization rate. For example, in Fig. 15, changing Γ_{-12} by over an order of magnitude does not affect the late-time clumping factors by more than $\gtrsim 10$ per cents. This was also seen in the simulations of D'Aloisio et al. (2020). This finding appears unexpected at first: larger values of Γ_{-12} cause the ionized-neutral transition to occur at higher densities (equation 27) and this increases the recombination rate. Therefore, if gas in haloes were to dominate the recombination rate (and hence c_r), then we would expect that $c_r \propto \Gamma^{1/3}$ (e.g. McQuinn et al. 2011). However, we find that recombinations mostly occur in gas with density around the mean at these early times, as seen in the lower panels of Fig. 16. Since this gas is highly ionized in any case, changing the value of Γ_{-12} has little effect on c_r.

We now compare our results to those obtained by D'Aloisio et al. (2020) and Park et al. (2016). Note that the evolution of the clumpy factor depends strongly on the simulation setup and the reduced speed of light, so we only make qualitative comparisons here. Our values of c_r are apparently ~ 50 per cent higher than those plotted in fig. 7 of D'Aloisio et al. (2020), when comparing the runs with $z_i = 8$ and 6, and $\Gamma_{-12} = 0.3$. However, D'Aloisio et al. (2020) used the

---

[24]There are two peaks in clumping factors. The second peak is due to the overlapping of I-fronts from opposite side.

[25]More precisely, they consider halo mass $< 100\, M_J$, where M_J is the pre-reionization Jeans mass.
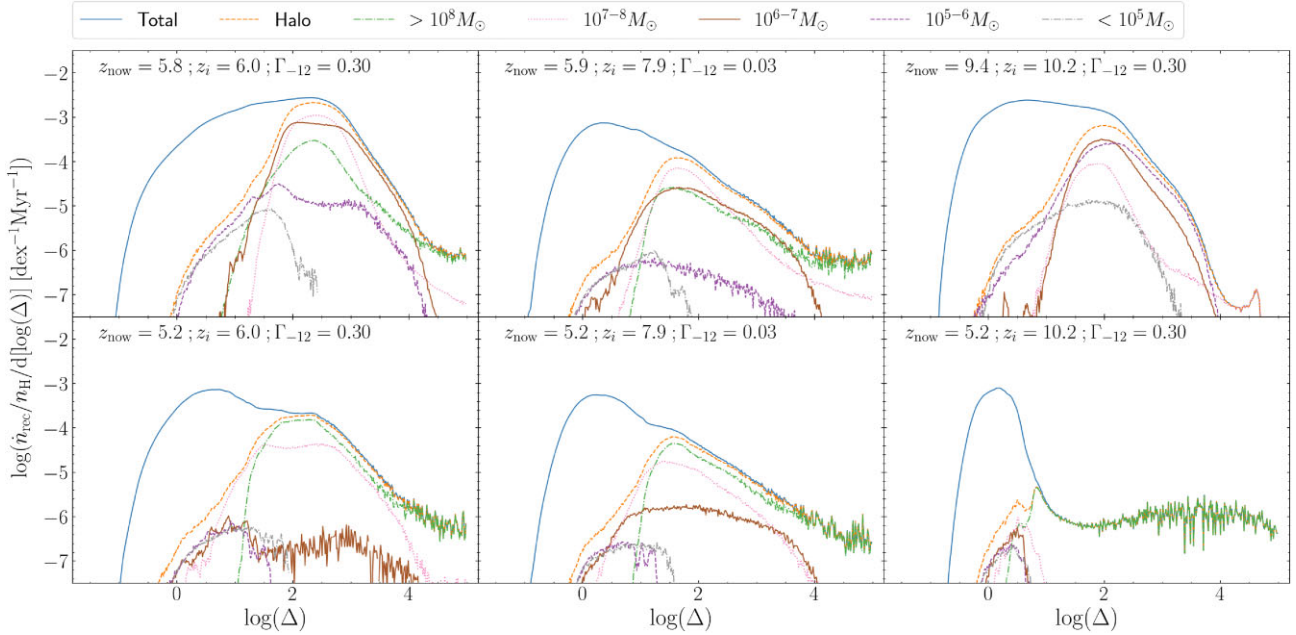
Figure 16. Total recombination rate per hydrogen, $\dot{n}_{\rm rec}/n_{\rm H}$, as a function of gas overdensity Δ, per decade in Δ. The area under the curve measures the contribution of gas at that overdensity to the recombination rate in the simulation volume. Line styles are the same as in Fig. 6. In a given column of panels, the upper row corresponds to $z \lesssim z_i$, whereas the lower row corresponds to a lower redshift. Gas in haloes contributes significantly to recombinations when $z \lesssim z_i$ and Γ_{-12} is high. As mini-haloes photoevaporate, the contribution of the IHM to the overall recombination rate increases. At even lower redshifts (not shown), recombinations in more massive haloes not contained in our small simulation volume dominate eventually.

clumping factor definition of equation (D3), which is tens of per cent lower than our fiducial definition equation (33) (because equation D3 used a lower reference temperature for recombination rate; see Appendix D). Thus, our results are roughly consistent.

Our simulations are not directly comparable to those of Park et al. (2016), since we used $\Gamma_{-12} = 0.3$, roughly a factor of 3 lower than that used by them, $\Gamma_{-12} = 0.92$. Applying the scaling of equation (34) with $\gamma = 0.5$, we would expect $c_{r,{\rm peak}} \approx 4.7 \times (0.92/0.3)^{1/2} \approx 8.2$ for the case of $z_i = 10$ and $\Gamma_{-12} = 0.92$, which is reasonably close to their value of $c_{r,{\rm peak}} = 7.5$ for that value of Γ_{-12} and z_i in their run M_I-1_z10. We also agree that the suppression of c_r due to photoevaporation is more significant at lower Γ_{-12} because the gas in mini-haloes starts to photoevaporate before radiation ionizes the higher density gas.

4.5.3 Photon consumption in the clumpy medium

In Fig. 17, we plot the ratio $\mathcal{N}_r \equiv N_{\rm rec}/N_{\rm H}$, where $N_{\rm rec}$ is the cumulative number of recombination in the simulation volume up to a given time, and $N_{\rm H}$ is the total number of hydrogen atoms in that volume. We computed and recorded this ratio as the simulation progressed. We find that $\mathcal{N}_r$ increases with Γ_{-12} (different line styles) but is rather strikingly only weakly dependent on z_i (different colours).

Since $c_{r,{\rm peak}} \propto \Gamma_{-12}^\gamma$, a higher photoionization rate increases the clumping factor and hence also $\mathcal{N}_r$, as expected. The weak dependence of $\mathcal{N}_r$ on z_i was also noted by Park et al. (2016). The mean instantaneous recombination rate per hydrogen atom is

$$\frac{\int \frac{{\rm d}n_{\rm HI}}{{\rm d}t}\big|_{\rm rec}\,{\rm d}V}{\int n_{\rm H}\,{\rm d}V} = \frac{c_r\,\alpha_B(\bar{T})\,\langle n_{\rm H}\rangle^2}{\langle n_{\rm H}\rangle} = c_r\,\alpha_B(\bar{T})\,\langle n_{\rm H}\rangle, \tag{35}$$
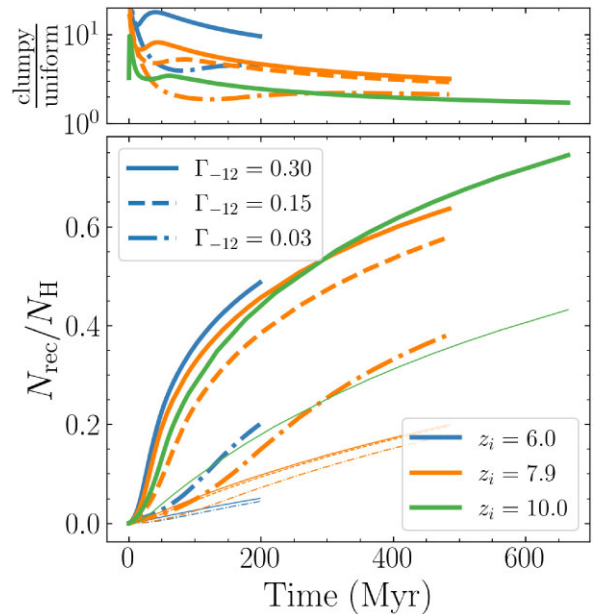
Figure 17. Lower panel: the cumulative number of recombinations per hydrogen atom, $N_{\rm rec}/N_{\rm H}$, as a function of time since ionizing photons were injected in the simulation volume. The thick lines represent the simulation results. The thin lines are computed for a homogeneous medium with the same median temperature. The ratio of these is plotted in the upper panel. Line colours and styles are as in Fig. 15. Although the clumping factor can be quite high, $c_r = 5$–20 (upper panel and Fig. 15), recombinations increase the required number of ionizing photons per hydrogen to complete reionization by a much smaller fraction, 1.2–1.7, because mini-haloes photoevaporate quickly. This fraction increases with Γ_{-12} (different line styles) but is only weakly dependent on z_i (different colours).

where the integral is over the computational volume. Since we found that approximately $c_r \propto (1 + z)^{-3}$ (equation 34), whereas $\langle n_H \rangle \propto (1 + z)^3$, the redshift dependence of the mean recombination rate per hydrogen atom is weak, which may explain the surprisingly weak dependence of $\mathcal{N}_r$ on z_i

Finally, we conclude that recombinations in the IHM and mini-haloes increase the number of ionizing photons per hydrogen atom required to ionize the Universe by a factor $1 + \mathcal{N}_r \approx 1.2 - 1.7$. The lower value corresponds to $\Gamma_{-12} = 0.03$, the upper value to $\Gamma_{-12} = 0.3$. Hence, the claim that recombinations increase $1 + \mathcal{N}_r$ by 20 per cent–100 per cent, which we made in the abstract.

5 DISCUSSION

Our simulation setup does not account for the formation of molecular hydrogen (H_2) and hence neglects cooling due to H_2. The simulations of Shapiro et al. (2004), Emberson et al. (2013), Park et al. (2016), and D'Aloisio et al. (2020) made the same assumption. Molecular hydrogen cooling can trigger star formation in haloes of masses as low as $10^6 \, M_\odot$ at $z \sim 10$ (e.g. Tegmark et al. 1997), orders of magnitude below the mass of haloes in which gas can cool atomically (M_{ACH} discussed in Section 2). Feedback from the first Pop III stars may remove gas from some mini-haloes, thus reducing their impact on the propagation of the I-front and the value of c_r. However, molecular hydrogen can be photodissociated by Lyman–Werner (LW) photons (Stecher & Williams 1967), which are emitted by those first stars (Haiman, Rees & Loeb 1997). An LW radiation background may thus have already turned off the molecular cooling channel at the redshifts we considered ($z \lesssim 10$, e.g. Trenti & Stiavelli 2009), suppressing Pop III star formation and hence reducing its impact on mini-haloes.[26]

We treat ionizing radiation using a frequency-averaged photoionization cross-section rather than following photons with a range of frequencies. This approximation does not capture the effects of spectral hardening or preheating. If included, these effects would most probably decrease the photoevaporation time of mini-haloes; hence, it may well be that our simulations overestimate the impact of such haloes on the EOR. For example, Iliev et al. (2005a) found that a harder spectrum can reduce the photoevaporation time by ~ 50 per cent.

We neglected sources of ionizing photons inside the computational volume. Instead, we injected photons from two opposing faces of the cubic simulation volume. Previous studies also inject radiation from boundaries and neglect the sources inside the volume (Emberson et al. 2013; Park et al. 2016; D'Aloisio et al. 2020). This approximation is reasonable for our purposes, given the small size of the computational volume.

Our simulation volume contains haloes with mass greater than M_{ACH} that would plausibly be able to form stars and contribute to the ionizing flux. Counter-intuitively, including stellar feedback from evolving stars forming in these haloes could potentially increase the net recombination rate. Indeed, McQuinn et al. (2011) found that the recombination rate is higher in a model that included stellar winds compared to a pure RHD run. Feedback can also avoid the overcooling problem, where too much gas turns into stars (Katz

---

[26]The escape fraction of LW photons from the star-forming gas cloud and the impact of self-shielding in the LW band are both uncertain (Skinner & Wise 2020). Therefore, the impact of Pop III stars on mini-haloes during the EOR is unlikely to play a significant role, although we realize this is not currently well constrained.

1992). Simulations with radiation sources within the simulation volume would be an important future improvement. These would be necessary for simulations of larger cosmological volumes where spatial correlations between photon sources and sinks are important.

Our simulations do not include pre-heating by X-rays emitted from an early generation of accreting black holes, as envisioned by Ricotti & Ostriker (e.g. 2004). Pre-heating would increase the minimum mass of haloes that contain gas before reionization, reducing the impact of mini-haloes on the EOR. D'Aloisio et al. (2020) presented a simulation where the IHM is pre-heated by X-rays below redshift $z = 20$, and found a factor of two suppression of $c_{r, \, peak}$ for a simulation with $z_i = 8$. They also concluded that X-ray pre-heating did not affect the value of c_r at the end of the EOR. Park et al. (2021) also studied the impact of X-ray preheating (starting at $z = 20$) and found a much larger decrease in the value of $c_{r, \, peak}$. However, their small simulation volume (200 h^{-1} ckpc) does not sample the more massive mini-haloes that may be less affected by X-ray pre-heating, which may lead them to overestimate the impact of pre-heating. Fialkov, Barkana & Visbal (2014) suggested that X-ray pre-heating most likely occurs at lower redshifts, not long before z_i, which would reduce its impact on mini-haloes.

We have neglected the relative velocity between dark matter and baryons post recombination (dark matter–baryon streaming), as discussed by Tseliakhovich & Hirata (2010). The streaming velocity can be several times larger than the pre-reionization sound speed, and this effect suppresses the early formation of low-mass haloes and affects their baryon contents. Studying this effect, Park et al. (2021) found a c_r lower by a factor of two. In contrast, Cain et al. (2020) concluded that baryon streaming decreases c_r by only 5 per cent–10 per cent (in regions with the root-mean-square streaming velocity). They claimed that the small simulation volume used by Park et al. (2021) exaggerates the streaming effects.[27]

In summary, the previous discussion highlights some of the various ways in which our simulations could be improved in the future. Nonetheless, these are unlikely to change our main conclusions substantially.

6 CONCLUSIONS

We presented cosmological RHD simulations of the propagation of I-fronts in a cosmological density field. RT is performed with a two-moment method with local Eddington tensor closure, implemented in the SWIFT SPH code, as described by Chan et al. (2021). Our simulations follow the ionization and heating of the gas, leading to the photoevaporation of (gas in) low-mass haloes (mini-haloes; $T_{vir} < 10^4$ K; $M_h \lesssim 10^8 \, M_\odot$), and self-shielding of gas in more massive haloes. The simulation can resolve the smallest mini-haloes that contain gas before reionization (gas mass resolution $m_{gas} \sim 20 \, M_\odot$; spatial resolution ~ 0.1 ckpc). We inject ionizing photons from two opposing sides of the computational volume at a given photoionization rate, Γ_{-12}, and for a given specified 'reionization redshift', z_i. We assume that the ionizing sources have a blackbody spectrum with temperature $T_{BB} = 10^5$ K.

These simulations improve upon the 2D RHD simulations performed by Shapiro et al. (2004) and Iliev et al. (2005a), who studied a more idealized set-up of a single mini-halo overrun by an I-front assuming cylindrical symmetry (see also Nakatani, Fialkov & Yoshida 2020). In contrast to previous cosmological RHD

---

[27]However, some of the difference between their results might be due to resolution (Cain et al. 2020).

simulations of the IGM (Park et al. 2016; D'Aloisio et al. 2020), we have either a larger volume or higher (spatial) resolution. We also quantify the relative contribution to the clumping and recombination of mini-haloes and the IHM. The results are presented in Section 4 and summarized in Section 6.

Our main results are as follows. In terms of the impact of the passage of the I-front on the cosmological density distribution, we find that

(i) Upon the passage of I-front, the low-density IHM is rapidly heated to $T \sim 2 \times 10^4$ K. This value is expected when a blackbody spectrum of photons with temperature $T_{BB} = 10^5$ K flash ionizes hydrogen when non-equilibrium effects are accounted for (Chan et al. 2021), but spectral hardening is neglected. Higher density filaments expand supersonically, heating the surrounding IHM to $T \sim 10^5$ K through shocks and adiabatic compression. Gas also cools through adiabatic expansion. As a result, the temperature of ionized gas scatters around $T \sim 10^4$ K. Gas at higher densities in mini-haloes slows the I-front as dense gas remains neutral due to self-shielding.

(ii) At later times, mini-haloes photoevaporate, which moves gas from an overdensity of $\Delta \sim 100$ to $\Delta \sim 5$ (see Section 4.4). The photoevaporation time-scale becomes shorter with increasing Γ_{-12}, lowering z_i and the mini-halo mass. The evaporation time is of order 50–100 Myr, which can be several times longer than the sound crossing time. This is the case for haloes of mass $M_h \gtrsim 10^6$ M$_\odot$, which trap the I-front for a long time ($\gg 10$ Myr) due to the short recombination time of their gas.

(iii) Our estimates of mini-halo photoevaporation times agree qualitatively with those of Shapiro et al. (2004) and Iliev et al. (2005a), who performed high-resolution idealized 2D RHD simulations.

In terms of the impact of mini-haloes on the overall recombination rate as quantified by the clumping factor, c_r, we found in Section 4.5 that:

(i) c_r increases rapidly up to a peak value of $c_{r,\,\text{peak}} \sim 20$ as the I-front overruns mini-haloes. The value of $c_{r,\,\text{peak}}$ is higher when Γ_{-12} is higher or z_i is lower (Section 4.5.2). As mini-haloes photoevaporate over a time-scale of ~ 100 Myr, c_r decreases to a value of ≈ 2–4. At this stage, most recombinations occur in the IHM rather than in haloes. Consequently, at the final stages of the EOR, the value of c_r depends only weakly on the value of Γ_{-12}.

(ii) The inhomogeneous IHM increases the reionization photon budget by 20 per cent–100 per cent, depending on the value of the photoionization rate during the EOR (higher values of Γ_{-12} increase the budget) and to a lesser extent the value of z_i (see Fig. 17).

(iii) Low-mass mini-haloes of mass $\ll 10^6$ M$_\odot$ do not contribute significantly to c_r or the reionization photon budget because they photoevaporate very quickly. The relative contribution to the recombination rate as a function of halo mass is plotted in Fig. 16.

We envision the following avenues for further research. First, investigate the effect of the photoevaporating mini-haloes on the value and evolution of the mean-free path of ionizing photons during the EOR. What is the nature of absorbers that dominate the opacity (see e.g. Nasir et al. 2021)? Does this explain the rapid evolution claimed by Becker et al. (2021)? Do these absorbers leave a trace on Lyman-α forest (Park et al. 2023)? Secondly, study the origin of the power-law-like gas density profile ($\rho \propto r^{-2}$) in mini-haloes pre-reionization. Thirdly, predict the shape and evolution of the gas density PDF, as well as the evolution of the PDF of neutral gas before, during, and after the EOR. Finally, it would be worthwhile

to incorporate the results presented here in a subgrid physics model for recombinations (see e.g. Cain et al. 2021, 2023, for effects along these lines). Such a model could then be applied to a simulation at a much lower resolution but in a much larger volume. This would allow for the incorporation of mini-haloes in reionization simulations that can connect with observations of the EOR in upcoming 21-cm surveys.

While this paper focuses on the reionization of a clumpy universe, it also serves as a benchmark of the two-moment method SPHM1RT in cutting-edge cosmological simulations. We are coupling our RHD method to interstellar medium and galaxy models. It will be promising in addressing a multitude of astrophysical problems, ranging from active galactic nuclei, H II regions, to self-consistent reionization.

careful reading of the paper and their valuable comments on its content.

REFERENCES

Abel T., Bryan G. L., Norman M. L., 2002, Science, 295, 93
Altay G., Theuns T., 2013, MNRAS, 434, 748
Barkana R., Loeb A., 2004, ApJ, 609, 474
Becker G. D., D'Aloisio A., Christenson H. M., Zhu Y., Worseck G., Bolton J. S., 2021, MNRAS, 508, 1853
Benitez-Llambay A., Frenk C., 2020, MNRAS, 498, 4887
Benítez-Llambay A. et al., 2017, MNRAS, 465, 3913
Bolton J. S., Haehnelt M. G., 2007, MNRAS, 382, 325
Borrow J., Borrisov A., 2020, J. Open Source Softw., 5, 2430
Borrow J., Schaller M., Bower R. G., Schaye J., 2022, MNRAS, 511, 2367
Bouwens R. J., Illingworth G. D., Oesch P. A., Caruana J., Holwerda B., Smit R., Wilkins S., 2015, ApJ, 811, 140
Bromm V., Coppi P. S., Larson R. B., 2002, ApJ, 564, 23
Bryan G. L., Machacek M., Anninos P., Norman M. L., 1999, ApJ, 517, 13
Cain C., D'Aloisio A., Iršič V., McQuinn M., Trac H., 2020, ApJ, 898, 168
Cain C., D'Aloisio A., Gangolli N., Becker G. D., 2021, ApJ, 917, L37
Cain C., D'Aloisio A., Gangolli N., McQuinn M., 2023, MNRAS, 522, 2047
Calverley A. P., Becker G. D., Haehnelt M. G., Bolton J. S., 2011, MNRAS, 412, 2543
Chan T. K., Theuns T., Bower R., Frenk C., 2021, MNRAS, 505, 5784
Chan T. K., Benitez-Llambay A., Theuns T., Frenk C., 2023, in Dmitry B., Dmitry W., Christian B., eds, Proc. IAU Symp. Vol. 362, The Predictive Power of Computational Astrophysics as a Discovery Tool. Kluwer, Dordrecht, p. 15
Chisholm J. et al., 2018, A&A, 616, A30
Chisholm J. et al., 2022, MNRAS, 517, 5104
Ciardi B., Scannapieco E., Stoehr F., Ferrara A., Iliev I. T., Shapiro P. R., 2006, MNRAS, 366, 689
Courant R., Friedrichs K., Lewy H., 1928, Math. Ann., 100, 32
D'Aloisio A., McQuinn M., Davies F. B., Furlanetto S. R., 2018, MNRAS, 473, 560
D'Aloisio A., McQuinn M., Trac H., Cain C., Mesinger A., 2020, ApJ, 898, 149
Davis M., Efstathiou G., Frenk C. S., White S. D. M., 1985, ApJ, 292, 371
Diemer B., 2018, ApJS, 239, 35
Doussot A., Trac H., Cen R., 2019, ApJ, 870, 18
Draine B. T., 2011, Physics of the Interstellar and Intergalactic Medium. Princeton Univ. Press, Princeton, NJ
Emberson J. D., Thomas R. M., Alvarez M. A., 2013, ApJ, 763, 146
Fan X. et al., 2006, AJ, 132, 117
Faucher-Giguère C.-A., Lidz A., Zaldarriaga M., Hernquist L., 2009, ApJ, 703, 1416
Fialkov A., Barkana R., Visbal E., 2014, Nature, 506, 197
Finkelstein S. L. et al., 2019, ApJ, 879, 36
Finlator K., Davé R., Özel F., 2011, ApJ, 743, 169
Finlator K., Oh S. P., Özel F., Davé R., 2012, MNRAS, 427, 2464
Furlanetto S. R., Zaldarriaga M., Hernquist L., 2004, ApJ, 613, 1
Furlanetto S. R., Oh S. P., Briggs F. H., 2006, Phys. Rep., 433, 181
George E. M. et al., 2015, ApJ, 799, 177
Gingold R. A., Monaghan J. J., 1977, MNRAS, 181, 375
Gnedin N. Y., 2000a, ApJ, 535, 530
Gnedin N. Y., 2000b, ApJ, 542, 535
Gnedin N. Y., 2014, ApJ, 793, 29
Gnedin N. Y., Abel T., 2001, New Astron., 6, 437
Gnedin N. Y., Hui L., 1998, MNRAS, 296, 44
Gnedin N. Y., Ostriker J. P., 1997, ApJ, 486, 581
Greig B. et al., 2021, MNRAS, 501, 1

HERA Collaboration, 2023, ApJ, 945, 124
Haardt F., Madau P., 2012, ApJ, 746, 125
Hahn O., Abel T., 2011, MNRAS, 415, 2101
Haiman Z., Rees M. J., Loeb A., 1997, ApJ, 476, 458
Haiman Z., Abel T., Madau P., 2001, ApJ, 551, 599
Hand N., Feng Y., Beutler F., Li Y., Modi C., Seljak U., Slepian Z., 2018, AJ, 156, 160
Hunter J. D., 2007, Comput. Sci. Eng., 9, 90
Iliev I. T., Shapiro P. R., Raga A. C., 2005a, MNRAS, 361, 405
Iliev I. T., Scannapieco E., Shapiro P. R., 2005b, ApJ, 624, 491
Iliev I. T., Mellema G., Pen U. L., Merz H., Shapiro P. R., Alvarez M. A., 2006a, MNRAS, 369, 1625
Iliev I. T. et al., 2006b, MNRAS, 371, 1057
Iliev I. T., Mellema G., Shapiro P. R., Pen U.-L., 2007, MNRAS, 376, 534
Iliev I. T. et al., 2009, MNRAS, 400, 1283
Iliev I. T., Mellema G., Ahn K., Shapiro P. R., Mao Y., Pen U.-L., 2014, MNRAS, 439, 725
Jones E., et al., 2001, SciPy: open source scientific tools for Python, http://www.scipy.org/ [Accessed Jun 2023]
Kahn F. D., 1954, Bull. Astron. Inst. Netherlands, 12, 187
Kannan R., Smith A., Garaldi E., Shen X., Vogelsberger M., Pakmor R., Springel V., Hernquist L., 2022, MNRAS, 514, 3857
Katz N., 1992, ApJ, 391, 502
Katz H., Kimm T., Sijacki D., Haehnelt M. G., 2017, MNRAS, 468, 4831
Koopmans L. et al., 2015, in Proc. Sci., Advancing Astrophysics with the Square Kilometre Array (AASKA14), SISSA, Trieste, PoS#001
Loeb A., Barkana R., 2001, ARA&A, 39, 19
Lucy L. B., 1977, AJ, 82, 1013
Madau P., 2017, ApJ, 851, 50
Mason C. A., Treu T., Dijkstra M., Mesinger A., Trenti M., Pentericci L., de Barros S., Vanzella E., 2018, ApJ, 856, 2
McQuinn M., Oh S. P., Faucher-Giguère C.-A., 2011, ApJ, 743, 82
Miralda-Escudé J., Cen R., Ostriker J. P., Rauch M., 1996, ApJ, 471, 582
Miralda-Escudé J., Haehnelt M., Rees M. J., 2000, ApJ, 530, 1
Mo H., van den Bosch F. C., White S., 2010, Galaxy Formation and Evolution. Cambridge Univ. Press, Cambridge, UK
Mortlock D. J. et al., 2011, Nature, 474, 616
Naidu R. P., Tacchella S., Mason C. A., Bose S., Oesch P. A., Conroy C., 2020, ApJ, 892, 109
Nakatani R., Fialkov A., Yoshida N., 2020, ApJ, 905, 151
Naoz S., Barkana R., 2007, MNRAS, 377, 667
Naoz S., Barkana R., Mesinger A., 2009, MNRAS, 399, 369
Nasir F., Cain C., D'Aloisio A., Gangolli N., McQuinn M., 2021, ApJ, 923, 161
Ocvirk P. et al., 2016, MNRAS, 463, 1462
Okamoto T., Gao L., Theuns T., 2008, MNRAS, 390, 920
Osterbrock D. E., Ferland G. J., 2006, Astrophysics of Gaseous Nebulae and Active Galactic Nuclei. University Science Books, Sausalito, CA
Park H., Shapiro P. R., Choi J.-h., Yoshida N., Hirano S., Ahn K., 2016, ApJ, 831, 86
Park H., Shapiro P. R., Ahn K., Yoshida N., Hirano S., 2021, ApJ, 908, 96
Park H., Lukić Z., Sexton J., Alvarez M., 2023, preprint (arXiv:2309.04129)
Pawlik A. H., Schaye J., van Scherpenzeel E., 2009, MNRAS, 394, 1812
Pawlik A. H., Rahmati A., Schaye J., Jeon M., Dalla Vecchia C., 2017, MNRAS, 466, 960
Planck Collaboration XLVII, 2016, A&A, 596, A108
Planck Collaboration VI, 2020, A&A, 641, A6
Ploeckinger S., Schaye J., 2020, MNRAS, 497, 4857
Pontzen A., Rey M. P., Cadiou C., Agertz O., Teyssier R., Read J., Orkney M. D. A., 2021, MNRAS, 501, 1755
Rahmati A., Schaye J., 2014, MNRAS, 438, 529
Rahmati A., Pawlik A. H., Raičević M., Schaye J., 2013, MNRAS, 430, 2427
Raičević M., Theuns T., 2011, MNRAS, 412, L16
Reed D. S., Bower R., Frenk C. S., Jenkins A., Theuns T., 2007, MNRAS, 374, 2
Ricotti M., Ostriker J. P., 2004, MNRAS, 352, 547
Robertson B. E., 2022, ARA&A, 60, 121

Robertson B. E., Kravtsov A. V., Gnedin N. Y., Abel T., Rudd D. H., 2010, MNRAS, 401, 2463

Robertson B. E. et al., 2013, ApJ, 768, 71

Rosdahl J., Blaizot J., Aubert D., Stranex T., Teyssier R., 2013, MNRAS, 436, 2188

Rosdahl J. et al., 2018, MNRAS, 479, 994

Schaller M., Gonnet P., Chalk A. B. G., Draper P. W., 2016, in Proc. Platform for Advanced Scientific Computing Conf. p. 1, https://dl.acm.org/doi/abs/10.1145/2929908.2929916

Schaller M. et al., 2018, Astrophysics Source Code Library, record ascl:1805.020

Schaller M. et al., 2023, preprint (arXiv:2305.13380)

Shapiro P. R., Giroux M. L., 1987, ApJ, 321, L107

Shapiro P. R., Iliev I. T., Raga A. C., 2004, MNRAS, 348, 753

Sharma M., Theuns T., Frenk C., Bower R., Crain R., Schaller M., Schaye J., 2016, MNRAS, 458, L94

Sharma M., Theuns T., Frenk C., Bower R. G., Crain R. A., Schaller M., Schaye J., 2017, MNRAS, 468, 2176

Shull J. M., Harness A., Trenti M., Smith B. D., 2012, ApJ, 747, 100

Skinner D., Wise J. H., 2020, MNRAS, 492, 4386

Springel V., 2005, MNRAS, 364, 1105

Springel V., Hernquist L., 2002, MNRAS, 333, 649

Stecher T. P., Williams D. A., 1967, ApJ, 149, L29

Tegmark M., Silk J., Rees M. J., Blanchard A., Abel T., Palla F., 1997, ApJ, 474, 1

Theuns T., 2021, MNRAS, 500, 2741

Trac H., Cen R., 2007, ApJ, 671, 1

Trenti M., Stiavelli M., 2009, ApJ, 694, 879

Tricco T. S., Price D. J., 2012, J. Comput. Phys., 231, 7214

Tseliakhovich D., Hirata C., 2010, Phys. Rev. D, 82, 083520

Viel M., Haehnelt M. G., Springel V., 2004, MNRAS, 354, 684

Visbal E., Haiman Z., Bryan G. L., 2014, MNRAS, 442, L100

van der Walt S., Colbert S. C., Varoquaux G., 2011, Comput. Sci. Eng., 13, 22

Wise J. H., 2019, Contemporary Phys., 60, 145

Wu X., McQuinn M., Eisenstein D., 2021, J. Cosmol. Astropart. Phys., 2021, 042

Wyithe J. S. B., Bolton J. S., 2011, MNRAS, 412, 1926

Zahn O. et al., 2012, ApJ, 756, 65

APPENDIX A: FILTERING AND MINIMUM MINI-HALO MASS

Because the gas temperature in the IHM is finite, the gas density distribution is smoother than that of the dark matter. However, the gas smoothing depends on the entire temperature evolution.

The filtering scale is where the baryonic perturbation are smoothed, given the temperature evolution. The filtering scale can be understood in terms of an evolving Jeans length, as described by Gnedin & Hui (1998). First define the (comoving) Jeans wavenumber, k_J, at a given scale factor (a) as,

$$k_J \equiv \frac{a^{-1/2}}{c_S} \sqrt{4\pi G \overline{\rho}_{m,0}}, \tag{A1}$$

where $\overline{\rho}_{m,0} = \Omega_m \rho_c$ is the average matter density at $z = 0$, and c_S is the sound speed. The filtering wavenumber, k_F, is obtained by integrating Jeans wavenumber over time:

$$\frac{1}{k_F^2(t)} = \frac{1}{D_+(t)} \int_0^t dt' a^2(t') \frac{\ddot{D}_+(t') + 2H(t')\dot{D}_+(t')}{k_J^2(t')} \int_{t'}^t \frac{dt''}{a^2(t'')}, \tag{A2}$$

where D_+ is the linear growth factor.

In a flat Universe, D_+ is equal to the scale factor, a, so $D_+ \propto a \propto t^{2/3}$ at redshifts $z \gtrsim 2$. Therefore,

$$\frac{1}{k_F^2(a)} = \frac{3}{a} \int_0^a \frac{da'}{k_J^2(a')} \left[1 - \left(\frac{a'}{a}\right)^{1/2} \right], \tag{A3}$$

where $z_{dec} = 1/a_{dec} - 1 \approx 130$ is the redshift, where the gas temperature decouples from the CMB temperature.

Before reionization and the onset of any other heating sources, the IHM temperature is:

$$T = \begin{cases} 2.73\text{K}/a & a < a_{dec} \\ 2.73\text{K}a_{dec}/a^2 & \text{otherwise,} \end{cases} \tag{A4}$$

$$c_S^2 = \begin{cases} \frac{\gamma R}{\mu} 2.73\text{K}/a & a < a_{dec} \\ \frac{\gamma R}{\mu} 2.73\text{K}a_{dec}/a^2 & \text{otherwise,} \end{cases} \tag{A5}$$

$$\frac{1}{k_J^2} = \begin{cases} 4\pi G\overline{\rho}_c \frac{\gamma R}{\mu} 2.73\text{K} & a < a_{dec} \\ 4\pi G\overline{\rho}_c \frac{\gamma R}{\mu} 2.73\text{K}a_{dec}/a & \text{otherwise.} \end{cases} \tag{A6}$$

Therefore, the (comoving) Jeans scale is independent of redshift before decoupling.

We combine equations (A3) and (A6) to calculate the filtering wavenumber:

$$\begin{aligned} \frac{1}{k_F^2(a)} &= \frac{3a_{dec}}{a} \int_{a_{dec}}^a \frac{da'}{a'} 4\pi G\overline{\rho}_c \frac{\gamma R}{\mu} 2.73\text{K} \left[1 - \left(\frac{a'}{a}\right)^{1/2} \right] \\ &+ \frac{3}{a} \int_0^{a_{dec}} da' 4\pi G\overline{\rho}_c \frac{\gamma R}{\mu} 2.73\text{K} \left[1 - \left(\frac{a'}{a}\right)^{1/2} \right], \\ &= \frac{3}{k_J^2(a)} \left\{ \int_{a_{dec}}^a \frac{da'}{a'} \left[1 - \left(\frac{a'}{a}\right)^{1/2} \right] \right. \\ &+ \left. \frac{1}{a_{dec}} \int_0^{a_{dec}} da' \left[1 - \left(\frac{a'}{a}\right)^{1/2} \right] \right\}. \end{aligned} \tag{A7}$$

In the simulations, we have neglected the difference between the baryon and dark matter power spectra at the starting redshift. Thus to enable a fair comparison with the simulations, we only integrate equation (A3) from a_{dec} to find,

$$\frac{1}{k_F^2(a)} = \frac{1}{k_J^2(a)} \left[3\ln(a/a_{dec}) - 6 + 6\left(\frac{a_{dec}}{a}\right)^{1/2} \right]. \tag{A8}$$

The filtering mass (equation 3) can then be inferred from the resultant k_F and M_J.

When generating initial conditions for the simulations, we assume that gas traces the dark matter. For consistency, we therefore replace z_{dec} by the starting redshift of the simulations, $z_{ic} = 127$, to estimate M_F in the simulations, with the result plotted in Fig. 1. The resulting value of M_F is lower than that quoted by Gnedin & Hui (1998), who start the integration in the limit of $z \to \infty$. Our estimate of M_F is close to the more accurate calculation performed by Naoz & Barkana (2007), who take account of the fact that the gas and CMB temperatures do not decouple completely at z_{dec}. Presumably this better agreement is mostly coincidental.

APPENDIX B: VARIABLE SPEED OF LIGHT

The time-step in simulations is limited by the Courant–Friedrichs–Lewy condition (CFL, Courant, Friedrichs & Lewy 1928), $\Delta t < \mathcal{C}h/v_{sign}$, where h is the spatial resolution, v_{sign} the signal speed in the simulated fluid, and $\mathcal{C}$ is a constant of order unity. For radiation, the signal speed is the speed of light ($v_{sign} = c$), so this time-step is often many orders of magnitude smaller than that for the fluid itself,

where the signal speed is of the order of the sound speed. Therefore, the inclusion of RT can dramatically reduce the time step and, in turn, increases the compute time.

However, even though radiation travels with speed c, I-front typically travel much slower, see, for example, equation (7). Gnedin & Abel (2001) first suggested that reducing the speed of light, $c \rightarrow \tilde{c} \ll c$, would improve the computational speed of the code without sacrificing its accuracy: this is the 'reduced speed of light' approximation (hereafter RSL). The essential idea is that the state of the gas, when it is in equilibrium with the radiation (e.g. photoionization equilibrium), is independent of the propagation speed. In fact, the RSL approximation may give accurate results even in some non-equilibrium situations, provided the light crossing time is much shorter than other time-scales (see e.g. Rosdahl et al. 2013; Chan et al. 2021).

The required $\tilde{c}$ varies across the simulation volume. Indeed, I-front moves fast in low-density regions, and hence $\tilde{c}$ should not be much smaller than c. However, such a large $\tilde{c}$ results in very short time-steps in high-density regions,[28] where h is small. Fortunately, the I-front speed is actually very low in dense regions, so we could apply a much lower value of $\tilde{c}$ without loss of accuracy. Therefore, it is very tempting to allow $\tilde{c}$ to *vary* in space and time. This is the variable speed of light approximation (hereafter VSL, e.g. one VSL version in Katz et al. 2017).

The first requirement (1) of a VSL scheme is to keep the equilibrium photoionization rate independent of $\tilde{c}$, so does the equilibrium neutral gas fraction. The photoionization rate is proportional to the number density of photons, the speed of light, and the photoionization cross-section, that is, $n_\gamma c \sigma_{HI}$. This implies that the product of the radiation density times the RSL, $n_\gamma \tilde{c}$, and the radiation flux should not change when $\tilde{c}$ is used.[29]

The second requirement (2) is that the scheme should reduce to the RSL approximation when $\tilde{c}$ is uniform.

For reference, the terms entering the rate of change of radiation variables that involve spatial derivatives of these variables (and hence are computed by summing over SPH neighbours that may have a different value of $\tilde{c}$), are given by (see Chan et al. 2021, their equations 5–7),

$$\left(\frac{D\xi}{Dt} \right) \Big|_{\text{prop}} = -\frac{1}{\rho} \nabla \cdot (\rho \mathbf{f}), \tag{B1}$$

$$\frac{D\mathbf{f}}{Dt} \Big|_{\text{prop}} = -\tilde{c}^2 \frac{\nabla \cdot (\xi \mathbb{F})}{\rho}, \tag{B2}$$

where the subscript 'prop' means that we only write terms that involve the propagation of radiation across particles. We are going to modify these equations for VSL, so that they can be applied consistently even if two particles that exchange radiation have different values of $\tilde{c}$. To be definite, let these particles be i and j, with RSL values $\tilde{c}_i$ and $\tilde{c}_j$.

To satisfy requirements (1) and (2), we devise a new three-step VSL scheme, as illustrated in Fig. B1. In short, (A) we transform the equations to a system with a common RSL, $\tilde{c}_0$. Next, (B) we solve the propagation equation with $\tilde{c}_0$. Finally, (C) we transform the equations back to the $\tilde{c}_i$ and $\tilde{c}_j$.
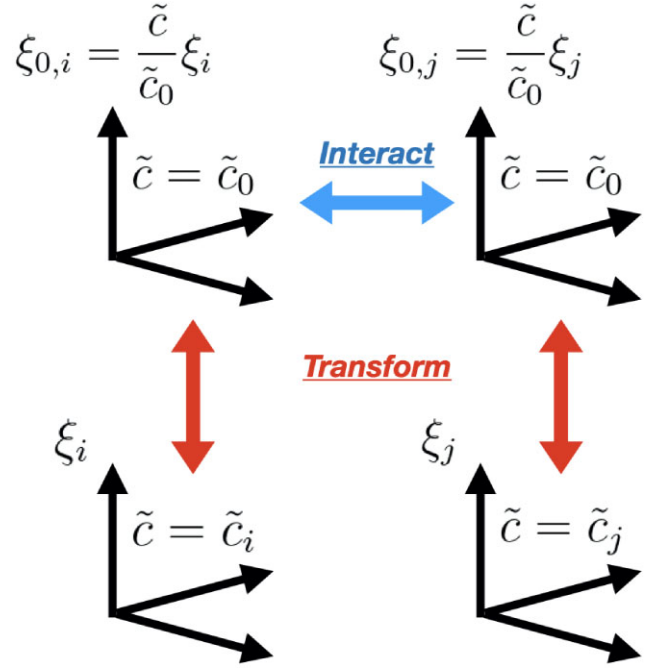
Figure B1. Schematic diagram illustrating our VSL implementation. The left and right lower panels represent particles i and j with different specific radiation energies ξ and RSL $\tilde{c}$, respectively. To evaluate the energy and flux exchanges, particles i and j are transformed to a frame with an RSL $\tilde{c}_0$ (upper panels). After evaluating the particle–particle interaction, radiation variables are transformed back to the original frame.

In the first step (A), we construct a reference frame with $\tilde{c}_0$ and then transform the quantities from the local (particle i) frame (with the RSL $\tilde{c}_i$) to the reference frame through:

$$\xi_i \rightarrow \frac{\tilde{c}_0}{\tilde{c}} \xi_{0,i}; \quad \mathbf{f}_i \rightarrow \mathbf{f}_{0,i}, \tag{B3}$$

where we label the $\tilde{c}_0$ reference frame with the subscript '0'. We apply the same transform for particles j, the neighbourhood particles of i. In this transform, $\rho\mathbf{f}$ and $\rho\tilde{c}\xi$ are invariant, so the radiation energy density in the reference frame is equal to that in the original frame, that is, $\rho\tilde{c}_0\xi_0 = \rho\tilde{c}_i\xi_i$, so this satisfies the requirement (1).

Hence, the radiation equations in the $\tilde{c}_0$ frame become:

$$\left(\frac{D\xi_0}{Dt} \right) \Big|_{\text{prop}} = -\frac{1}{\rho} \nabla \cdot (\rho \mathbf{f}_0), \tag{B4}$$

$$\frac{D\mathbf{f}_0}{Dt} \Big|_{\text{prop}} = -\tilde{c}_0^2 \frac{\nabla \cdot (\xi_0 \mathbb{F}_0)}{\rho}. \tag{B5}$$

In the second step (B), we solve equations (B4) and (B5) in one neighbourhood by applying the SPH algorithm to evaluate the derivatives,

$$\left(\frac{D\xi_{0,i}}{Dt} \right) \Big|_{\text{prop}} = -\sum_j \frac{m_j}{\Omega_i \rho_i^2} (\rho_i \mathbf{f}_{0,i} - \rho_j \mathbf{f}_{0,j}) \cdot \nabla_i W_{ij}(h_i), \tag{B6}$$

and

$$\left(\frac{D\mathbf{f}_i}{Dt} \right) \Big|_{\text{prop}} = -\sum_j \frac{m_j \tilde{c}_0^2}{\Omega_i \rho_i^2} \left(\rho_i \xi_{0,i} \mathbb{F}_{0,i} - \rho_j \xi_{0,j} \mathbb{F}_{0,j} \right) \cdot \nabla_i W_{ij}(h_i). \tag{B7}$$

Note that we have to pick the 'difference' SPH differential form (e.g. see Tricco & Price 2012; Chan et al. 2021) if the speed of light changes discontinuously. Otherwise, the estimated gradient

will be inaccurate, which would lead to numerical reflections at discontinuities.

In the final step (C), we convert back to the local ($\tilde{c}_i$) frames,

$$\xi_{0,i} \rightarrow \frac{\tilde{c}}{\tilde{c}_0}\xi_i; \quad \mathbf{f}_{0,i} \rightarrow \mathbf{f}_i, \tag{B8}$$

and similarly for particle j.

The solution will depend on our choice for $\tilde{c}_0$. We take $\tilde{c}_0 = \max(\tilde{c}_i, \tilde{c}_j)$ for each pairwise interaction term to ensure symmetry and recover the RSL limit [i.e. satisfying the requirement (2)]. In experiments, we found that the choice of $\tilde{c}_0$ makes little difference,[30] as long as (I) $\tilde{c}_0$ is between $\tilde{c}_i$ and $\tilde{c}_j$ and (II) $\tilde{c}_0$ is symmetric with respect to i and j.

We also apply these changes to the artificial diffusion (see section 2.5 in Chan et al. 2021).

$$\left.\frac{\mathrm{D}\tilde{\xi}_{0,i}}{\mathrm{D}t}\right|_{\mathrm{diss}} = \sum_{j=1}^{N} D_{\xi,ij}\frac{m_j}{\rho_i \rho_j}(\rho_i\xi_{0,i} - \rho_j\xi_{0,j})\frac{\hat{\mathbf{r}}_{ij} \cdot \overline{\nabla_i W_{ij}}}{r_{ij}}, \tag{B9}$$

and artificial viscosity:

$$\left.\frac{\mathrm{D}\mathbf{f}}{\mathrm{D}t}\right|_{\mathrm{diss}} = \frac{1}{\rho}\nabla \cdot \left[\mathbb{D}^{\mathbf{f}}\nabla \cdot (\rho\mathbf{f})\right], \tag{B10}$$

where $\mathbb{D}^{\mathbf{f}}$ is given by

$$\mathbb{D}^{\mathbf{f}} = \alpha_{\mathbf{f}} v_{\mathrm{sig}} h\hat{\mathbf{n}}\hat{\mathbf{n}}. \tag{B11}$$

Eequation (B10) has to be solved with the 'difference' SPH form too.
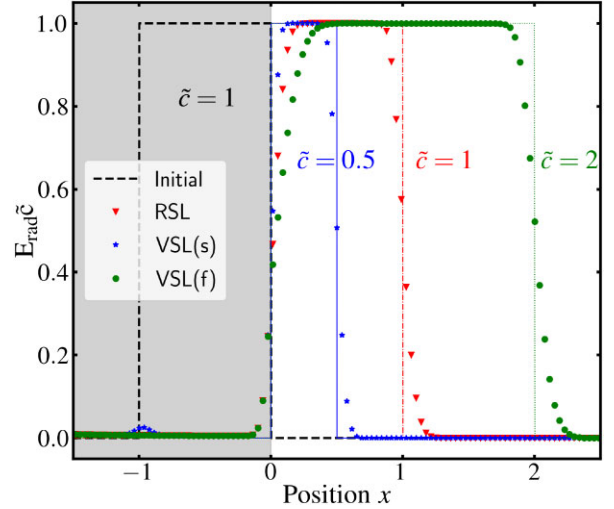
We demonstrate the robustness of our scheme in Fig. B2, which shows a case of radiation propagation in the optically thin limit. We consider a rapid change of $\tilde{c}$ at $x = 0$ and investigate whether our scheme can work in the following aspects.

First, both RSL(s) and VSL(f) keep the product $E_{\mathrm{rad}}\tilde{c}$ approximately constant within the plateau region, so they have the same ionizing power. Second, both the VSL(s) and VSL(f) profiles follow $\tilde{c}$ specified in different regions. For example, the VSL(s) line reaches $x = 0.5$ at $t = 1$ (with $\tilde{c} = 0.5$). To achieve this speed, the VSL(s) profile is compressed by a factor of two. Third, we have explicitly checked that photon conservation is better than 1 per cent in all runs even with sudden changes in $\tilde{c}$. Finally, our scheme is also robust during the transition. Even with a rapid change in $\tilde{c}$ at $x = 0$, the radiation profile at $x = 0$ is remarkably smooth.

The second test is the 1D photoionization test in Fig. B3. A constant photon flux is injected from the left and recombinations balance photoionizations. In the VSL runs, the RSL increases or decreases by a factor of ten at $x = 0$. We find that the equilibrium neutral fraction profiles computed with the VSL approximation match well that computed with the RSL approximation, demonstrating the accuracy of the VSL implementation.

The final test is a 3D isothermal Strömgren sphere (Iliev et al. 2006b, test 1) in Fig. B4. A source at the centre is emitting ionizing radiation at a constant rate of $\dot{N}_\gamma = 5 \times 10^{48}$ photons s^{-1}. The volume has a linear extent of 20 kpc, filled with 32^3 gas particles in a glass-like distribution. The gas is pure hydrogen with density $n_{\mathrm{H}} = 10^{-3}$ cm^{-3}. The collisional ionization coefficient is $\beta = 3.1 \times 10^{-16}$ cm^3 s^{-1}, whereas the recombination coefficient is $\alpha_{\mathrm{B}} = 2.59 \times 10^{-13}$ cm^3 s^{-1} (with the on-the-spot approximation). The photoionization cross-section is $\sigma_{\gamma\mathrm{HI}} = 8.13 \times 10^{-18}$ cm^2. We apply the VSL approximation such that $\tilde{c} = 0.05c$ for $r < 4$ pkpc and
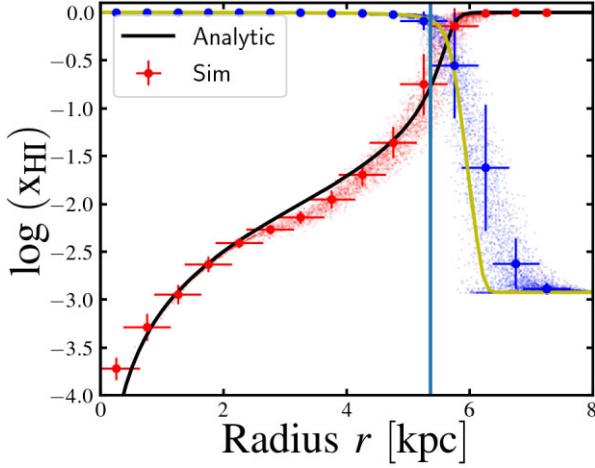

Figure B2. Tests of the RSL and VSL implementation, in which a packet of radiation streams in the optically thin limit from left to right. Shown in all cases is the product of the energy density times $\tilde{c}$, which is independent of the choice of $\tilde{c}$. The black dashed line is the initial shape of the packet, with thin coloured lines the correct solution at later times. The corresponding numerical solution in the RSL case with $\tilde{c} = 1$ is shown as downwards triangles. The stars and circles correspond to the numerical solution in the VSL approximation, which uses $\tilde{c} = 1$ for $x < 0$ and $\tilde{c} = 0.5$ and $\tilde{c} = 2.0$, for $x > 0$, respectively. The numerical calculation uses 10^3 particles in one dimension, and in all cases is shown at time $t = 1$. The simulation reproduces the correct solution, apart from the inevitable diffusion associated with the SPH scheme.
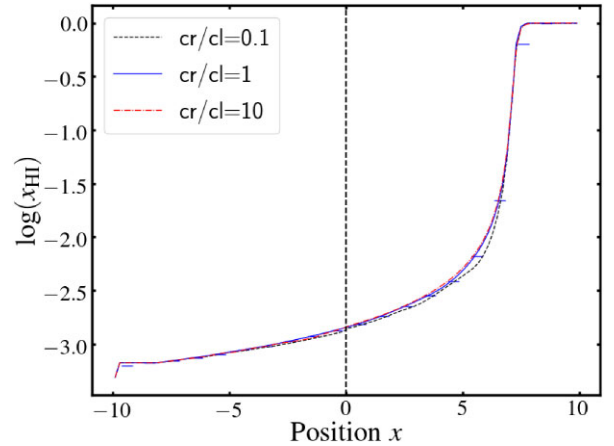
Figure B3. Neutral gas fraction, $x_{\mathrm{HI}} = n_{\mathrm{HI}}/n_{\mathrm{H}}$, in a 1D photoionization test of the VSL approximation. We use dimensionless variables, in which the simulation volume contains 100 gas particles with hydrogen density $n_{\mathrm{H}} = 1.0$, photoionization cross-section $\sigma_{\mathrm{HI}} = 10^2$ and recombination coefficient $\alpha_{\mathrm{B}} = 4.0$. Radiation is injected at the location $x = -8$ with a constant radiation flux $F_\gamma = 60$. Different curves show the run of x_{HI} with x for simulations with different values of RSL with cr the value of RSL at $x > 0$ in units of the RSL at $x < 0$. Small horizontal lines indicate the local value of the smoothing length. The profile is shown at time $t = 10^2$ when x_{HI} is in equilibrium. The test shows that the equilibrium value does not depend on the choice of the RSL.

---

[30]The RSL solution will also depend on $\tilde{c}$, for example, in the optically thin limit. But the equilibrium solution, for example, Strömgren sphere, will not.

Figure B4. Isothermal Strömgren sphere from Iliev et al. (2006b). Test 1: a source of radiation, located at radius $r = 0$, photoionizes hydrogen gas, kept at constant density and constant temperature. The system is shown a time $t = 500$ Myr after the source is switched on. Red points (from bottom left to top right) are the neutral hydrogen fraction, $x_{HI} = n_{HI}/n_H$, of individual gas particles, with the red circles with errorbars showing binned values, with horizontal error bars indicating the bin width, and vertical error bars the standard deviation; the black line (around red points) is the analytical solution. Small blue points (from top left to bottom right), and blue circles with error bars show the corresponding ionized fraction, $1 - x_{HI}$, with the yellow line the analytical solution. The vertical solid line is the approximate analytic location of the Strömgren radius. In this VSL test, $\tilde{c}$ increases by a factor two at $r = 4$ kpc. This has little effect on the numerical solution, which is almost identical to the case where $\tilde{c}$ is constant (fig. B4 in Chan et al. 2021).

$\tilde{c} = 0.1c$ for $r > 4$ pkpc. Even with a sudden change of $\tilde{c}$ by a factor of two, the equilibrium neutral fraction profile still agrees well with the analytic solution (from Chan et al. 2021).

Our VSL scheme improves upon the original scheme described by Katz et al. (2017) as follows. Our scheme allows for adaptive time stepping without the need for subcycling. Our scheme can also be applied to any moment-based RT scheme, for example, adaptive mesh refinement, moving mesh, or any meshless method.

APPENDIX C: COSMOLOGICAL RADIATIVE TRANSFER

To account for cosmological expansion, we convert from proper to comoving variables in the usual way,

$$\mathbf{r} = a\mathbf{r}'; \ \chi = a^2 \chi'; \ \rho = \frac{1}{a^3}\rho'; \ W_{ij}(h) = \frac{1}{a^3}W_{ij}'(h');$$

$$\nabla_i = \frac{1}{a}\nabla_i'; \ \nabla_i W_{ij}(h) = \frac{1}{a^4}\nabla' W_{ij}'(h'); \ \dot{r}' = \frac{1}{a^2}v'; \ \frac{\dot{a}}{a} = H, \ \text{(C1)}$$

where primed variables are comoving and a is the expansion factor. Furthermore, $\mathbf{r}$ is position, χ opacity, ρ gas density, W is the kernel, and ∇ the gradient operator.

Furthermore, we transform the radiation quantities as follows:

$$\xi = \xi'; \ \mathbf{f} = a\mathbf{f}'; \ \tilde{c} = a\tilde{c}'; \ \mathbb{P} = \frac{1}{a^3}\mathbb{P}'. \ \text{(C2)}$$

Here, $\xi (= E_{rad}/\rho)$ is the ratio of the radiation energy density over the gas density $\mathbf{f}$ is the ratio of the radiative flux over the gas density and $\mathbb{P}$ is the radiation stress tensor (see table 1 in Chan et al. 2021). Our choice accounts only for the cosmological dilution of photons but not the redshifting of the wavelengths of photons. As a result, both

gas and photon densities have the same dependency on scale factor, so $\xi = E_{rad}/\rho = E_{rad}'/\rho' = \xi'$.

The primed radiation equations are then unchanged from the original proper equations,

$$\frac{D\xi'}{Dt} = -\frac{1}{\rho'}\nabla' \cdot (\rho'\mathbf{f}'), \ \text{(C3)}$$

$$\frac{1}{\tilde{c}'^2}\frac{D}{Dt}\mathbf{f}' = -\frac{\nabla' \cdot \mathbb{P}'}{\rho'} - \frac{\chi'\rho'}{\tilde{c}'}\mathbf{f}', \ \text{(C4)}$$

if we neglect small cosmological terms when the scale factor changes slowly. These are small corrections for the current application[31] and ignored in many previous works, for example, in Shapiro & Giroux (1987) and Rosdahl et al. (2013).

We verify the implementation of these equations by simulating the evolution of a cosmological H II region in a homogeneous, constant-temperature, matter-dominated flat universe, with 10 per cent of its mass density in hydrogen (and neglecting helium). The hydrogen is initially fully neutral and is ionized by a source that switches on at $z_i = 9$, emitting ionizing radiation at a constant rate of $\dot{N}_\gamma = 5 \times 10^{48}$ photons s^{-1} at $h\nu = 13.6$ eV (and keeping the temperature constant). The collisional ionization coefficient is $\beta = 3.1 \times 10^{-16}$ cm^3 s^{-1}, whereas the recombination coefficient is $\alpha_B = 2.59 \times 10^{-13}$ cm^3 s^{-1} (at $T = 10^4$ K); making the on-the-spot approximation. The photoionization cross-section is $\sigma_{\gamma HI} = 8.13 \times 10^{-18}$ cm^2.

In the non-cosmological case, provided the density and temperature are uniform and constant, the I-front initially moves at the speed of light, before slowing down to the speed derived in equation (7) which eventually approaches zero due to recombinations. Its position r_I as a function of time is given by

$$y(t) \equiv \left(\frac{r_I(t)}{r_S}\right)^3 \to 1 - \exp\left(-\frac{t - t_i}{t_r}\right). \ \text{(C5)}$$

Here, t_i is the time that the sources switches on, t_r is the recombination time, $t_r^{-1} = \alpha_B n_H$, and $r_S = \left(3t_r\dot{N}_\gamma/(4\pi n_H)\right)^{1/3}$ is the Strömgren radius.

In the cosmological case, the I-front initially also moves at the speed of light before slowing down as described by equation (7). However, the Strömgren radius increases as the density decreases due to the expansion of the Universe, $R_s \propto a^2$ (provided the temperature is taken to be constant, rather than decreasing with the gas density). As a consequence, the ratio r_I/r_S decreases again at late times. The analytical solution is given by (Shapiro & Giroux 1987)

$$y(t) \to \lambda \exp\left(\lambda\frac{t_i}{t}\right)\left[\frac{t}{t_i}E_2\left(\lambda\frac{t_i}{t}\right) - E_2(\lambda)\right], \ \text{(C6)}$$

where E_2 is the exponential integral of order 2, and the constant λ is the ratio of the initial time over the initial recombination time, $\lambda \equiv t_i/t_r(t_I)$.

We simulate the set-up using 64^3 gas particles in a computational volume with a linear extent of 40 ckpc, using $\tilde{c} = 0.01\,c$, and compare the outcome to the analytical solution in Fig. C1. The H II region is not well resolved initially, but at later times the agreement between the simulation and the analytical result is excellent. The good agreement at late times demonstrates that our choice of comoving radiation variables works correctly.

---

[31]One of the neglected terms is the cosmological redshifting of the wavelength of photons. This is relevant for those photons that can travel over distances comparable to the *Hubble* distance, but not for the ionizing photons that have a mean-free path of only a few Mpc in our set-up.
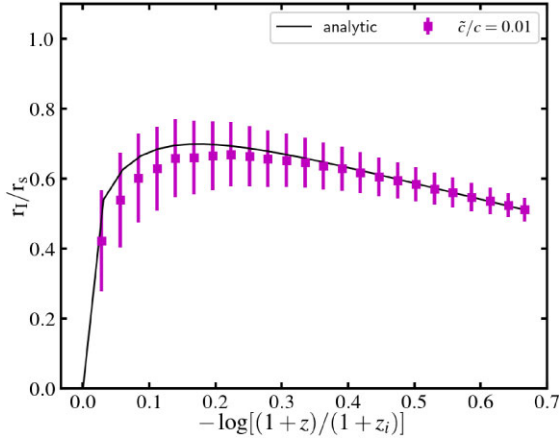
Figure C1. I-front location, r_I, divided by the Strömgren radius, r_S, as a function of redshift; r_I is operationally defined as the location where 50 per cent of the gas is ionized. The source switches on at redshift $z_i = 9$. Squares with errorbars show the simulation result, with error bars depicting the gas smoothing lengths divided by r_S. The solid line is the analytic solution from Shapiro & Giroux (1987).

APPENDIX D: NUMERICAL CONVERGENCE

D1 Choice of clumping factor

In this section, we contrast various definitions of the clumping factor, c_r, that appear in the literature. For the first three of those, we only consider gas that is downstream of the I-front (as we did in the main text).

The first definition is c_l from Emberson et al. (2013):

$$c_l = \frac{\langle n_{\mathrm{HII}}^2 \rangle_{\mathrm{IF}}}{\langle n_{\mathrm{HII}} \rangle_{\mathrm{IF}}^2}. \tag{D1}$$

This expression does not account for any spatial variations in temperature in the ionized regions. Such variations affect the value of the recombination rate.

The second definition is c_r from Park et al. (2016), as used in the main text (equation 33). This expression does account for spatial variations in the temperature: the denominator evaluates the recombination rate at the mass-averaged temperature, $\bar{T}_{\mathrm{IF}}$.

The third definition is $c_{r,V}$, which is similar to the second definition, except that the recombination rate is evaluated at the volume averaged temperature, $\langle T \rangle_{\mathrm{IF}}$, yielding

$$c_{r,V} \equiv \frac{\langle \alpha_{\mathrm{B}}\, n_{\mathrm{HII}}^2 \rangle_{\mathrm{IF}}}{\alpha_{\mathrm{B}}(\langle T \rangle_{\mathrm{IF}})\, \langle n_{\mathrm{HII}} \rangle_{\mathrm{IF}}^2}. \tag{D2}$$

The fourth definition is similar to D'Aloisio et al. (2020). We evaluated the recombination rate at $T = 10^4$ K:

$$c_{r,V} \equiv \frac{\langle \alpha_{\mathrm{B}}\, n_{\mathrm{HII}}^2 \rangle_{\mathrm{IF}}}{\alpha_{\mathrm{B}}(10^4\mathrm{K})\, \langle n_{\mathrm{HII}} \rangle_{\mathrm{IF}}^2}. \tag{D3}$$

In the fifth definition, we consider all gas in the computational volume:

$$c_{l,\mathrm{all}} = \frac{\langle n_{\mathrm{HII}}^2 \rangle}{\langle n_{\mathrm{H}} \rangle^2}. \tag{D4}$$

Unlike the previous definitions, the recombination rate can be estimated from $c_{l,\mathrm{all}}$ without knowing the ionization fraction of the volume.

We have computed these clumping factors in simulation M512z8G03 and they are plotted as a function of time since the
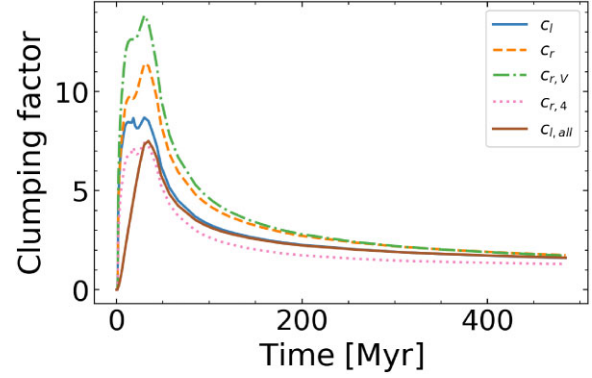
Figure D1. Evolution of the clumping factor in simulation M512z8G03, where $t = 0$ is the instance the I-front enters the simulation volume. Different curves correspond to different definition of the clumping factor, as described in Appendix D1.

I-front entered the computational volume in Fig. D1. All clumping factors exhibit a similar evolution: a fast rise to a peak value, followed by a decline to an asymptotic value.

The clumping factor c_r that we use in the main text (i.e. computed following the second definition, equation 33) is larger than c_l by $\sim$30 per cent, which is due to spatial variation in the temperature which c_r accounts for. In the simulations, dense gas is shielded and remains cooler than lower density gas. The lower temperature increases the recombination rate in the numerator, and hence the clumping factor (see also fig. 2 in Park et al. 2016). On the other hand, c_r is smaller than $c_{r,V}$ by $\sim$30 per cent. This is because the volume-averaged temperature (used in $c_{r,V}$) is higher than the mass-averaged temperature (used in c_r), hence $\alpha_{\mathrm{B}}(\langle T \rangle) < \alpha_{\mathrm{B}}(\bar{T})$, since $\alpha_{\mathrm{B}}(T) \propto T^{-0.7}$. However, both $c_{r,V}$ and c_r can be accurate measures of recombination rate, as long as the corresponding α_{B} is accounted for when computing the net recombination rate in equation (33). $c_{r,4}$ is lower than both $c_{r,V}$ and c_r, because the reference temperature $T = 10^4$ K is lower than the mean temperature of the ionized gas. Finally, $c_{l,\mathrm{all}}$ is the lowest since it considers all of the gas in the denominator. It quickly converges to c_l when all of the volume is ionized, around 50 Myr in this simulation.

All definitions here converge to the same asymptotic value (times $t \geq 400$ Myr in this simulations), because once the volume is ionized, temperature variations are relatively small. However, at earlier times, it is important to use the same definition of the clumping factor when comparing numerical simulations, given the 30 per cent–60 per cent differences that we find. We think that c_r or $c_{r,V}$ are preferred, since they capture the initial spatial temperature fluctuations better.

D2 Convergence with the value of $\tilde{c}$

We use an RSL approximation, $c \to \tilde{c} \ll c$, in the simulations: this improves computational efficiency. The value of $\tilde{c}$ is further allowed to vary spatially: this is the VSL approximation, described in Appendix B.

We test by how much we can reduce $\tilde{c}$ in the VSL approximation and still capture accurately the evolution of the clumping factor c_r in Fig. D2. The value of c_r at its peak is constant to within 10 per cent–15 per cent provided $\tilde{c} \geq 0.1\, c$. This justifies our choice of $\tilde{c} = 0.15\, c$ in the main simulations. The asymptotic value of c_r does not dependent on the choice of $\tilde{c}$, provided $\tilde{c} \geq 0.05$.
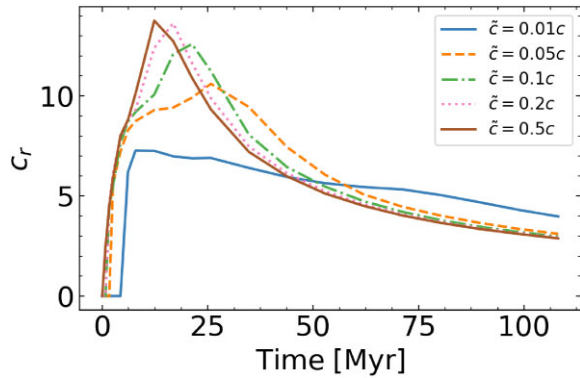
Figure D2. Convergence of the clumping factor for different RSL $\tilde{c}$ (at the mean density of the simulation volume). We consider the small box (400 ckpc), $\Gamma_{-12} = 0.3$, and $m_{\rm gas} = 20\,{\rm M_\odot}$ (i.e. the S256G03 runs in Table 1). The peak clumping factor converges at $\tilde{c} \sim 0.2c$, which is around the value we adopt in the production runs.
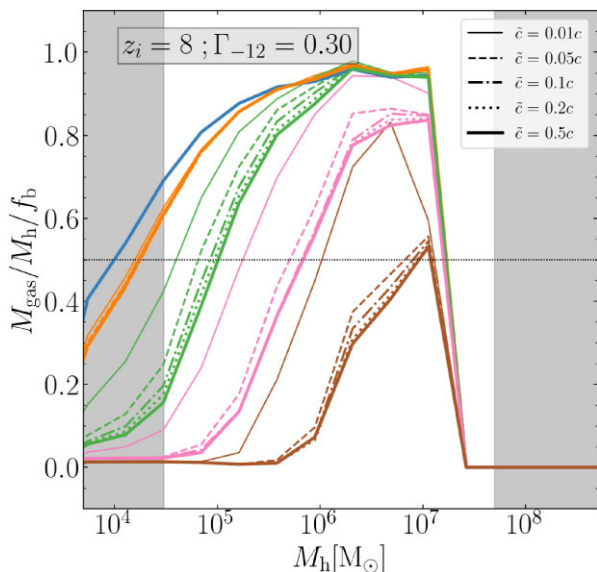

Figure D3. Ratio between gas mass within the virial radius and the halo mass, in units of the cosmic baryon fraction, f_b. It is similar to Fig. 4, but for simulations performed with different values of the RSL $\tilde{c}$, as per the legend. Different colours correspond to different times, $t_{\rm dur}$, since the halo was over-run by I-front, from blue (left-most; recently) to brown (right-most; long ago) (see Fig. 4 legend). The baryon fractions converge to better than 10 per cent when $\tilde{c} > 0.05c$, and significantly better when $\tilde{c} > 0.1c$.

D3 Convergence with particle mass

We have performed simulations with different mass resolutions in the same cosmological volume to verify the level of numerical convergence, see Table 1. In Fig. D4, we plot the baryon fraction (in units of the cosmological mean value, f_b) as a function of halo mass, for simulations with different particle masses.[32] In our simulations, the baryonic mass fraction of haloes converges to within ~ 30 per cent for halo mass $M_{\rm h} \gtrsim 10^{4.3}\,{\rm M_\odot}$ provided that the dark matter particle mass $m_{\rm DM} \sim 100\,{\rm M_\odot}$ (200 dark matter particles per halo). This agrees well with the findings of Naoz et al. (2009), who

---

[32]The legend gives the dark matter particle mass, the gas-particle mass is $f_b/(1 - f_b)$ time the dark matter particle mass.
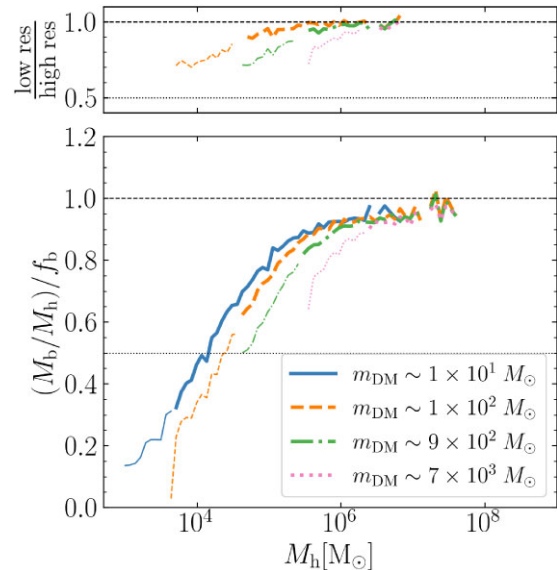
Figure D4. Lower panel: baryon fraction of haloes in units of the cosmic mean, f_b, for simulations with different particles masses (different line styles). Upper panel: the baryon mass divided by the baryon mass of the highest resolution simulation. In both panels, thick (thin) lines refer to haloes resolved with more than (less than) 300 DM particles. Results are shown at redshift $z = 8$, before radiation was injected in the simulations. The baryon fraction is converged to within 20 per cent–30 per cent, provided the halo is resolved with more than ~ 300 particles.

found that ~ 300 particles are needed to reach convergence at the 30 per cent level. Given our fiducial resolution of $m_{\rm DM} \sim 100\,{\rm M_\odot}$, our simulations resolve the baryon fraction of haloes of mass $M_{\rm min}$ to within 30 per cent. Here, $M_{\rm min}$ is the minimum mass of haloes that retain 50 per or more of their baryons, as discussed in Section 2.1.

We examine the impact of finite-mass resolution on the photoevaporation of mini-haloes in Fig. D5. At a given halo mass, mini-haloes evaporate faster at lower resolution. This is partially because the central gas density is lower when the profile is not well resolved, which enables the I-front to propagate deeper into the halo. This effect is less pronounced at higher halo masses, $M_{\rm h} > 5 \times 10^6\,{\rm M_\odot}$, because these are reasonably well resolved at our coarsest numerical resolution of $m_{\rm DM} \sim 6400\,{\rm M_\odot}$.

The impact of resolution on the evolution of c_r is illustrated in Fig. D6. Simulations with different resolutions agree well and the clumping factors converge at $m_{\rm DM} \lesssim 800\,{\rm M_\odot}$. Somewhat surprisingly, this conclusion is different from that reached by Emberson et al. (2013), who found that the clumping factor converges only at $m_{\rm DM} \lesssim 100\,{\rm M_\odot}$. We suspect that the reason is that Emberson et al. (2013) did not account for the photoevaporation of mini-haloes. Lower mass mini-haloes contribute significantly to c_r but only in the very early stages of the EOR. Once this photoevaporate, c_r is determined by more massive mini-haloes which can be sufficiently resolved even when $m_{\rm DM} = 800\,{\rm M_\odot}$.

We verify this scenario in Fig. D7 in which we plot the recombination rate as a function of overdensity at the instance when c_r is near its peak. Although the contribution of haloes with mass $M_h < 10^6\,{\rm M_\odot}$ depends on resolution, they do not contribute significantly to the recombination rate at this stage of the evolution (this conclusion will depend on z_i, since lower mass haloes contribute more at higher z). The value of c_r is dominated by haloes with mass in the range $10^{6-8}\,{\rm M_\odot}$ haloes, which can be resolved sufficiently well at a particle
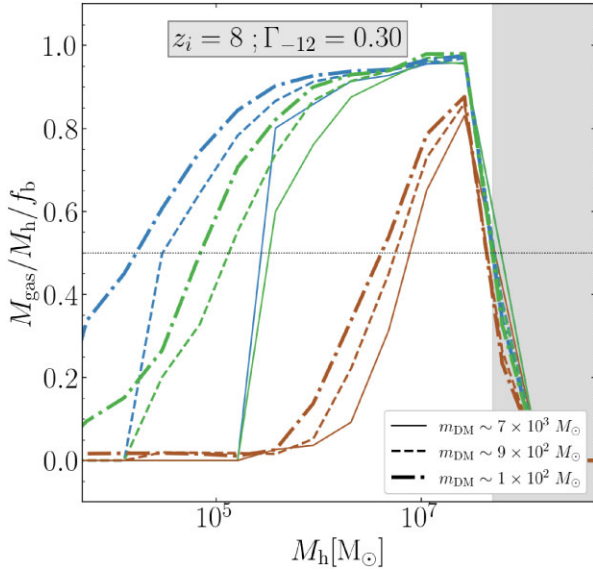
Figure D5. Ratio between gas and halo mass, in units of the cosmic baryon fraction, f_b. It is similar to Fig. 4, but for simulations with different particles masses (plotted using different line styles). Different colours correspond to different times, t_{dur}, since the halo was over run by I-front: blue (left): 1 Myr; green (middle): 20 Myr; and brown (right): 100 Myr. The simulation volume is 800 ckpc on a side. Higher resolution simulations yield longer photoevaporation time-scales at a given halo mass.
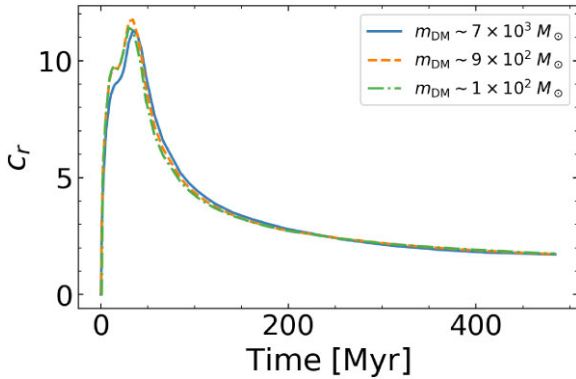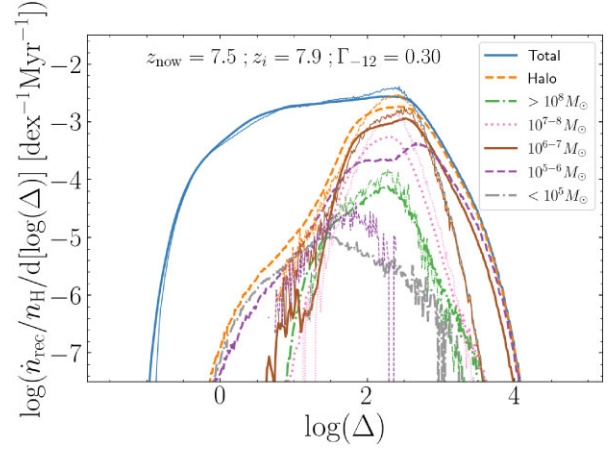

Figure D6. As Fig. D3, but for simulations with different particles masses. The simulation volume is 800 ckpc on a side, and we use $\Gamma_{-12} = 0.3$, and $z_i = 8$. The evolution of the clumping factor differs by less than 5 per cent between these runs.

resolution of $m_{DM} \lesssim 10^3 \, M_\odot$ (at least in the ionized outer regions).[33] At low Γ_{-12} and/or late times, the clumping factor is dominated by gas at overdensities $\Delta < 100$, and the recombination rate of this gas is resolved well when $m_{DM} < 10^3 \, M_\odot$.

However, mini-haloes need to be resolved spatially as well. A mini-halo with $M_h = 10^6 \, M_\odot$ has a virial radius of ~ 0.3 pkpc at $z \sim 8$. For a quasi-Lagrangian code such as SWIFT, the smoothing length of a gas particle is less than 0.05 kpc at the critical self-shielding density ($n_S \sim 0.1 \, cm^{-3}$) and even smaller at higher density, when $m_{DM} \lesssim 800 \, M_\odot$ (and when using equal numbers of dark matter and

gas particles). Therefore, spatial resolution is not a limiting factor in our calculations.

In contrast, spatial resolution may be challenging in mesh-based simulations, for example, uniform mesh methods might have difficulties resolving the central parts of mini-haloes (see e.g. the convergence test in the appendix of D'Aloisio et al. 2020). Artificial diffusion can be problematic when the gas moves at high speed across a static mesh (Robertson et al. 2010). This can suppress the formation of structures that are not well resolved (Pontzen et al. 2021). Whether and how this affects the value of c_r in mesh simulations may require further study.

In summary, a dark matter particle resolution of $m_{DM} \lesssim 100 \, M_\odot$ is needed to model the photoevaporation of mini-haloes (provided that the adaptive spatial resolution is high enough).[34] This can be relaxed to $m_{DM} \lesssim 10^3 \, M_\odot$ for studies of the clumping factor, because the lower mass haloes that are not well resolved at this coarser resolution contribute little to c_r.
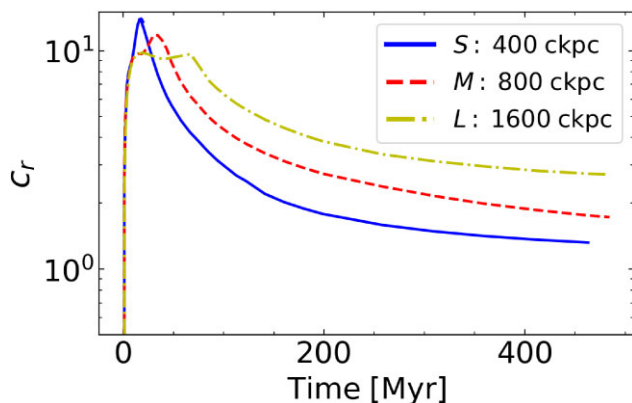
D4 Convergence with simulation volume

We quantify the impact of simulation volume on the halo mass function in Fig. D8. We consider three cubic volumes, S, M, and L, with linear extents $L_c \sim 400$, ~ 800, and ~ 1600 ckpc, respectively. The numerical resolution is the same in these three runs. Not surprisingly, the number of haloes with mass $M_h > 10^8 \, M_\odot$ is severely underestimated in simulation S. Such haloes are significant photon sinks at the end of the EOR and later, and clearly the simulation volume needs to be large enough to sample them correctly (see also appendix C of Cain et al. 2020). Our production runs are performed

Figure D7. As Fig. 16, showing the contribution to the recombination rate as a function of overdensity with different linestyles depicting the net contribution of haloes of different mass. Results are shown at the instance that $c_r = c_{r, peak}$. The thick lines are for simulation M512z8G03 (particle mass $m_{DM} = 120 \, M_\odot$), the thin lines are simulation M128z8G03 (with $m_{DM} = 9600 \, M_\odot$). The simulations differ significantly for haloes with with mass $M_h < 10^6 \, M_\odot$, but these do not contribute much to the over all recombination rate. For haloes more massive than $M_h = 10^6 \, M_\odot$, the lower resolution simulation yields more recombinations at higher density. This causes the over all recombination rate to be higher at lower resolution.

---

[33]The lower resolution run has slightly higher recombination rate because the I-front propagate faster at lower resolution. It is because low-resolution runs have fewer structures to impede I-front .

[34]Here, we assume that the IHM gas follows the adiabatic cooling limit (equation 1), which is a lower limit to the IHM temperature. In reality, the IHM will be hotter than this lower limit due to, for example, X-ray pre-heating as suggested by 21-cm observations (HERA Collaboration 2023). Thus, M_{min} might be higher and the mass resolution requirement less stringent.
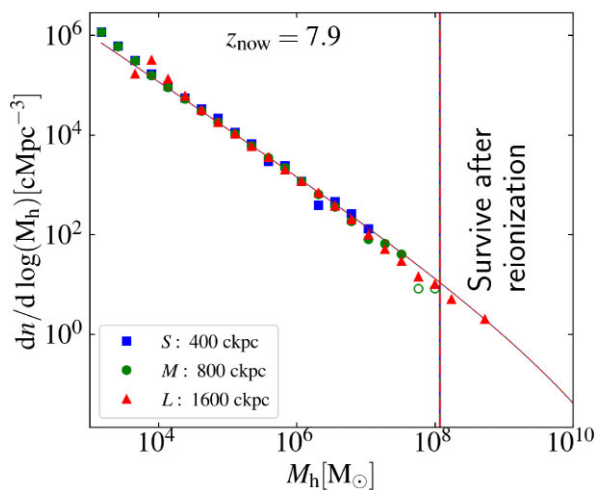
Figure D8. Impact of the extent of the simulation volume on the halo mass function at redshift 7.9. Different symbols correspond to simulations performed in volumes of linear extent ranging from 400 to 1600 ckpc, as per the legend. The empty symbols show bins with fewer than 5 haloes per $\log_{10}(M)$. The diagonal line is the fit to the mass function from Reed et al. (2007), the vertical line shows $M_{\rm crit}$, the halo mass above which gas can be retained after reionization (Okamoto et al. 2008), as discussed in Section 2.

Figure D9. Convergence of the clumping factor for different linear extents of the simulation volume. The mass resolution is $m_{\rm DM} = 960\,{\rm M_\odot}$, and we assumed $\Gamma_{-12} = 0.3$, and $z_i = 8$. The value of c_r at its peak only depends weakly on volume, but the asymptotic value of c_r increases from ~ 2 to ~ 3 when increasing the linear extent from 800 to 1600 pkpc. The figure also suggests that the asymptotic value of c_r is underestimated, even in the largest volume.

in simulations with $L_c = 800$ ckpc, (see Table 1) and therefore only begin to sample these more massive haloes.

Fig. D9 compares the evolution of c_r for these three simulations. The (first) value of $c_{r,\,\rm peak}$ is similar for all three runs (see also Park et al. 2016). This first maximum depends on mini-haloes with mass $\gtrsim 10^6\,{\rm M_\odot}$, which are well sampled even in simulation S. The second peak is higher when L_c is smaller. The reason is that the I-front that propagate from two opposing sides of the simulation cube overlap earlier for smaller values of L_c. At this earlier stage, c_r is still higher, as mini-haloes have had less time to photoevaporate. The late time clumping factor is 50 per cent higher in the simulation L compared to M, and a factor of two compared to S. This suggests that even our fiducial volume (M) does not contain enough (massive) collapsed structures after photoevaporation to compute c_r accurately.
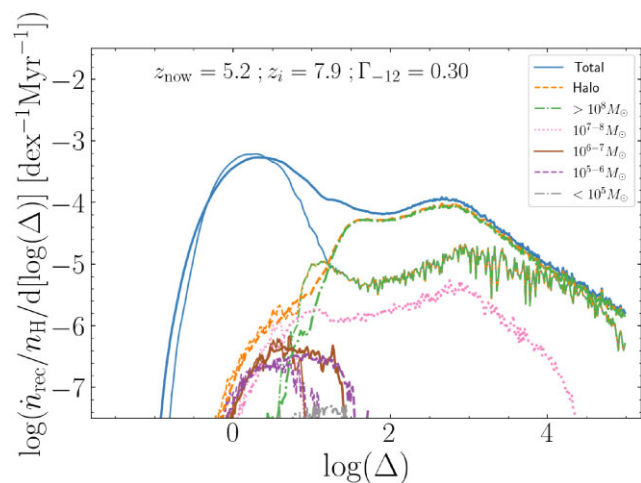
Figure D10. As Fig. D7, but for simulations with different linear extent, L_c: $L_c = 800$ ckpc (simulation S, thin lines) and $L_c = 1600$ ckpc (simulation L, thick lines). The simulation particle mass is $m_{\rm DM} = 800\,{\rm M_\odot}$ for both. Simulation L contains many more haloes with mass $10^8\,{\rm M_\odot}$ compared to simulation M. Gas in those haloes increases the recombination rate at $\Delta \sim 10^2$ significantly, as can be seen by comparing the thick and thin green lines (i.e. $> 10^8{\rm M_\odot}$ lines).

We examine the reason for the relatively poor convergence with L_c in more detail in Fig. D10. The ratio of more massive to lower mass haloes is larger in simulation L compared to M (Fig. D7). The gas in and surrounding these more massive haloes contributes significantly to the recombination rate and hence c_r in simulation L. This effect causes the dependence of c_r post-reionization on L_c.

After reionization, the minimum halo mass that can contribute significantly to c_r is close to the critical mass $M_{\rm char}$ from Okamoto et al. (2008, as discussed in Section 2.1, the minimum mass above which haloes retain 50 per cent or more of their cosmological baryon fraction). This mass is around $10^8\,{\rm M_\odot}$ at $z = 8$ and Fig. D8 shows that only simulation L samples a reasonable number of such haloes. This is not surprising: the parameters for our production runs were a trade-off between mass resolution and simulation volume for a given number of simulation particles and hence computation time. Our value of $c_r \lesssim 3$ post-reionization in simulation L agrees well with the value of $c_r \sim 3$ in the $L_c = 2\,h^{-1}$cMpc simulation of D'Aloisio et al. (2020), and the range of $c_r = 2.4$–2.9 found at $z = 6$ in the simulations with $L_c = 40\,h^{-1}$cMpc by McQuinn et al. (2011).

Our convergence requirement on L_c is more stringent than that of Emberson et al. (2013), who obtained differences of less than 5 per cent in c_r for simulations with $L_c = 1$ and 0.5 cMpc. We suggest that the difference stems from the fact that Emberson et al. (2013) did not account for photoevaporation and hence are unduly biased to low-mass mini-haloes, which dominate the recombination rate. Such low-mass haloes are already sampled reasonably well in simulations with smaller L_c.

It would be interesting to extend the types of simulations performed here to larger volumes and investigate the impact of even more massive haloes. Such simulations could then also be used to calculate the evolution of the attenuation length of ionizing photons. One aspect that such simulations should take into account is that these more massive haloes may host a galaxy, and the feedback from the galaxy's stars may affect the distribution of neutral gas inside and outside the halo.

APPENDIX E: I-FRONT TRAPPING IN A MINI-HALO

Here, we test the ability of our RT implementation to trap an I-front in a halo by comparing to analytical solutions. These are based on the model presented in Section 4.3, except that here we assume that an initially planar I-front over runs a halo, rather than that the halo is illuminated by ionizing radiation from all directions.

Consider therefore an initially planar I-front, propagating along the Z-axis from $Z > 0$ to $Z < 0$, and encountering a mini-halo located at the origin of the coordinate system ($Z = 0$). The mini-halo gas is modelled as a singular isothermal profile of equation (15). We assume that the gas density outside the halo's virial radius R_h is low enough such that the attenuation is negligible (but see Section 4.3). All of the gas is assumed to be static and has a uniform and constant temperature (hence, the recombination coefficient α_B is also uniform and constant).

There are two ways to calculate the equilibrium neutral hydrogen profile. First, we consider the ISL approximation under which gas downstream from the I-front is fully ionized and upstream is fully neutral. With this approximation, we can compute the total recombination rate, $\mathcal{R}$, along a line parallel to the Z-axis at impact parameter b. Equating $\mathcal{R}$ to the flux incoming flux yields the location $Z_{ISL}(b)$ of the inverse Strömgren layer, where gas transits from ionized to neutral. $Z_{ISL}(b)$ can be solved through the following equation,

$$
F = \alpha_B n_{H,h}^2 R_h^4 \int_{Z_{ISL}}^{Z_h} \frac{dZ'}{(b^2 + Z'^2)^2}
$$
$$
= \alpha_B n_{H,h}^2 \frac{R_h^4}{2b^3} \left(\arctan(z) + \frac{z}{1+z^2} \right) \Big|_{z=Z_{ISL}/b}^{z=Z_h/b}, \quad (E1)
$$

where $Z_h = (R_h^2 - b^2)^{1/2}$. The sign of Z_{ISL} can be positive or negative.

Ignoring the optical depth of the neutral gas downstream, we can find an approximate expression for the neutral fraction $x \equiv n_{HI}/n_H$ in photoionization equilibrium,

$$
\frac{x}{(1-x)^2} = \frac{\alpha_B n_H(Z, b)}{F_c}
$$
$$
F_c = \alpha_B n_{H,h}^2 \frac{R_h^4}{2b^3} \left(\arctan(z) + \frac{z}{1+z^2} \right) \Big|_{z=Z_{ISL}/b}^{z=Z/b}, \quad (E2)
$$

$$
x(b, Z) \approx \frac{n_{H,h}\alpha_B}{\sigma_{HI} F_c} \frac{R_h^2}{Z^2 + b^2}
$$
$$
= \frac{2b^3}{\sigma_{HI} n_{H,h} R_h^2} \frac{1}{Z^2 + b^2}
$$
$$
\times \left[\left(\arctan(z) + \frac{z}{1+z^2} \right) \Big|_{z=Z_{ISL}/b}^{z=Z/b} \right]^{-1}, \quad (E3)
$$

where x_h is the neutral fraction at R_h.

Second, we can drop the ISL approximation and calculate the neutral gas distribution considering the optical depth. Assuming photoionization equilibrium, we calculate the photon number density n_γ:

$$
\frac{\partial n_\gamma}{\partial t} = -\frac{\partial f_\gamma}{\partial Z} - n_{HI} c \sigma_{HI} n_\gamma = 0, \quad (E4)
$$

where f_γ is the photon flux which is approximately $f_\gamma = n_\gamma c$ if we ignore scattering. Then, we solve n_γ by integration

$$
n_\gamma(Z) = \frac{F}{c} \exp\left(-\int_Z^{Z_h} n_{HI}\sigma_{HI}dZ' \right). \quad (E5)
$$
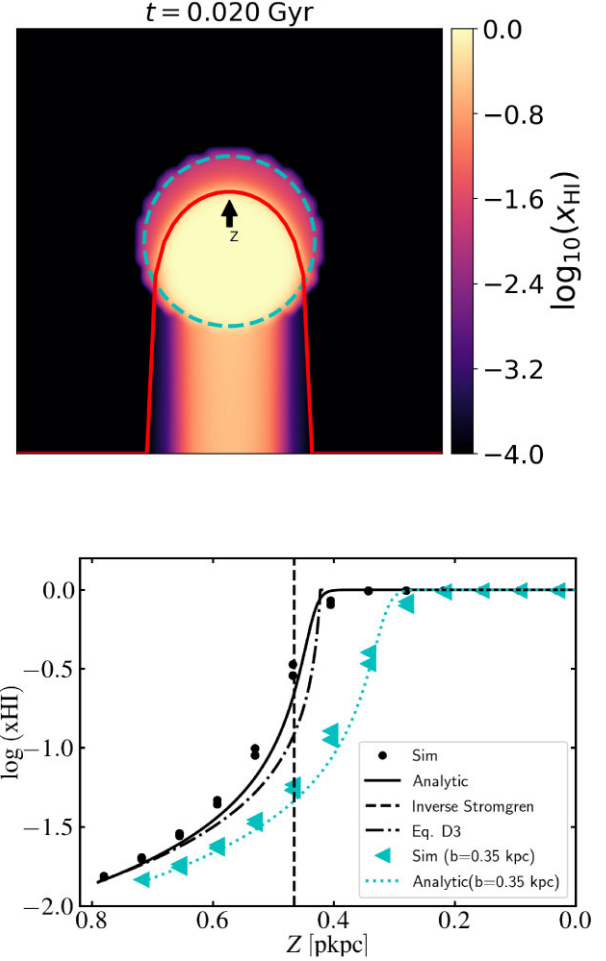
Figure E1. I-front trapping by a static gas cloud with a $1/R^2$ density distribution: the initially planar I-front moves vertically down. Upper panel: slice through the centre of the sphere, with colours indicating neutral fraction. The dashed circle indicates the initially neutral sphere. The solid line shows the approximate location of the ISL from equation (E1). The arrow indicates the origin and the positive Z-direction. Lower panel: neutral fraction x_{HI} as a function of Z, where the Z-axis runs vertically up from the centre of the sphere (as indicated in the upper panel). The circles and triangles are obtained from the simulation with impact parameters $b = 0$ and 0.35 pkpc, respectively. The solid and dotted lines are obtained by numerically integrating equation (E10) with impact parameters $b = 0$ and 0.35 pkpc, respectively. The vertical dashed line is the location of the ISL from equation (E1) for an impact parameters $b = 0$ pkpc. Finally, the dashed–dotted line represents the approximate neutral fraction (equation E3). The simulation follows the analytical result very closely. The text describes the simulation set-up in detail.

Substituting this relation into the equation expressing photoionization equilibrium:

$$
n_{HI} c \sigma_{HI} n_\gamma = n_e n_{HII} \alpha_B, \quad (E6)
$$

yields an equation for the neutral fraction, x,

$$
x c \sigma_{HI} \frac{F}{c} \exp(-\tau) = (1-x)^2 n_H \alpha_B, \quad (E7)
$$

where the optical depth is given by

$$
\tau = \int_Z^{Z_h} x n_H \sigma_{HI} dZ'. \quad (E8)
$$

We follow Altay & Theuns (2013) and take the logarithm on both side and differentiate with respect to Z,

$$\left(\frac{1}{x} + \frac{2}{1-x}\right)\frac{dx}{dZ} = -xn_H\sigma_{HI} + \frac{d\ln n_H}{dZ}. \tag{E9}$$

We then simplify and obtain the final differential equation

$$\frac{dx}{dZ} = -\frac{x(1-x)}{1+x}\left(xn_H\sigma_{HI} + \frac{2Z}{b^2+Z^2}\right), \tag{E10}$$

with boundary condition $x \to x_h$ when $Z \to Z_h$. We can integrate this equation numerically to find $x(Z,b)$. This more accurate expression is actually quite similar to the approximate, analytical solution of equation (E3) (see the lower panel of Fig. E1).

We now perform a simulation with the following numerical set-up. The computational volume has linear extent of $L_c = 6$ pkpc, and is filled with particles such that the mean density is $\langle n_H \rangle_{out} = 2 \times 10^{-4}$ cm^{-3}. The sphere is located at the centre of the simulation volume, has radius $R_h = 0.8$ pkpc and its density is normalized by $n_{H,h} = (200/3)\langle n_H \rangle_{out}$ so that its mean density is 200 times the surrounding density (and hence mimicking a cosmological halo). This density profile is realized with ≈ 2000 particles, this is equivalent to the resolution of a halo of mass 2.4×10^5 M$_\odot$ in our main production runs (Table 1). We neglect hydrodynamics and keep the temperature of the gas constant and uniform, using a recombination coefficient of $\alpha_B = 2.59 \times 10^{-13}$ cm^3 s^{-1} everywhere. We inject radiation from one side of the cubic simulation volume, with constant photon flux of $F = 1.5 \times 10^5$ cm^{-2}s^{-1}, and use $\sigma_{HI} = 8.13 \times 10^{-18}$ cm^2. Finally, we impose that the optically thin direction of the Eddington tensor is parallel to the Z-axis (Chan et al. 2021), which is perpendicular to the side through which we inject radiation), and use the RSL value of $\tilde{c} = 0.01c$.

The results of the simulation are compared to the analytical solution in Fig. E1, at 20 Myr after radiation was first injected. The upper panel is a slice through the centre showing the neutral fraction in the simulation, with the solid red line the approximate location of the ISL from equation (E1). The lower panel compares the simulation results (black circle symbols) to the more accurate expression found by integrating equation (E10) numerically (black solid line). The agreement between the simulation and the analytical solution is within a few percentages, demonstrating the accuracy of the numerical scheme. This close agreement also suggests that the simulation can accurately account for I-front trapping in mini-haloes with mass $M_h = 2.5 \times 10^5$ M$_\odot$ and higher.

## APPENDIX F: DETAILED RESPONSE TO THE PASSING OF IONIZATION FRONTS

Fig. F1 shows the response of the IHM to the passing of I-front for the simulation M512z8G03 quantitatively. The probability density distribution by volume, $\mathcal{P}_V$, is plotted at $z = 7.84$ (blue line) and $z = 7.58$ (orange line), as a function of[35] $\log \Delta$, $\log x_{HI}$, and $\log T$. Photoionization reduces $\mathcal{P}_V$ at intermediate densities, $\log \Delta \sim 1$–3, due to photoevaporation of the outskirts of mini-haloes.

To clarify better how regions of different densities react, we select particles in three ranges of overdensity $\Delta \equiv \rho/\langle\rho\rangle$ at $z = 7.84$, and track them to $z = 7.58$. We plot their PDF's as a function of Δ, x_{HI}, and T in Fig. F1.

The initially lowest density gas ($\Delta < 5$, brown dashed line) changes little in volume density due to reionization but becomes mostly highly ionized, $x_{HI} \leq 10^{-4}$, and is photoheated to a temperature, $T \sim 2.2 \times 10^4$ K. A small fraction of this gas is only partially ionized and partially heated ($T < 10^4$ K). The initially highest density gas ($\Delta > 200$, grey dotted–dashed line) also changes relatively little, staying mostly dense, neutral and cold, as it self-shields from the I-front. A small fraction by mass becomes ionized and heated, expanding to lower densities. The passage of the I-front impacts predominantly gas initially at intermediate densities ($5 < \Delta < 200$, purple dotted line): this gas expands significantly to lower densities as it is ionized and photoheated.

Some further features of Fig. F1 are worth noting. Although most of the gas is photoheated to $T \sim 2.2 \times 10^4$ K, a fraction is hotter, reaching $T \sim 10^5$ K. This corresponds to initially low-density gas ($\Delta < 5$) that is first photoheated by I-front and subsequently further adiabatically or shock-heated by the expansion of a nearby filament. This can be seen in Fig. 5, where the hot gas appears as red lines delineating filamentary structures. This comparison also shows the origin of the slightly cooler gas of $\log T[K] \sim 3.8$: this is initially intermediate density gas in filaments that cools adiabatically as the filaments expand. Finally, there is a 'knee' of gas at temperature $T \leq 10^3$ K below which gas has not been ionized and photoheated.

---

[35]Since the horizontal axis is $\log \Delta$ rather than Δ, the area under the curve is not proportional the fraction of volume at a given density. Rather, that would be $d\mathcal{P}/d\log\Delta \propto \Delta\, d\mathcal{P}/d\Delta$.
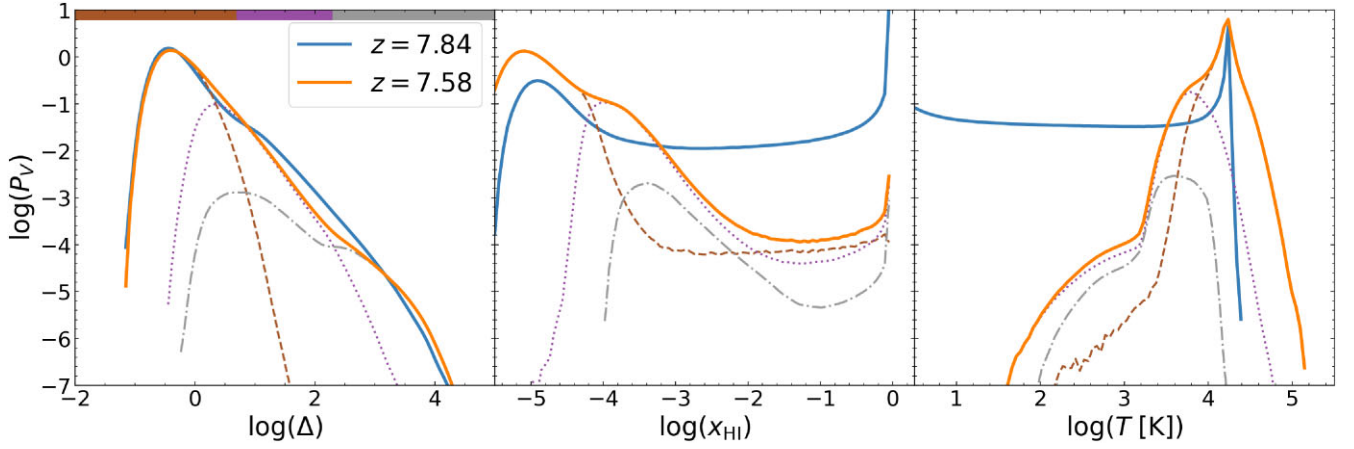
Figure F1. PDF by volume, $\mathcal{P}_V$, of the gas overdensity, $\Delta(= \rho/\langle\rho\rangle)$, neutral fraction, x_{HI}, and gas temperature, T (left to right), for two different redshifts as labelled, for M512z8G03 (the simulation shown in Fig. 5). We select gas at the higher redshift, $z = 7.84$, in three density ranges $\Delta < 5$, $5 < \Delta < 200$, and $\Delta > 200$, as illustrated by coloured top patches in the left panel, and trace it to redshift $z = 7.58$. The PDF by volume of this gas is plotted as dashed ($\Delta < 5$), dotted ($5 < \Delta < 200$), and dashed–dotted ($\Delta > 200$) lines in all panels.

This paper has been typeset from a TEX/LATEX file prepared by the author.